6-2019

Functionalization Of 2d-Zno for Selective Gas Sensing: First-Principles Analysis

Alaa F. M. Shaheen

Follow this and additional works at: https://scholarworks.uaeu.ac.ae/mechan_theses

Part of the Materials Science and Engineering Commons

Recommended Citation

United Arab Emirates University

College of Engineering

Department of Mechanical Engineering

FUNCTIONALIZATION OF 2D-ZnO FOR SELECTIVE GAS SENSING: FIRST-PRINCIPLES ANALYSIS

Alaa F. M. Shaheen

This thesis is submitted in partial fulfilment of the requirements for the degree of Master of Science in Materials Science and Engineering

Under the Supervision of Professor Nacir M. Tit

June 2019

Declaration of Original Work

I, Alaa F. M. Shaheen, the undersigned, a graduate student at the United Arab Emirates University (UAEU), and the author of this thesis entitled *"Functionalization of 2D-ZnO for Selective Gas sensing Applications: First-Principles Analysis"*, hereby, solemnly declare that this thesis is my own original research work that has been done and prepared by me under the supervision of Professor Nacir M. Tit, in the College of Science at UAEU. This work has not previously been presented or published or formed the basis for the award of any academic degree, diploma or a similar title at this or any other university. Any materials borrowed from other sources (whether published or unpublished) and relied upon or included in my thesis have been properly cited and acknowledged in accordance with appropriate academic conventions. I further declare that there is no potential conflict of interest with respect to the research, data collection, authorship, presentation and/or publication of this thesis.

Student's Signature: _____   Date: 25 / 8 / 2019

Approval of the Master Thesis

This Master Thesis is approved by the following Examining Committee Members:

1) Advisor (Committee Chair): Nacir M. Tit

   Title: Professor

   Department of Physics

   College of Science

   Signature _____   Date 27/6/2019

2) Member: Noureddine Amrane

   Title: Professor

   Department of Physics

   College of Science

   Signature _____   Date 27/6/2019

3) Member (External Examiner): Baker Mohammad

   Title: Associate Professor

   Department of Electrical and Computer Science

   Institution: Khalifa University of Science & Technology at Abu-Dhabi, UAE

   Signature _____   Date 27/6/2019

This Master Thesis is accepted by:

Dean of the College of Engineering: Professor Sabah Alkass

Signature _____ Date __18/8/2019__

Acting Dean of the College of Graduate Studies: Professor Ali Al-Marzouqi

Signature ___Ali Hassan___ Date ___26/8/2019___

Copy __3__ of __8__

Abstract

The scope of this MSc thesis is to theoretically search for suitable materials and relevant factors (e.g., dopants and catalysts) to induce gas sensing (GS) selectivity towards harmful gases such as H_2, H_2S and CO_2, under ambient conditions. We chose as material 2D-ZnO Honeycomb in the form of nanoribbon (ZnO-NR), which is very promising in the gas sensing applications. We employed a state-of-the-art computational method, based on a combination of the density-functional theory (DFT) and the Non-Equilibrium Green's Functions (NEGF) formalism, which both are incorporated in Atomistic Toolkit (ATK) package. This package is famous by its reliability in estimating the IV characteristics. The thesis consists of three phases: (1) Effect of dopants on gas sensing: Three organic-atoms (e.g., N, C, F) were initially attempted. But selectivity towards the detection of H_2 was achieved only in N-doped ZnO-NR. Special trend, discovered about the secrete of such selectivity, was the existence of negative differential resistance (NDR) in the IV characteristics of ZnO-NR:N. (2) Origins of NDR: the previous results led us to search for the origins of NDR in N-doped ZnO-NRs. We have investigated the effect of placing the doping atom N in three different positions across ZnO-NR, with respect to the edges (i.e.(i) at the O-rich edge, (ii) at the center, and (iii) at the Zn-rich edge.) Results show a clear trend that NDR shifts to higher energies than Fermi level, as well as both NDR and the Top-to-Valley-Current Ratio (TVCR)get reduced, when N-atom is moved from O-rich to Zn-rich edges. We concluded that the unpaired electron on N-atom, when it gets charged, causes the localization/curdling of wave-function at Fermi-level and consequently causes back-scattering and draw-back of current (so named NDR). (3) Effect of catalysts on gas sensing: Five transition-metal atoms (Pt, Pd, Au, Ag, and Fe) were used as ad-atom decorating ZnO-NR aiming to induce selectivity towards gases of interest (H_2, H_2S, and CO_2) in existence of other gases (e.g., O_2, N_2, and H_2O) at room temperature (RT). Results show that both Pt and Pd have poor selectivity at RT. Whereas, Fe is found to yield high selectivity toward detecting CO_2, while both Au and Ag have selectivity towards H_2S, at RT. All our findings are in excellent agreements with experimental data.

Keywords: Ab-initio calculations, Adsorbents on surfaces, Catalysis, Chemisorption, Gas sensing, Physisorption, Surface structure, Transition metal oxides, ZnO.

Title and Abstract (in Arabic)

العوامل المؤثرة في مادة أكسيد الزنك لزيادة تحسسها للغازات السامة: دراسة نظرية تحت درجة حرارية نظامية

الملخص

موضوع هذه الأطروحة هو دراسة نظرية للبحث عن المواد، مع تحديد العوامل المناسبة، لكشف واستشعار الغازات السامة مثل: الهيدروجين، ثاني هيدروجين الكبريت وثاني أكسيد الكربون تحت الظروف الجوية النظامية. لقد قمنا باختيار مادة أكسيد الزنك المصنعة على هيئة سبائك رقيقة نانوية لأنها معروفة أنها واعدة في صلاحية تطبيقاتها في مجال استشعار الغازات. من ناحية ثانية، قمنا باقتناء طريقة حسابية راقية تعتمد على شطرين: نظرية دالة الكثافة مع طريقة جرين لحساب الناقلية الكهربائية. كلتا الطريقتين مدموجتين في برنامج محاكاة واحد. يقسم العمل في هذه الأطروحة الى ثلاث مراحل: (1) دراسة تأثير الشوائب على كفاءة استشعار الغازات: قمنا بمحاولة دمج شوائب مثل ذرات النتروجين، الكربون والفسفور ورؤية تأثيراتها على الحصول على استشعار انتقائي للغازات. كانت النتيجة أنّ النتروجين هو الوحيد الذي يمتلك القدرة على احداث استشعار انتقائي لغاز الهيدروجين. اكتشفنا أنّ السر وراء ذلك هو حصول ناقلية تفاضلية سالبة لسبائك الزنك المنضبة بذرة النيتروجين، (2) دراسة أسباب حدوث الناقلية التفاضلية السالبة في سبائك أكسيد الزنك المنضبة بعنصر النتروجين: بات من المفروض أن نمر لدراسة أسباب حدوث الناقلية التفاضلية السالبة في سبائك الزنك المنضبة بالنتروجين. لقد وضحت الدراسة أنّ ذرة النتروجين تقل بالإلكترون واحد عن ذرة الأكسيجين. هذا النقص بالإلكترون واحد يحدث فراغا في رابطة كيميائية واحدة، والتي بدورها تحدث انحصارا كميا للشحنة من حول ذرة النيتروجين. خلال جريان التيار الكهربائي تشحن ذرة النيتروجين سلبا وذلك ينفر الالكترونات العابرة بل يجعل بعضها يعود من حيث أتى. تسبب هذه الظاهرة حدوث الناقلية التفاضلية السالبة، (3) دراسة تأثير المحفزات المعدنية على كفاءة استشعار الغازات: قمنا بتجربة خمس محفزات معدنية وهي: بلاتنيوم، بلاديوم، الحديد، الذهب الأصفر والذهب الأبيض. تم وضع ذرة المحفز على سطح سبيكة أكسيد الزنك ثم القيام بتجربتها في استشعار الغازات.

نستطيع تلخيص النتائج للمراحل الثلاث كالآتي: لقد دلت النتائج أنّ لوجود الناقلية التفاضلية السالبة في سبائك الزنك المنضبة بالنيتروجين أهمية بالغة في الحصول على كفاءة استشعارية عالية لغاز الهيدروجين. أما بالنسبة لتأثير المحفزات المعدنية، فلقد دلت النتائج أنّ كل

من البلاتنيوم والبلاديوم لا يمتلكان القدرة لإحداث استشعار انتقائي لأي غاز عند درجات حرارية نظامية. كما دلت النتائج أيضا أنّ محفز الحديد يحدث استشعارا انتقائيا لغاز ثاني أكسيد الكربون تحت درجات حرارية نظامية. في حين أنّ محفزي الذهب الأبيض والذهب الأصفر يحدثان استشعارات انتقائية لنفس الغاز وهو ثاني هدروجين الكبريت تحت درجات حرارية نظامية. تجدر الاشارة بأنّ جميع النتائج النظرية المحصلة في هذه الأطروحة في تطابق وتوافق مع جميع النتائج العملية التي نشرت والتي تم اجراءها في مختبرات عالمية.

مفاهيم البحث الرئيسية: الحسابات الأصلية، استشعار الغازات، الشوائب، ZnO.

Acknowledgements

I would like to express my gratitude and thanks to Allah, who gave me health and strength to finish this thesis. My great thanks and appreciation go to my supervisor Professor Nacir Tit whose interest about and introduction to Gas Sensing field got me started. I am especially grateful to my supervisor for his guidance, assistance and encouragement during the preparation of the thesis.

I would like to thank the chair and all members of the Department of graduate studies at the United Arab Emirates University for assisting me. My special thanks are extended to the United Arab Emirates University for allowing me to be enrolled in the Master program.

Special thanks go to my parents, brothers, and sisters who helped me along the way. I am sure they suspected it was endless.

Dedication

To my beloved parents and family

Table of Contents

List of Tables

List of Figures

List of Abbreviations

μ_L	Chemical Potential of Left electrode
μ_R	Chemical Potential of Right electrode
Å	Angstrom unit
a_B	Bohr radius
Ag	Silver
Ang(..)	Angle
ATK	Atomistix Tool Kit
Au	Gold
b(..)	Bond length
C	Carbon
CB	Conduction Band
CH_4	Methane Gas
CNT	Carbon Nanotubes
CO	Carbon Monoxide Gas
CO_2	Carbon Dioxide Gas
CPA	Coherent Potential Approximation
DDOS	Device Density of State
DFT	Density Functional Theory
DOS	Density of State
E_b	Bond dissociation Energy
E_{bind}	Binding Energy
E_F	Fermi-level Energy
Eg	Band Gap

Etot	Total Energy
eV	Electron Volt unit
F	Fluorine
Fe	Iron
G	Conductance
GaN	Gallium Nitride
G_g	Conductance in presence of gas
GGA	Generalized Gradient Approximation
G_o	Conductance in absence of gas
GS	Gas Sensing
H_2	Hydrogen Gas
H_2O	Water molecule
H_2S	Hydrogen Sulfide Gas
HOMO	Highest-occupied molecular orbital
HPC	High Performance Computers
IV	Current Voltage
K	Kelvin Degree
LCAO	Linear Combination of Atomic Orbitals
LDA	Local Density Approximation
LED	Light Emitting Diode
LRT	Linear Response Theory
LUMO	Lowest-unoccupied molecular orbital
L_y	Length in y-direction
L_z	Length in z-direction

MOFs	Metal-organic framework
MOSFET	Metal Oxide Semiconductor Field Effect Transistor
MWCNTs	Multi-wall carbon nanotubes
N	Nitrogen
N_2	Nitrogen Gas
NDR	Negative Differential Resistance
NEGF	Non-Equilibrium Green's Function
NO	Nitrogen Monoxide Gas
NO_2	Nitrogen Dioxide Gas
NP	Nanoparticle
NR	Nanoribbon
NT	Nanotube
O_2	Oxygen Gas
O_3	Ozone Gas
^oC	Celsius Degree
O_{Zn}	Zinc Anti-Site
PBE	Perdew Burke Emzerhof
Pd	Palladium
ppb	Part Per Billion
ppm	Part Per Million
Pt	Platinum
QCAS	Quantized Conductance Atomic Switch
R_g	Resistance in presence of gas
R_o	Resistance in absence of gas

RT	Room Temperature
S_{ave}	Average Sensitivity
SCell	Supercell
SIESTA	Spanish Initiative for Electronic Simulations with Thousands of Atoms
SMONs	Semiconducting Metal Oxide Nanostructures
SnO_2	Tin dioxide
T(E)	Transmission coefficient
TiO_2	Titanium Dioxide
TM	Transition Metals
TVCR	Top to Valley Current Ratios
UCF	Universal Conductance Fluctuations
VASP	Vienna Ab initio Simulation Package
V_b	Bias Voltage
VB	Valence Band
V_O	Oxygen Vacancy
V_{Zn}	Zinc Vacancy
w/	With
w/o	Without
ZnO	Zinc Oxide
ZnO-NR	Zinc Oxide Nanoribbon
ZnO-NR-N	Zinc oxide Nanoribbon doped with nitrogen
χ^C	Carbon Electronegativity
χ^H	Hydrogen Electronegativity
χ^N	Nitrogen Electronegativity

χ^{O} Oxygen Electronegativity

χ^{Pd} Palladium Electronegativity

χ^{Pt} Platinum Electronegativity

χ^{Zn} Zinc Electronegativity

Chapter 1: Introduction

1.1 Motivation for Gas Sensing

In recent times, air purification becomes of universal concern, especially after the escalation of the issue of global warming and spread of acid rains. Obviously, it is crucially important to live in an environment clean of toxic gases to avoid heath disasters. As a matter of fact, each toxic gas has limit above which it presents a health risk. The level of some gases is as low as one ppm (part per million) or even less. In addition to the fact that some gases are odorless and human nose fails to detect these gases. Indeed, it is very important to support or replace human nose when addressing toxic and deleterious gases detection, especially when dealing with the explosive ones such as hydrogen [1]. Recently, academic research and industry have paid more attention to gas sensing technology [2]. Considering a large number of gas detecting systems have lately been used in process control and laboratory analytics, it can be seen that it is essential to improve the levels of gas detection to influence high-performance gas sensors with high sensitivity, high selectivity, cheap price, low-power consumption, portable and rapid response [3]. Conventionally, the gas sensing mechanism is the occurrence of adsorption process between the surface of semiconducting metal oxides and gas species. Upon exposure to the target gas, chemisorption may happen to lead to charge transfer. This charge transfer will disturb the majority charge carries in the metal oxides and, consequently, changing the electrical conductance of the sensor. Generally, the resistance increases in the presence of oxidizing gases, such as such as nitrogen monoxide (NO), nitrogen dioxide (NO_2) and ozone (O_3) for n-type metal oxide semiconductor (like our case of ZnO); while the

resistance decreases in the case of reducing gases, like carbon monoxide (CO) and methane (CH_4) [4, 5]. On the other hand, the reverse is true for p-type surface.

1.2 Literature Review

From this perspective, extensive research has been active on both experimental and theoretical sides to search for materials with selectivity towards harmful gases at room temperature. Over time, metal oxides have been characterized by their high sensitivities, easy fabrication methods, low cost and high compatibility to be promising candidates for gas sensing applications [6-8]. As a result, metal oxides gas sensors reside to be predominant solid-state gas detecting devices. However, the morphology and structure of sensing material affect the performance of such sensors [9]. According to this, different type of metal oxides, such as ZnO, SnO_2, and TiO_2, have been developed and tested in the application of gas sensing and it was observed that morphology, surface state, and microstructure do play important roles in gas sensing performance [10]. Several investigations came out to a conclusion to agree that one-dimensional (1D) materials would consist strong candidates to take a leading edge among various nanostructures. This is due to their high surface-to-volume ration together with their reliable chemical and thermal stabilities [10, 11]. Limiting the sensing material, Zinc oxide (ZnO) has been rapidly chosen due to its low cost, high sensitivity, rapid response and fast recovery [12, 13]. In addition, ZnO has been one of the most examined sensitive materials for gas sensing [14].

Briefly, zinc oxide (ZnO) is an inorganic metal oxide compound. In nature, zinc oxide is found as a rare mineral called zincite. Therefore, most pure ZnO is produced synthetically and is found as a white powder. Zinc oxide is from group II-VI semiconductor compound, its ionicity resides at the borderline between covalent and

ionic semiconductor. ZnO has a hexagonal wurtzite crystal structure. ZnO is attracting notice in powder forms as well as thin films because of its enormous modern applications such as filler for rubber products, pigments in paint, electrophotography, and coating for papers, medicines, cosmetics, and sunscreens. Because of its hardness, it is used in the ceramic industry, while also it is considered to be cheap and nontoxic, zinc oxide has become commercially viable [15]. ZnO has shown high radiation hardness where it is useful in space applications. Moreover, ZnO has a variety of nanostructures and can be classified as follows: (i) one-dimensional group-(1D), (ii) two-dimensional group-(2D), and (iii) three-dimensional group-(3D). Under one dimensional structure, it can exist in many forms, for instance: nanorods, needles, helixes, springs and rings, ribbons, nanotubes, nano-belts, nano-wires, and combs. Also, zinc oxide can be structured in 2D including flower, dandelion, snowflakes, coniferous urchin-like, etc. [15, 16]. There are many ways to synthesis ZnO crystals. Namely, vapour deposition, precipitation in water solution, hydrothermal synthesis, the sol-gel process, and the mechano-chemical process can provide you with particles of different shape, size, and structure [17]. The properties of ZnO are highly dependent on its structure, morphology, aspect ratio, particle size and orientation [18-20]. ZnO crystalizes into three different 3D crystal structures, hexagonal wurtzite, cubic zinc blende, and rocksalt structure (see Figure 1.1) [21]. The most stable phase at ambient conditions among the three structures is the wurtzite phase. The Zinc-Blende structure can only be stabilized on a cubic structure while the rocksalt phase may be obtained at really high pressure. Moreover, the wurtzite structure consists of a hexagonal unit cell, where each anion, Oxygen, is surrounded by four cations, Zinc, at the corners of the tetrahedron.
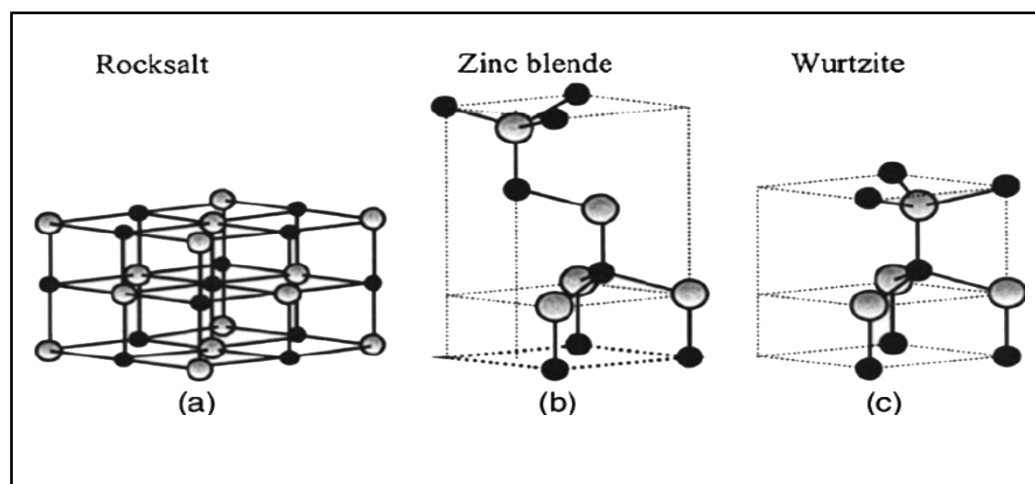
Figure 1.1 : ZnO 3D Nanostructures

Zinc oxide (ZnO) comprises unique physical and chemical properties to make it as a multifunctional material with high chemical stability, high electrochemical coupling, a broad range of radiation and high photo-stability (see Table 1) [15, 22]. Besides the breakthrough discovery of achieving p-doping [23], ZnO has proven itself successful in many applications. The most relevant applications comprise the following fields: (i) photonics: ZnO has a direct wide bandgap (3.37eV) and high exciton-binding energy (60 meV). Such a large bandgap is suitable for blue and ultraviolet optical devices and became rather a strong competitor to GaN. ZnO has been used in the fabrications of LED [24], (ii) electronics: dual-gate ZnO-nanorod-based MOSFET was fabricated [25], (iii) piezoelectrics: being a polar semiconducting material and having a wurtzite structure, ZnO can easily be functionalized for piezoelectric device applications [26], (iv) photo-catalysis: ZnO in nano-tube (NT) form is shown to have huge potential activity as a photo-catalyst to induce reactions of water splitting and hydrogen production [27], (v) biomedical: ZnO nano-particles (NPs) have been utilized in medical imaging and therapy. ZnO NPs have recently been favored in especially drug delivery to treat cancer-tumor cells because of their high-

luminescence efficiency and least toxicity properties [28], and (vi) gas sensing: there has been an evidence at all time that ZnO is a competitor to SnO_2 regarding the suitable material for sensing hazardous and toxic gases. Recently, nanostructured ZnO materials such as ZnO nanorods have been shown to reach very high selectivity toward sensing H_2S with an outstanding sensitivity at the scale of 1 ppb (part per billion) at room temperature [29, 30]. Such level of sensitivity is of great achievement as regard that this latter gas is so hazardous to an extent of the fact that the exposure to a dose of 10 ppm for 8 hours would endanger the human's life [31]; (vii) bio-sensing: such as detecting glucose [32].

Table 1: ZnO properties

Properties	Values
Crystal structure	Rock salt, Zinc-blende, Wurtzite
Energy Bandgap, eV	3.2, 3.3
Electron Mobility, cm^2Vs^{-1}	2.5-300 (Bulk ZnO), 1000 (Single nanowire)
Exciton Binding Energy, meV	60
Density, g/cm^3	5.606
Refractive Index	2.0041
Electron Effective Mass (m_e)	0.26
Relative Dielectric Constant	8.5
Melting point, ^oC	1975
Boiling point, ^oC	2360
Electron Diffusion Coefficient, cm^2s^{-1}	5.2 (Bulk ZnO), 1.7×10^{-7} (Particulate Film)

Regarding important gases to sense, the utilization of hydrogen as a renewable and clean energy source raised more attention since it provides a timely solution to the future supply in addition to other renewable energies [33, 34]. Therefore, it becomes an essential step for safety in industrial and household places to record hydrogen detection measurements. As a result, these measurements can help to raise alert for the formation of potentially explosive mixtures with air [35]. Higher sensitivity, higher

selectivity, and faster response time have been the main challenges in hydrogen sensor technology. However, some of the currently existing hydrogen sensors are not appropriate for fuel cells, household, biomedical and transportation applications because of their sizes, high-temperature operation, slow response, high cost, and energy input [36] but still, some are suitable for many industrial applications [37, 38]. Sensing material may fail to detect H_2 gas at RT, because they have high operating temperatures like >500 ^oC [39]. Accordingly, for H_2 sensor applications, the ZnO nanostructures should demonstrate improved performances, and ability to work at room temperature.

From gas sensing perspective, it is an ultimate priority to develop high-precision gas sensors with high sensitivity, fast response, good selectivity, low limit of detection, as well as real-time monitoring capabilities. To achieve this goal, many types of gas sensors have been dev{eloped, mostly including resistive [40], optical [41], ultrasonic and acoustic wave [42], thermoelectric [43] and electrochemical [44] ones. The most popular gas sensors type among all these types is the resistive gas sensor (also named "chemiresistive sensor") and is simple and easy to fabricate using cost effective processes. Resistive gas sensors mechanism is based on the change in resistance of a sensing layer upon adsorption and reaction with the target dopants, catalyst, and gas molecules. Sensitivity and selectivity are usually determined by the sensing layer. The sensing materials used in the resistive gas sensors are usually: (i) semiconducting metal oxide nanostructures (SMONs) [9, 40, 45], (ii) carbon materials such as graphene and CNT [46, 47], and (iii) organic semiconductors [48-52]. SMONs is more favorable when compared to carbon materials and organic semiconductors due to its higher sensitivity, faster response/recovery speed, better reversibility, simple fabrication processes and least cost.

In the computational side, Topsakal and coworkers used Vienna Ab-initio Simulation Package (VASP) and presented a detailed DFT study of the electronic structures and magnetic properties of ZnO versus its structural forms, ranging from 3D wurtzite, to 3D zinc-blende, to 3D hexagonal (graphite-like), to 2D periodic, and to 1D nano-ribbons (with both armchair and zigzag edges) [53]. After the hydrogen passivation of dangling bonds at the edges, armchair-edged ZnO-NR are shown to be semiconducting. Their bandgap energy increases with the reducing width of NR due to quantum-confinement effects. While zigzag-edged ZnO-NRs are shown to be metallic. Defects (e.g., oxygen vacancy "V_O", zinc vacancy "V_{Zn}", Zn-O divacancy, zinc anti-site O_{Zn}) on 2D honeycomb ZnO were further studied. The authors have shown that V_O creates a donor state while V_{Zn} create a magnetic moment [53].

1.3 Preliminary Plan

In the present thesis, we used the state-of-the-art Atomistic Toolkit (ATK) package, which is based on a combination of density-functional theory (DFT) and non-equilibrium Green's functions (NEGF) formalism, to study the adsorption and transport properties of ZnO nanoribbons. Within the scheme of ATK-package, the IV curves are calculated versus defect (like oxygen vacancy V_O) dopants and ad-atom decorations (like transition metals used as catalysts). This thesis is organized as follows: section 1.4 describes the computational model and method. Chapter 2 aims to relax dopants and defects (e.g., oxygen vacancy) in order to search for possible selectivity towards detection of H_2 gas. Therein, binding energy of various molecules can be estimated from total energy calculations. Moreover, sensitivity towards certain gas is estimated from the IV-curve by calculating the differential conductance/resistance. Chapter 3 explores the origins of negative differential

resistance for N-doped-ZnO-NR. Chapter 4 aims to search for suitable TM catalyst (among: Au, Ag, Pt, Pd, and Fe) used to functionalize ZnO-NR again in order to tune the selectivity toward a gas of interest for energy and environmental applications (such as H_2, H_2S and CO_2). Of course, to assess the selectivity, testing should include other gas molecules as well (list comprises: H_2, H_2S, H_2O, CO_2, O_2, N_2, etc..). The reasons behind any trend of selectivity are rigorously investigated. Chapter 5 summarizes the main findings.

1.4 Computational Model and Method

Four different supercells are used to simulate the zigzag-edged ZnO nanoribbons (ZnO-NR). In the first phase to study the effect of doping on ZnO-NR devices, two different supercells are designed. The first supercell is a sample to probe the band structures is composed of 3 rows of hexagons in width ($L_y = 11.80$ Å) and 8 layers (unit cells) along z-direction in length ($L_z = 27.17$ Å). This make the sample be composed of 64 atoms: 32 Zn + 32 O-atoms. The dangling bonds of the edge atoms of the nanoribbon are saturated with hydrogen atoms (i.e., 16 H-atoms are added to the total to become: 80 atoms). However, the supercell of central region, used in this study, has dimensions: A = 10 Å, B = 19.48 Å, and C = 27.17 Å, to ensure that the ZnO-NR is isolated from its mirror symmetries with respect to 2 directions (x, y directions) and continuous in z-direction. The second supercell is a device to probe the IV curves has the same previously described sample in its central zone and two electrodes on both sides of it, along z-direction. So, the supercell (two-probe system) is composed of left electrode (L), central scattering zone (C), and right electrode (R). Each electrode is described by a cell with three repeated ZnO unit cells along the transport z-direction (Each electrode consists of three layers of hexagons in length ≈ 10.19 Å). Electrodes

are modeled as an electron gas with a given chemical potential. The two-probe zigzag-edged ZnO-nanoribbon device models studied in phase 1 are shown in Figure 2.1 (in Chapter 2).

In the second phase, we study the effect of catalysts on the gas sensing performance of ZnO-NR devices, two different supercells are re-designed of bigger size than those used in studying the effect of doping because of the following reasons: (i) We had access to the newly-made available high-performance computers (HPC) which can run our ATK-package using 512 parallel processors; (ii) The inclusion of TM atoms is computationally demanding and this is no longer a problem using HPC; (iii) For a reliable calculation of IV curves the central region must be four times larger than the width of the electrode. The first supercell is a sample to probe the band structures is composed of 3 rows of hexagons in width (L_y = 11.80 Å) and 12 layers (unit cells) along z-direction in length (L_z = 40.75 Å). This make the sample be composed of 96 atoms: 48 Zn + 48 O-atoms. The dangling bonds of the edge atoms of the nanoribbon are saturated with hydrogen atoms (i.e., 24 H-atoms are added to make the total become: 120 atoms). Periodic boundary condition is applied only in z-direction. The dimensions of supercell are: A = 10 Å, B = 19.48 Å and C = 40.75 Å. These dimensions ensure the sample to be isolated in both x- and y-directions and be periodic in one direction (z-direction). The second supercell is a device to probe the IV curves has the same previously described sample in its central zone and two electrodes on both sides of it, along z-direction. We emphasize that it is recommended for the central zone to have a length of 4 times bigger than that of the electrode in order to have enough space to deposit the catalyst then the gas molecule at the center of the scattering zone in order to prevent the following artifacts: (i) prevent occurrence of folding of any ad-atom with its mirror in the regions of both electrodes; (ii) allow the

flow of higher current density to go through edges as it is well known that the hydrogen bonds to be weak and should populates the states at Fermi level and through the edges high current densities are expected; and (iii) changing the position of deposition of catalyst across the width of NR (especially as it is ultra-narrow) would affect the IV-curve, and this should be kept in the scope of a forth coming investigation. The two-probe ZnO-NR device models studied in phase 2 are shown in Figure 4.1 (in Chapter 4).

First-principle calculations are performed first to relax the structures toward minimum energy configurations, based on density-functional theory DFT within SIESTA algorithm [54]. The IV curves are evaluated using devices with inclusion of electrodes in which both DFT and non-equilibrium Green's function (NEGF) formalism are simultaneously applied.

About the details of the method, we emphasize that all the calculations are performed using the Atomistix Tool Kit (ATK) package [54-56]. The optimization of atomic structures is done using DFT within the generalized gradient approximation (GGA) of Perdew-Burke-Ernzerhof (PBE) for the exchange-correlation energy [57]. The Brillouin zone sampling was done using 1x1x100 Monkhorst-Pack technique [58]. The convergence criteria for total energy and Hellmann-Feynman forces were 0.001 eV and 0.01 eV/Å, respectively. The electrostatic potentials were determined on a real-space grid with a mesh cutoff energy of 2040 eV, and double-zeta-polarized basis set of local numerical orbitals were applied to all atoms. Dispersive interactions (i.e., van de Waals interactions) are accounted for by using Grimme's DFT-D2 empirical dispersion correction [59] to the PBE.

In the calculations of IV curves, the positive applied bias "V_b" would shift up the chemical potential of the left electrode with respect to the right electrode (i.e., $eV_b = \mu_L - \mu_R$). This fact produces conventional electric current from left to right electrode. The current can be calculated from two-terminal Landauer-Büttiker formula [60].

$$I(V_b) = \frac{2e}{h} \int_{-\infty}^{+\infty} T(E, V_b)[f_L(E - \mu_L) - f_R(E - \mu_R)] \qquad (1),$$

where e the charge of an electron; h is Planck's constant; T(E, V_b) is the bias-dependent transmission coefficient calculated from Green's functions; $f_{L/R}$ is the Fermi-Dirac distribution function of the left (L)/right (R) electrode; μ_L (=E_F - $eV_b/2$) and μ_R (=E_F + $eV_b/2$) are the electrochemical potentials of the left and right electrode, respectively. More details of the calculations can be found in references [54-56].

Furthermore, using ATK-package, one has an opportunity to probe electronic structures of the central (scattering) region after atomic relaxations, with exclusion of electrodes (e.g., doing the calculations of bands, density of states (DOS) and transmission coefficient). Whereas, in the calculations of IV curves the inclusion of electrodes is compulsory. From results of IV-curve, one can estimate the differential resistance:

$$R = \frac{dV}{dI} ; \qquad (2),$$

Using the finite-difference method, one would write:

$$R_n = \frac{V_{n+1} - V_{n-1}}{I_{n+1} - I_{n-1}} = \frac{2\Delta V}{I_{n+1} - I_{n-1}} ; \qquad (3),$$

where in our present case step $\Delta V = 0.1$ Volt and V_{max}= 1.0 Volt so n = 1, ...,9

Thereafter, the gas sensitivity "S" (or the sensor's response) is defined as [51, 61, 62]:

$$S = \frac{|G_g - G_o|}{G_o} = \frac{|R_g - R_o|}{R_g} \ ; \tag{4},$$

where G_g, G_o and R_g, R_0 are the conductance and resistance values in presence and absence of gas, respectively. The results of atomic relaxations, band structures, and adsorption and transport properties will be discussed in Chapter 2, Chapter 3 and Chapter 4. Discussion about the reliability and accuracy of calculating the IV curves will be elaborated in the Appendix A.

Chapter 2: Effect of Doping on Gas Sensing ZnO-NR- N

2.1 Introduction

The first attempt to induce gas sensing selectivity is to investigate the effects of intrinsic defects (such as oxygen vacancy "V_O") and the role of impurities or dopants on the performance of gas sensing. So, we have prepared a sample of zigzag-edged hydrogen-passivated ZnO-NR and calculated the IV curves of devices whose central zone is composed of one of the following cases: (i) pristine ZnO-NR; (ii) ZnO-NR with V_O; (iii) ZnO-NR doped with an organic element such as C, N and F. All these devices were used in testing their adsorption mainly to three gases (H_2, H_2S and CO_2). We were lucky to find N-doping would yield very high selectivity toward the detection of H_2 gas. The secret behind it, is that ZnO-NR:N possess a negative differential resistance (NDR) caused by the unpaired electron on N-atom. After chemisorption, each hydrogen atom plays a role of a donor giving charge to saturate the dangling bond of N-atom. Thus, the chemisorption of H_2 on ZnO-NR:N causes a rectification to the IV-curve as hydrogen plays a role of reducing gas. A second gas which causes another kind of modification to the IV characteristics is O_2. The chemisorption of O_2 on ZnO-NR:N causes an oxidation to the surface. Draining electrons by O_2 from the surface would cause more hampering to the electric current and further NDR. Yet, so as far as gas sensing is concerned, O_2 exist in 20% in the air, ZnO-NR:N should be considered as a good material candidate for high selectivity of H_2 gas. This chapter reports my work in this regard.

2.2 Atomic Relaxation

Without the inclusion of electrodes, a supercell can be defined for ZnO-NR, such as the zig-zag edge-terminated NR with periodic boundary condition in 1 direction (z-direction). One can use such a supercell to study adsorption; namely to carry on atomic relaxations of molecules on various sites of doped or undoped ZnO-NR then followed by calculating other physical quantities (e.g., density of states (DOS), energy bands and transmission coefficient). As far as the aim in the present investigation is the study of gas sensing properties, which are beyond the adsorption, the IV-curve calculation requires the inclusion of two electrodes through which a bias should be applied, and the electric current should be calculated. Figure 2.1 displays the atomically-relaxed structures of four samples with inclusion of two electrodes (to make devices), whose respective central regions are: (a) Pristine ZnO-NR; (b) N-doped ZnO nanoribbons (thereafter named ZnO-NR:N); (c) ZnO-NR:N after chemisorption of H_2 molecule; and (d) ZnO-NR:N after chemisorption of O_2 molecule. The used supercell (SCell) to describe the central zone (i.e., excluding electrodes) has dimensions: A = 10 Å, B = 19.48 Å, and C = 27.17 Å. In the case of pristine ZnO-NR, it contains 32 Zn-atoms + 32 O-atoms + 16 H-atoms = 80 atoms. The atomic relaxation process produces a structure with average bond lengths of about b(Zn-O) = 1.853-1.961 Å (corresponding to bonds being perpendicular and parallel to the z-axis, respectively), b(O-H) = 0.978 Å, and b(Zn-H) = 1.558 Å. The bond Zn-O length is consistent with the value d = 1.895 Å, reported by Topsakal and coworkers for ZnO honeycomb structure [53]. The studied ZnO-NR has asymmetric zig-zag edges (one edge is fully composed of O-atoms and the other edge is fully composed of Zn-atoms. They will be named O-rich edge and Zn-rich edge, respectively). The dangling bonds

are saturated with hydrogen atoms. The A-size and B-size of the SCell ensure the separation of the sheet from its mirror symmetries obtained by SCell's periodic-boundary conditions along x, y directions; while the C-size ensures the 1D-periodicity along z-axis (in case of exclusion of electrodes), and the matching to the electrodes (in case of devices). The combination of two similar electrodes is needed in IV-curve calculations, which are very essential in estimating the gas sensitivity in our current application. Each electrode is optimized to a size of 3 rows of atomic layers (See Figure 2.1(a)) and has a width of about 10.19 Å.

Figure 2.1(a) shows a relaxed structure of a device containing pristine ZnO-NR. Attempts of relaxing H_2 molecule on various sites such as: (i) Zn-site, (ii) O-site, (iii) Zn-O bridge-site, and (iv) hollow-site have all yielded physisorption with binding energies summarized in Table 2. So, one moved to test the effect of dopants like C, N, and F elements substituting an oxygen atom. Our tests included several gases such as H_2, O_2, N_2, H_2S, and H_2O. We discovered that N-doped ZnO-NR does have selectivity towards detecting H_2, and O_2, while all other gases exhibit physisorption. For this reason, we devote and focus our efforts on just one dopant which is nitrogen; also exploring other venues like defects such as oxygen vacancy, as it will be described below. The binding energies of various gas molecules on N-site in case of ZnO-NR:N are shown in Table 3.

Figure 2.1(b) shows the device containing one nitrogen (N) atom, in the middle of the central zone, substituting oxygen site. This device will be considered our main adsorbent bed of gases to be tested in our present investigation. Figure 2.1(c) shows the case of relaxing H_2 molecule on the N-site. This case yields a chemisorption associated with the dissociation of H_2 molecule, in which one H-atom binds to N-atom

and the other H-atom binds to a neighboring Zn-atom. Nevertheless, N-atom has limited coordination, so it breaks one bond with one Zn of the lattice and forms a kind of an extended defect. The formation energies are also summarized in Table 3. Figure 2.1(d) shows the case of relaxing O_2 molecule on the N-site. This case also yields chemisorption but without dissociation of the molecule. But, rather, the O_2 molecule breaks just one π-bond in order to pave the way for one of its two oxygen atoms to bind to N-atom and the second oxygen to bind to the Zn-atom near the dopant site. Furthermore, one recalls that the formation energy can be found in Table 3. The binding energy corresponding to the chemisorption process of H_2 molecule on the N-site does include the dissociation energy, which is about 4.52 eV/molecule [63]. So that the chemisorption of H_2 is more energetically costly than the cases of O_2 (i.e., the chemisorption of H_2 would have a relatively stronger effect than that of O_2 on the conductivity in the sample).
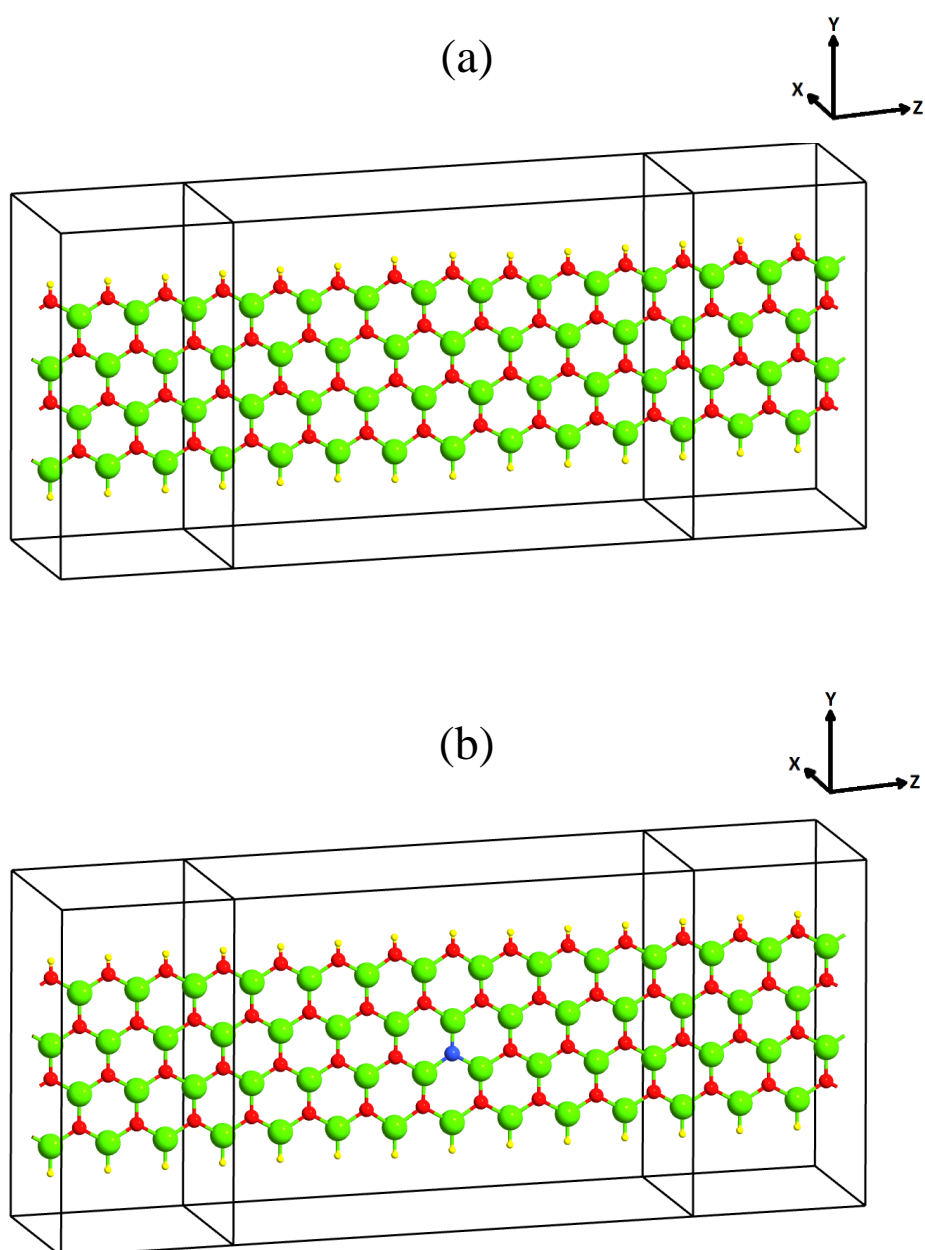
(a)

(b)

Figure 2.1 : Relaxed Structure of ZnO-NR devices
(a) Pristine ZnO-NR device (b) N-doped ZnO-NR device (c) H_2 on ZnO-NR device (d) O_2 on ZnO-NR device.

Note: Used colors are: O-atoms in red, Zn-atoms in green, H-atoms in yellow, N-atom in blue.

(c)

(d)
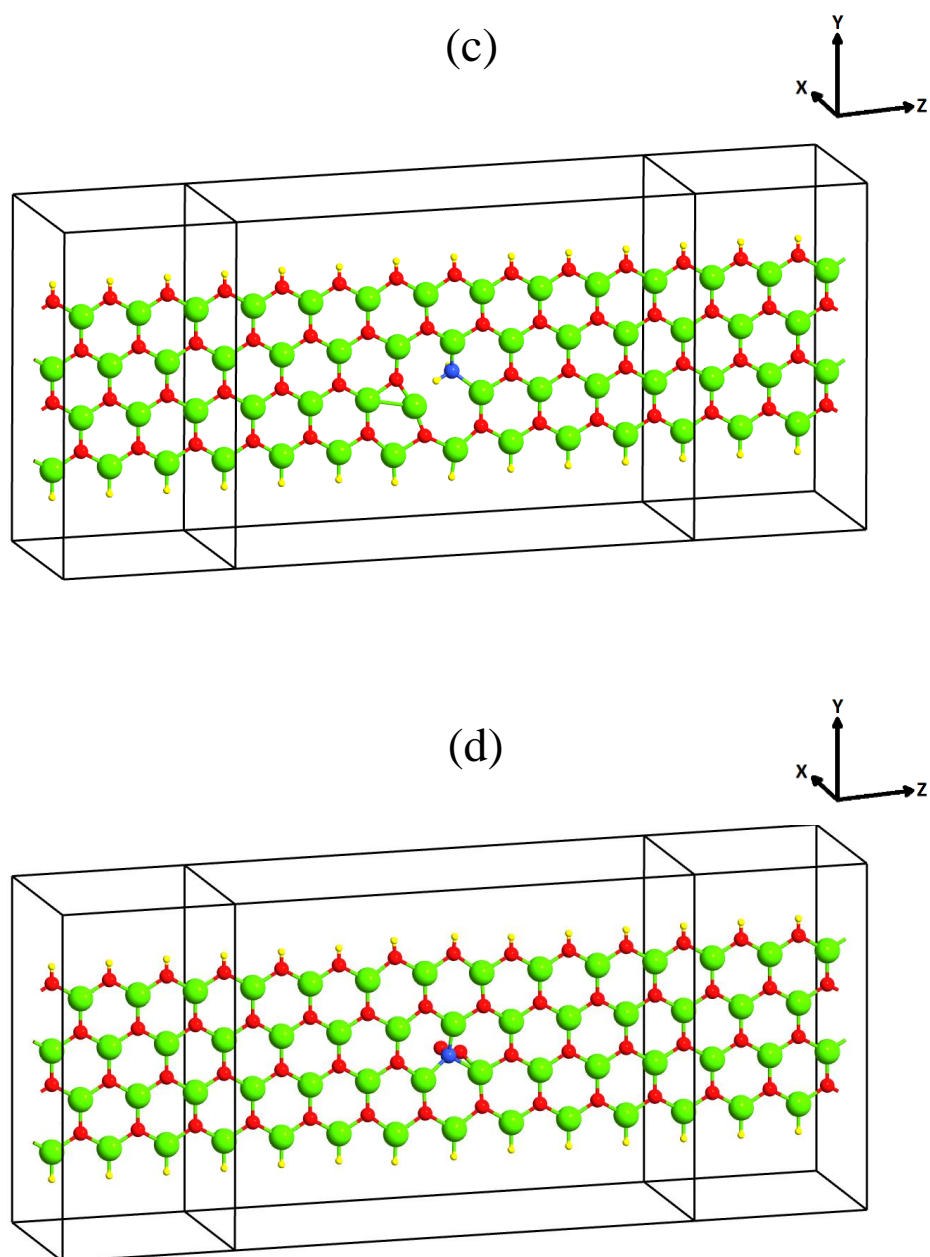
Figure 2.1: Relaxed Structure of ZnO-NR devices (continued)
(a) Pristine ZnO-NR device (b) N-doped ZnO-NR device (c) H_2 on ZnO-NR device (d) O_2 on ZnO-NR device.

Note: Used colors are: O-atoms in red, Zn-atoms in green, H-atoms in yellow, N-atom in blue.

Table 2 : Total and binding energies of H_2 molecule on various sites of pristine ZnO-NR.

System	E_{tot} (eV)	E_{bind} (eV)	Comments	
Molecule H_2	-30.798	---	---	
Pristine ZnO-NR	-64703.661	---	---	
H_2 on Zn-site	-64734.737	-0.278	Physisorption,	D = 2.03 Å
H_2 on O-site	-64734.696	-0.177	Physisorption,	D = 2.49 Å
H_2 on bridge-site	-64734.695	-0.236	Physisorption,	D = 2.07 Å
H_2 on hollow-site	-64734.874	-0.415	Physisorption,	D = 1.78 Å

Table 3 : Binding energies of several gas molecules on ZnO-NR:N.

System	E_{bind} (eV)	Comments
H_2 on N-site of ZnO-NR:N	-2.354	Chemisorption w/ dissociation
O_2 on N-site of ZnO-NR:N	-3.067	Chemisorption w/o dissociation
N_2 on N-site of ZnO-NR:N	-0.722	Physisorption
H_2O on N-site of ZnO-NR:N	-0.613	Physisorption
H_2S on N-site of ZnO-NR:N	-0.689	Physisorption
H_2 on V_O of ZnO-NR	-0.084	Physisorption
H_2 on N-site of ZnO-NR:N w/ V_O	-3.028	Chemisorption w/ dissociation

2.3 Transmission and Density of States

The two devices, hosting the chemisorption of H_2 and O_2 require further examination. In Figure 2.2, we present the calculations of transmission coefficient, $T(E)$, and device density of states (DDOS) for the two cases of chemisorption of H_2 and O_2, in red and green curves, respectively. It is important to see the existence of eigen-states versus energy by presenting DDOS before getting into the discussion of $T(E)$. Starting with DDOS results, it seems that the adsorption of H_2 has larger effect than the adsorption of O_2 on the sample (i.e., in terms of reconstructions of ZnO-NR:N) as can be shown from panels Figure 2.3(a) and Figure 2.3(b). In case of chemisorption of H_2 molecule, associated with its dissociation, the two H-atoms binds to N and Zn-atoms, separately, causing the following three effects: (1) The formation of N-H bond, which is covalent one with partial ionic character and in such situation charge transfer is expect to take place from H to N, as this latter has stronger electronegativity (Namely: $\chi^H = 2.20$ Pauling, $\chi^N = 3.07$ Pauling) [64]; (2) The formation of Zn-H bond, which is also covalent one with partial ionic character and charge transfer is expected to take place from Zn to H, as the former has weaker electronegativity than H-atom (i.e., $\chi^{Zn} = 1.66$ Pauling) [64]; (3) The breaking of one N-Zn bond with the neighboring zinc atoms around N-atom. So, the combination of all these three events would cause an accumulation of DDOS at an energy of about $E_F - 1.5$ eV. The eigen-functions of such eigen-energies ($E \approx E_F - 1.5$) are delocalized as they result in high transmission coefficient (see Figure 2.2(a)). Other valence-band states are a bit depleted and cause reduction in $T(E)$ (see Figure 2.2(a)).

Now, regarding the chemisorption of O_2, Figure 2.3(b) displays the results of DDOS. Actually, O_2 molecule does not exhibit any dissociation but rather just a breaking of π-bond to pave the way for one O-atom to bind to N-atom and the second O-atom to bind to Zn-atom. Besides, oxygen has a high electronegativity than both Zn-atom and N-atom (i.e., $\chi^O = 3.50$ Pauling) [64] so it is expected to drain charges from both Zn and N-atoms in establishing the 2 respective covalent bonds with partial ionic characters (i.e., O-N and O-Zn bonds). Yet, the structure of the adsorbent layer is not as much disturbed as in the case of H_2 chemisorption. That's why T(E) changes after the landing of O_2 on the surface but with less deviation as compared to the case of the landing of H_2 (i.e., compare Figure 2.2(a) and Figure 2.2(b), respectively). So, process of desorption should be easier to take place in case of oxygen gas; whereas sensitivity of sample toward H_2 should be larger, and the calculations of IV-curve would indicate that (see below).

(a)

(b)
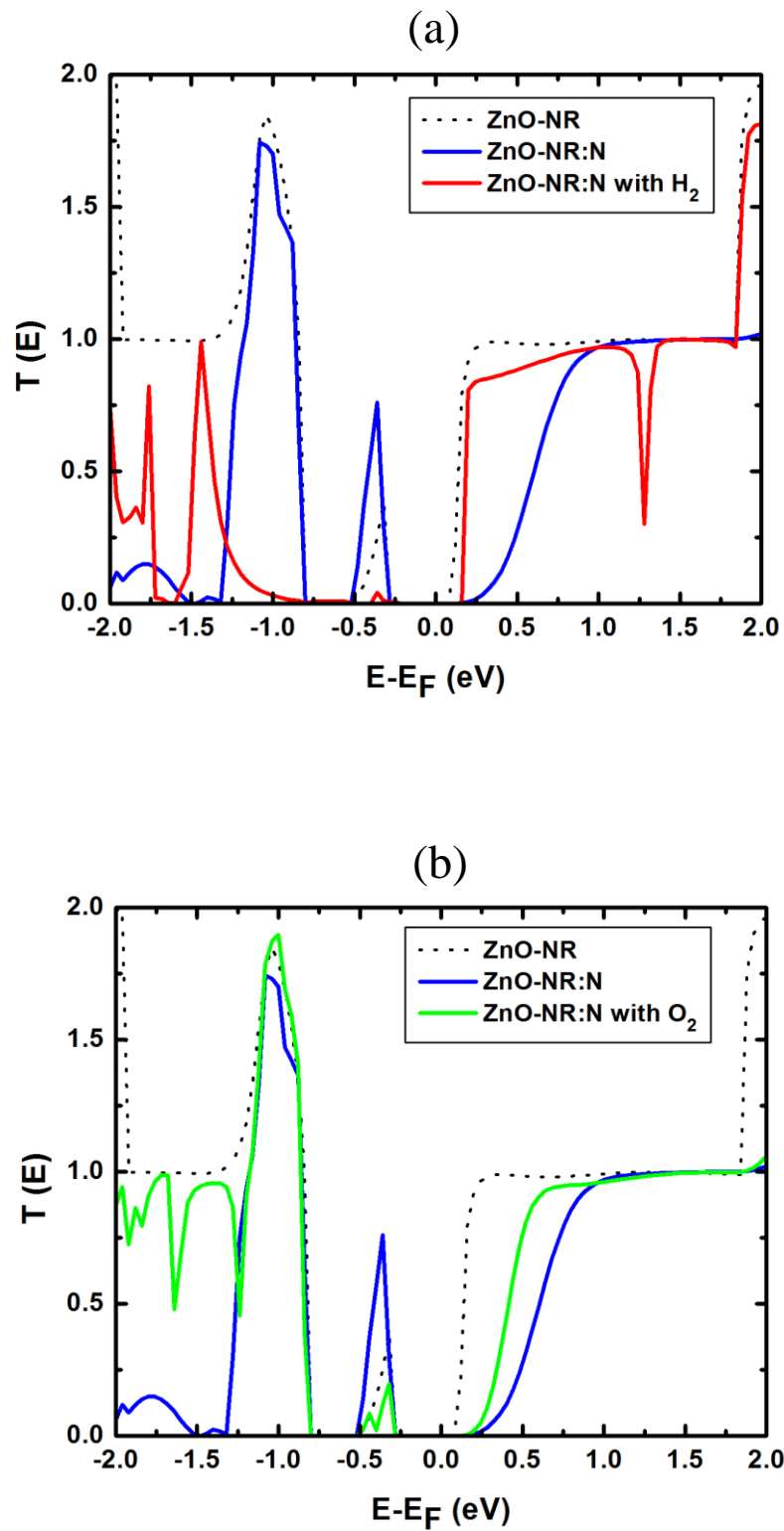
Figure 2.2 : Device Transmission Coefficient T(E) of ZnO-NR devices
(a) H_2 gas molecule (b) O_2 gas molecule on ZnO-NR:N device

(a)

(b)
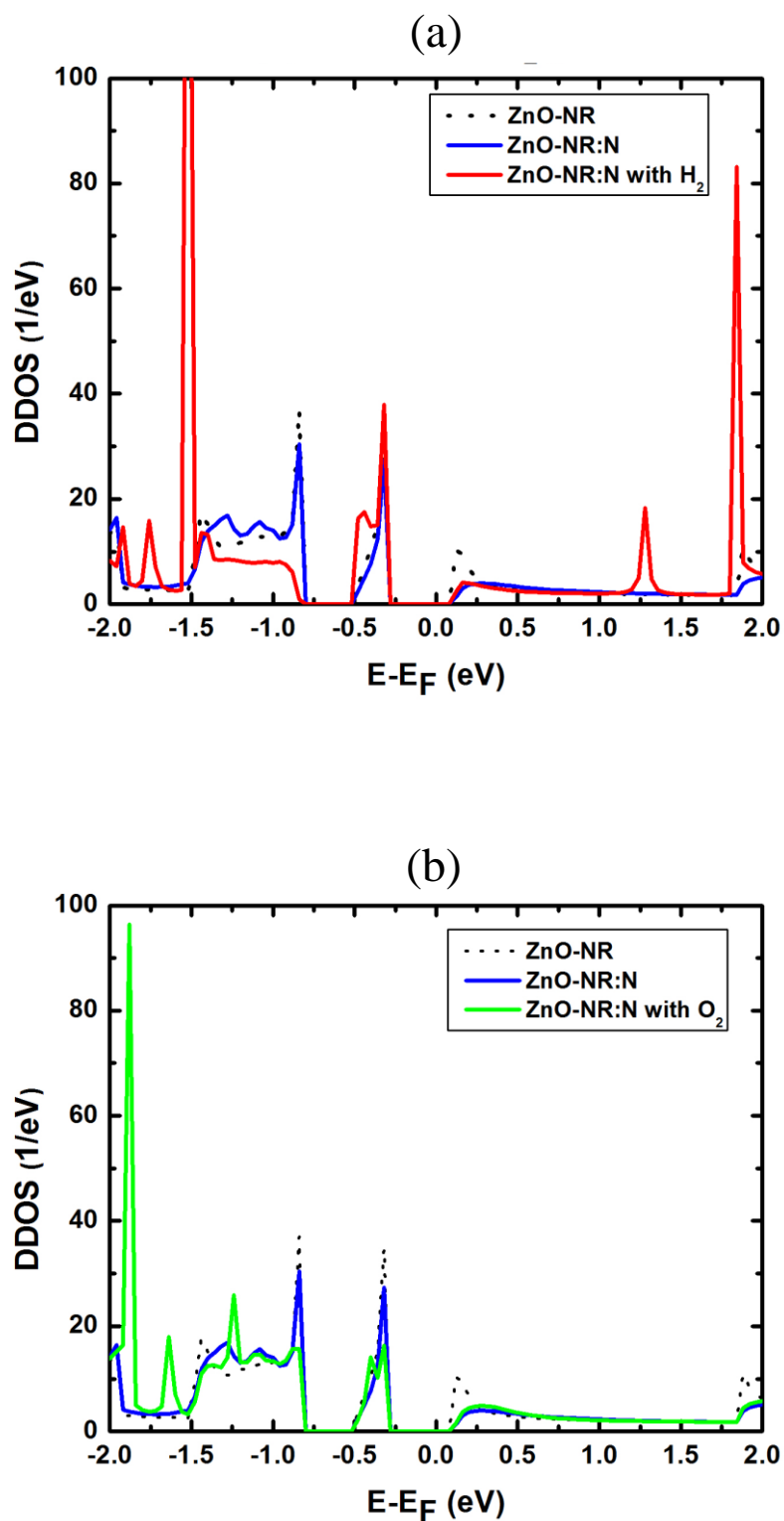
Figure 2.3 : Device Density of States (DDOS) of ZnO-NR devices
(a) H_2 gas molecule (b) O_2 gas molecule on ZnO-NR:N device

2.4 HOMO and LUMO States

Understanding charge transfer is an important component in analyzing the adsorption properties and their effects on gas sensing. Figure 2.4 displays the highest-occupied molecular orbital (HOMO) and the lowest-unoccupied molecular orbital (LUMO) eigen-functions' moduli for three devices: (a) ZnO-NR:N; (b) ZnO-NR:N after chemisorption of H_2 molecule; and (c) ZnO-NR:N after chemisorption of O_2 molecule. In Figure 2.4(a) (system ZnO-NR:N), HOMO state is localized on the dopant N-site, likely, due to the valency of N being less by 1 electron than the valency of O-atom. This would form a hole state, which may trap the electrons at HOMO level; whereas, the LUMO eigen-state is extended over the oxygen sites (see Figure 2.4(b)). LUMO state is revealing the asymmetry existing in the structure of the nanoribbon as the upper edge fully composed of oxygen atoms (i.e., O-rich edge) and lower edge fully consisted of Zn-atoms (i.e., Zn-rich edge). In Figure 2.4(c) (system ZnO-NR:N with H_2 molecule), HOMO state is repelled from N-site as the H-atoms binds to N and Zn, and dangling bonds are passivated; whereas LUMO remains to behave as extended state on O-atoms (see Figure 2.4(d)). In Figure 2.4(e) (system ZnO-NR:N with O_2 molecule), O_2 gets chemisorbed without dissociation and where 2 O-atoms making bonds with N and Zn would let charges be drained by the O-atoms of the molecule as they have larger electronegativity for HOMO state; whereas, the LUMO state persists to be delocalized on O-sites (see Figure 2.4(f)).
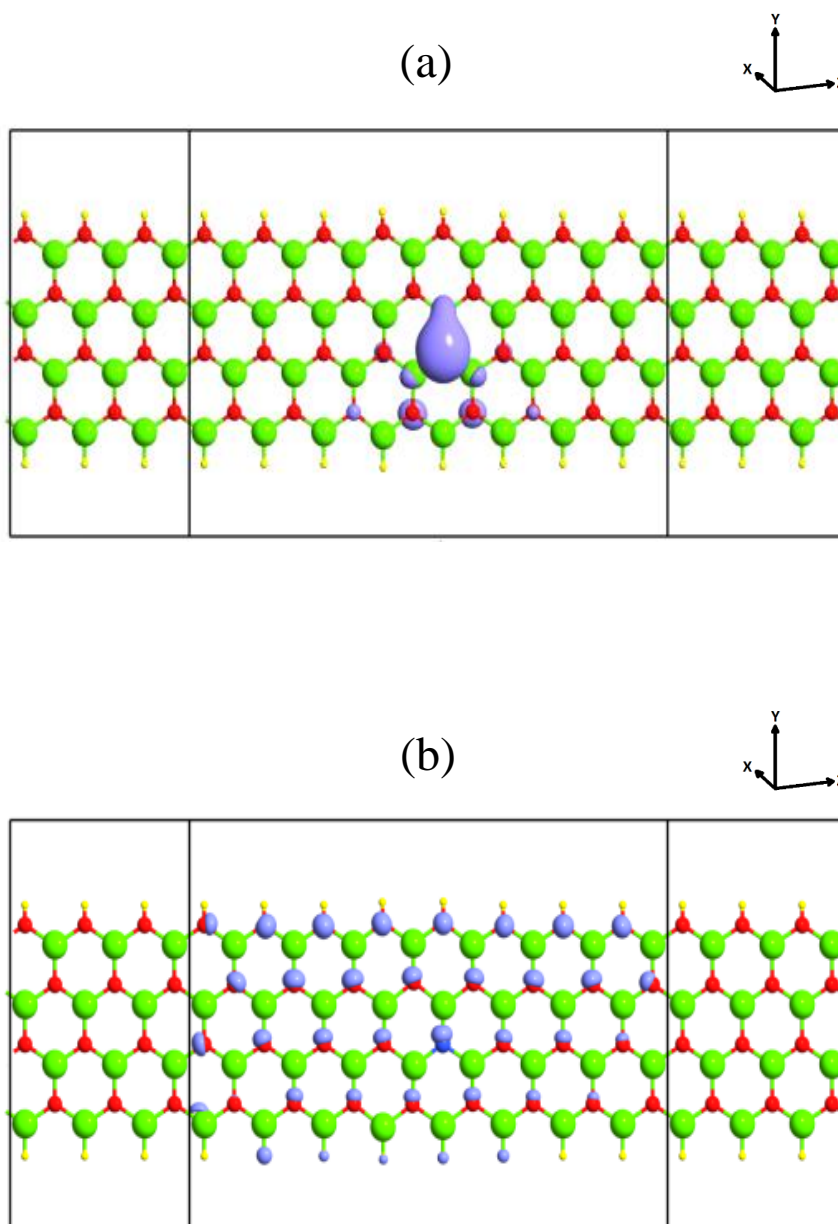
Figure 2.4 : HOMO and LUMO eigen-states of ZnO-NR devices
(a) ZnO-NR: N device HOMO eigen-states (b) ZnO-NR: N device LUMO eigen-states (c) H_2 molecule on ZnO-NR: N device HOMO eigen-states (d) H_2 molecule on ZnO-NR: N device LUMO eigen-states (e) O_2 molecule on ZnO-NR: N device HOMO eigen-states (f) O_2 molecule on ZnO-NR: N device LUMO eigen-states.
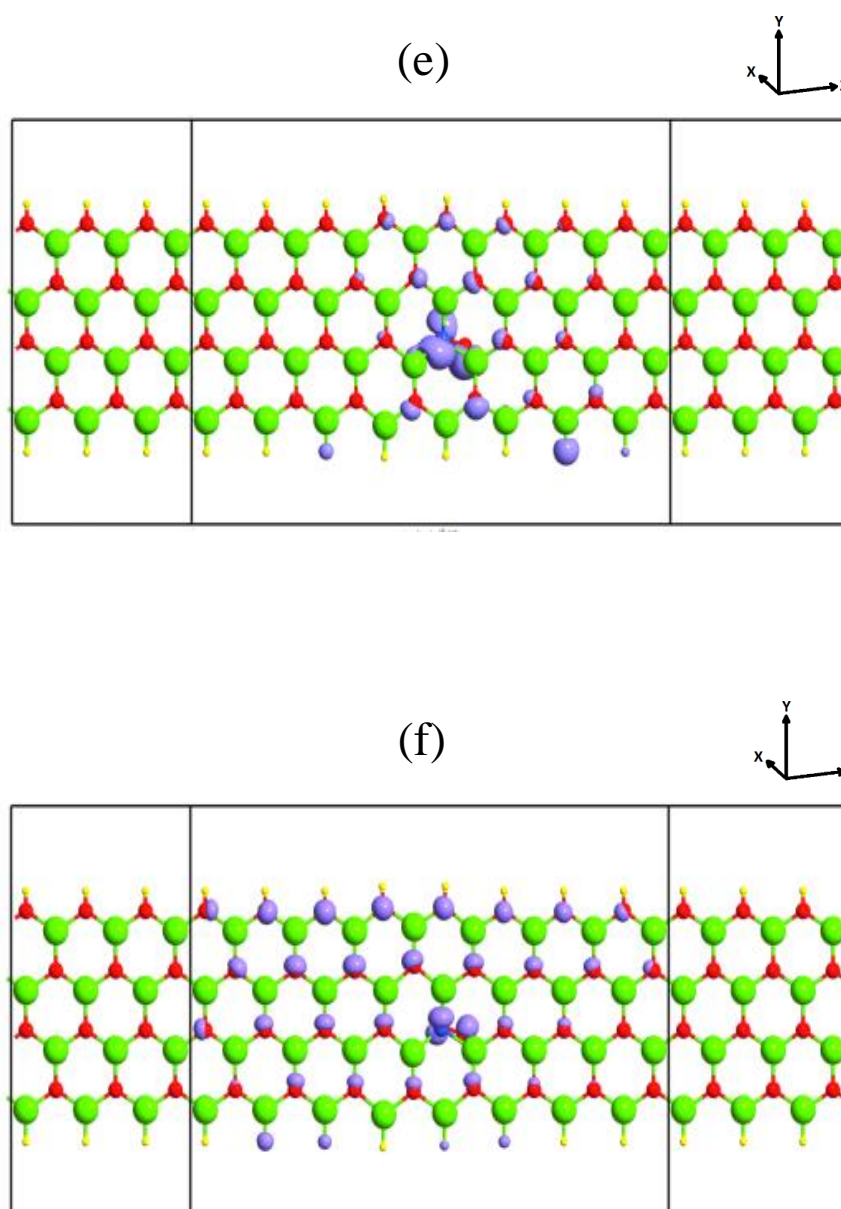
(c)

(d)

Figure 2.4 : HOMO and LUMO eigen-states of ZnO-NR devices (continued)
(a) ZnO-NR: N device HOMO eigen-states (b) ZnO-NR: N device LUMO eigen-states (c) H_2 molecule on ZnO-NR: N device HOMO eigen-states (d) H_2 molecule on ZnO-NR: N device LUMO eigen-states (e) O_2 molecule on ZnO-NR: N device HOMO eigen-states (f) O_2 molecule on ZnO-NR: N device LUMO eigen-states.

(e)

(f)

Figure 2.4 : HOMO and LUMO eigen-states of ZnO-NR devices (continued) (a) ZnO-NR: N device HOMO eigen-states (b) ZnO-NR: N device LUMO eigen-states (c) H_2 molecule on ZnO-NR: N device HOMO eigen-states (d) H_2 molecule on ZnO-NR: N device LUMO eigen-states (e) O_2 molecule on ZnO-NR: N device HOMO eigen-states (f) O_2 molecule on ZnO-NR: N device LUMO eigen-states.

2.5 Band Structures

Figure 2.5 displays the band structures of 1D-periodic samples corresponding to a central zone of the following samples: (a) ZnO-NR; (b) N-doped ZnO-NR; (c) ZnO-NR:N after chemisorption of H_2 molecule; and (d) ZnO-NR:N after chemisorption of O_2 molecule. The bandgap energies of these structures are summarized in Table 4. The common platform sample used for detection of both H_2 and O_2 is ZnO-NR:N, whose band structure is in Figure 2.5(b), in which Eg = 0.533 eV and Fermi level lies in the gap close to the valence-band edge, as N-atom seems to act as an acceptor. Then the chemisorption of H_2 molecule on ZnO-NR:N seems to make the gap a bit larger (Eg = 0.677 eV), shown in Figure 2.5(c), by passivating the dangling bonds of N-atom. But Fermi level being located near the edge of the conduction band would reveal the fact that hydrogen atoms result in n-type doping, where H-atoms behave like donors. The coupling of O_2 molecule to the ZnO-NR:N surface clearly shown in Figure 2.5(d) to produce deep trap states in the gap. The bandgap energy is reduced to Eg = 0.353 eV but the band at Fermi level looks flat (localized on defect) and likely will not consist a conducting channel for the electric current and results in higher impedance.

Table 4 : Bandgap energies and position of Fermi level, in cases of chemisorption of H_2 and O_2 molecules.

System	Eg (eV)	Fermi Level
Pristine ZnO-NR	0.533	@ mid-gap
N-doped ZnO-NR	0.533	Close to VB
ZnO-NR:N after H_2 chemisorption	0.677	@ CB edge
ZnO-NR:N after O_2 chemisorption	0.357	@ mid-gap
Pristine ZnO-NR with V_O	0.683	@ mid-gap
N-doped ZnO-NR with V_O	0.806	Close to VB edge
N-doped ZnO-NR with V_O after H_2 chemisorption	1.0256	Close to CB edge
ZnO-NR with V_O after H_2 chemisorption	0.639	@ mid-gap
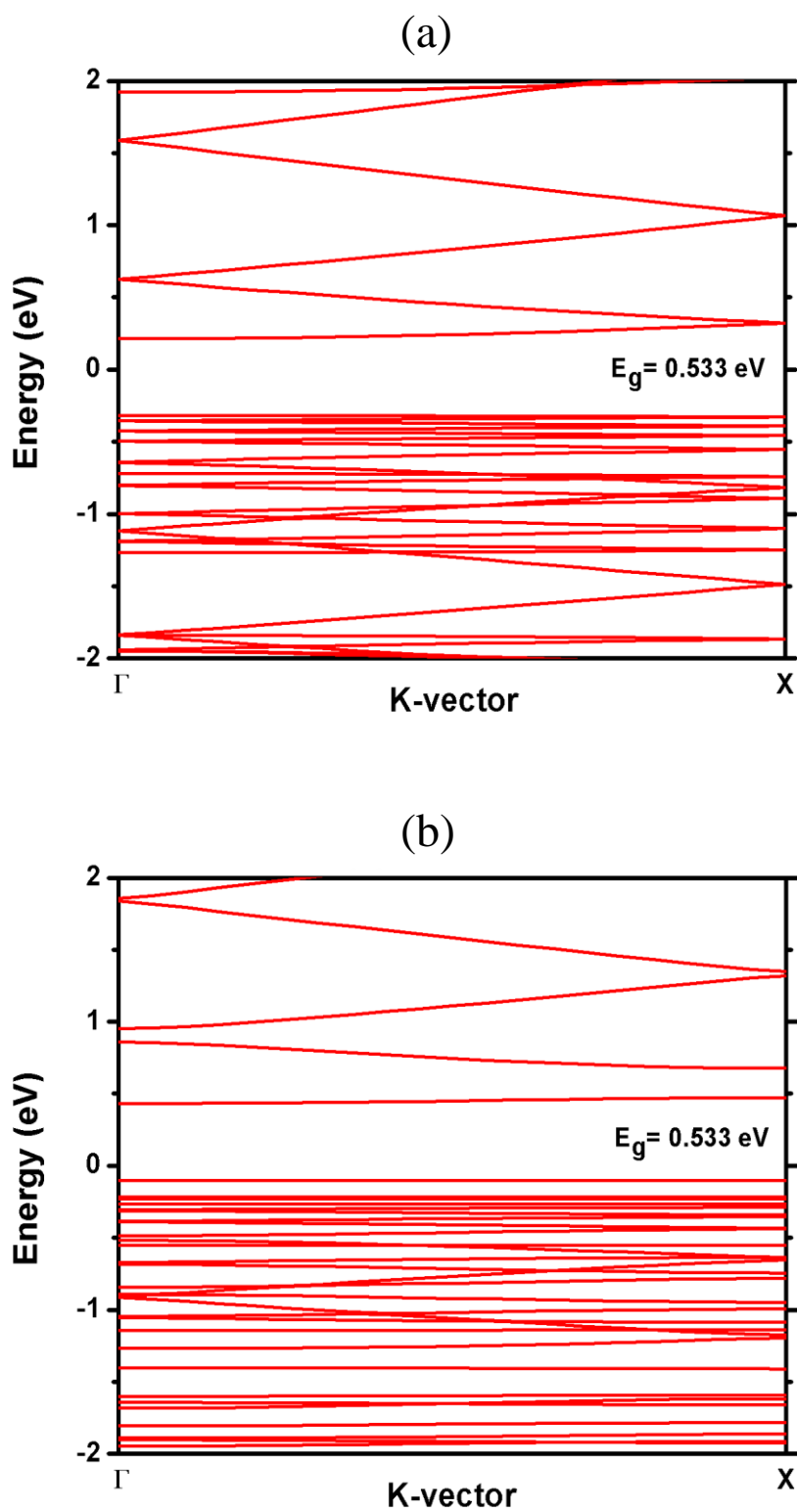
Figure 2.5 : Band Structure of ZnO-NR devices
(a) Pristine ZnO-NR device (b) N-doped ZnO-NR device (c) H_2 on ZnO-NR:
N device (d) O_2 on ZnO-NR: N device.

(c)

$E_g= 0.677$ eV

(d)

$E_g= 0.357$ eV
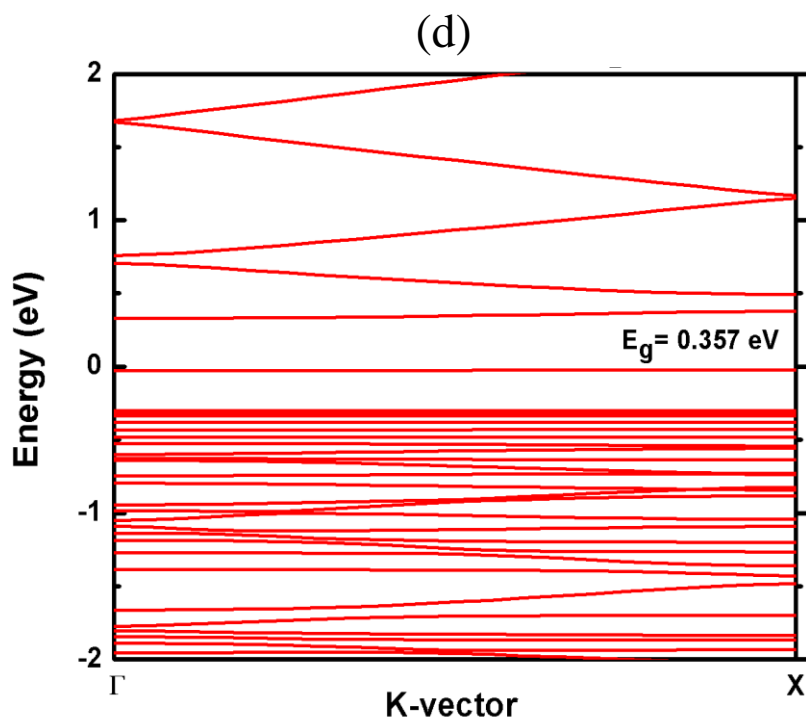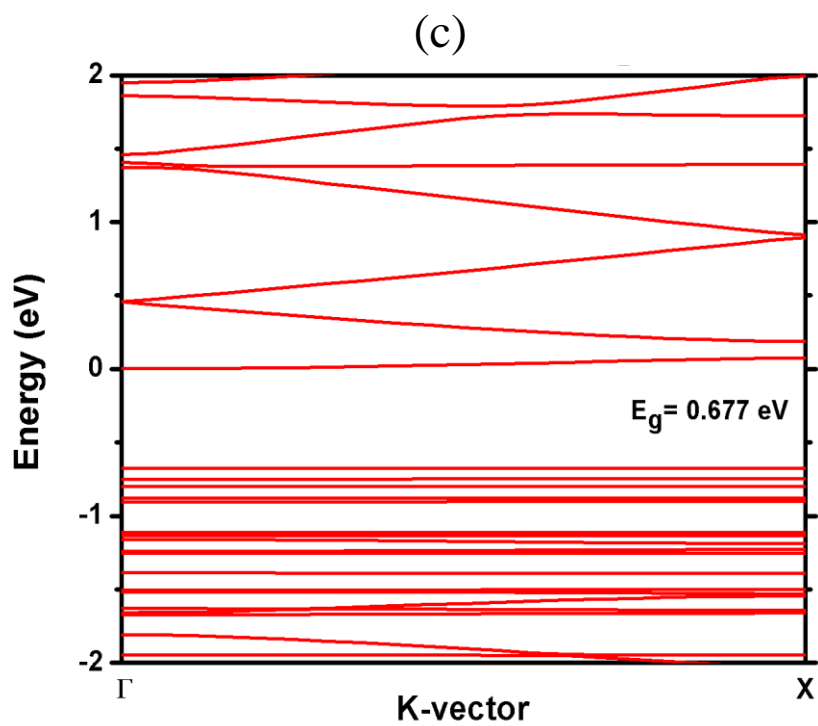
Figure 2.5 : Band Structure of ZnO-NR devices (continued)
(a) Pristine ZnO-NR device (b) N-doped ZnO-NR device (c) H_2 on ZnO-NR:
N device (d) O_2 on ZnO-NR: N device.

2.6 IV curves and Negative-differential Resistance

We have evaluated IV curves for 4 devices, whose central zones are: (i) pristine ZnO-NR; (ii) N-doped ZnO-NR; (iii) ZnO-NR:N after the chemisorption of H_2 molecule; (iv) ZnO-NR:N after the chemisorption of O_2 molecule. Results are shown in Figure 2.6 in two separate panels for clarity. Panel 2.6(a) includes systems (i), (ii) and (iii) corresponding to H_2 adsorption; Panel 2.6(b) comprises systems (i), (ii) and (iv) to correspond to O_2 adsorption. The applied bias is ranging from 0 to 1 Volt with a bias-spacing of $\Delta V = 0.1$ Volt. We note the following trends: (1) Figure 2.6(a) shows a great enhancement in conductance after the landing of H_2 on ZnO-NR:N surface with great contrast to the cases of O_2 chemisorption, shown in Figures 2.6(b); (2) One common trend, very noticeable between panels of Figure 2.6(a) and 2.6(b), is that the current is vanishingly small when $V \leq 0.4$ Volt. This is attributed to the bandgap of relaxed samples (i.e., ZnO-NR:N with molecule after occurrence of chemisorption), including the existence of localized states (defect states), yet, not allowing the peculation of electric current with energies $E \leq E_F + 0.4$ eV (see band structures shown in the previous sub-section); (3) The existence of a negative differential resistance (NDR) in IV characteristics corresponding to ZnO-NR:N and ZnO-NR:N after chemisorption of O_2. Similar behaviors of NDR have been reported in devices, for instance, containing asymmetrically gated graphene nanoribbons (GNR) by Al-Dirini and coworkers [65], as well as devices containing step-like GNR by An and coworkers [66]. In our present case of devices containing ZnO-NR:N, the origins of NDR by itself deserve a full study that we plan in a forth coming investigation.
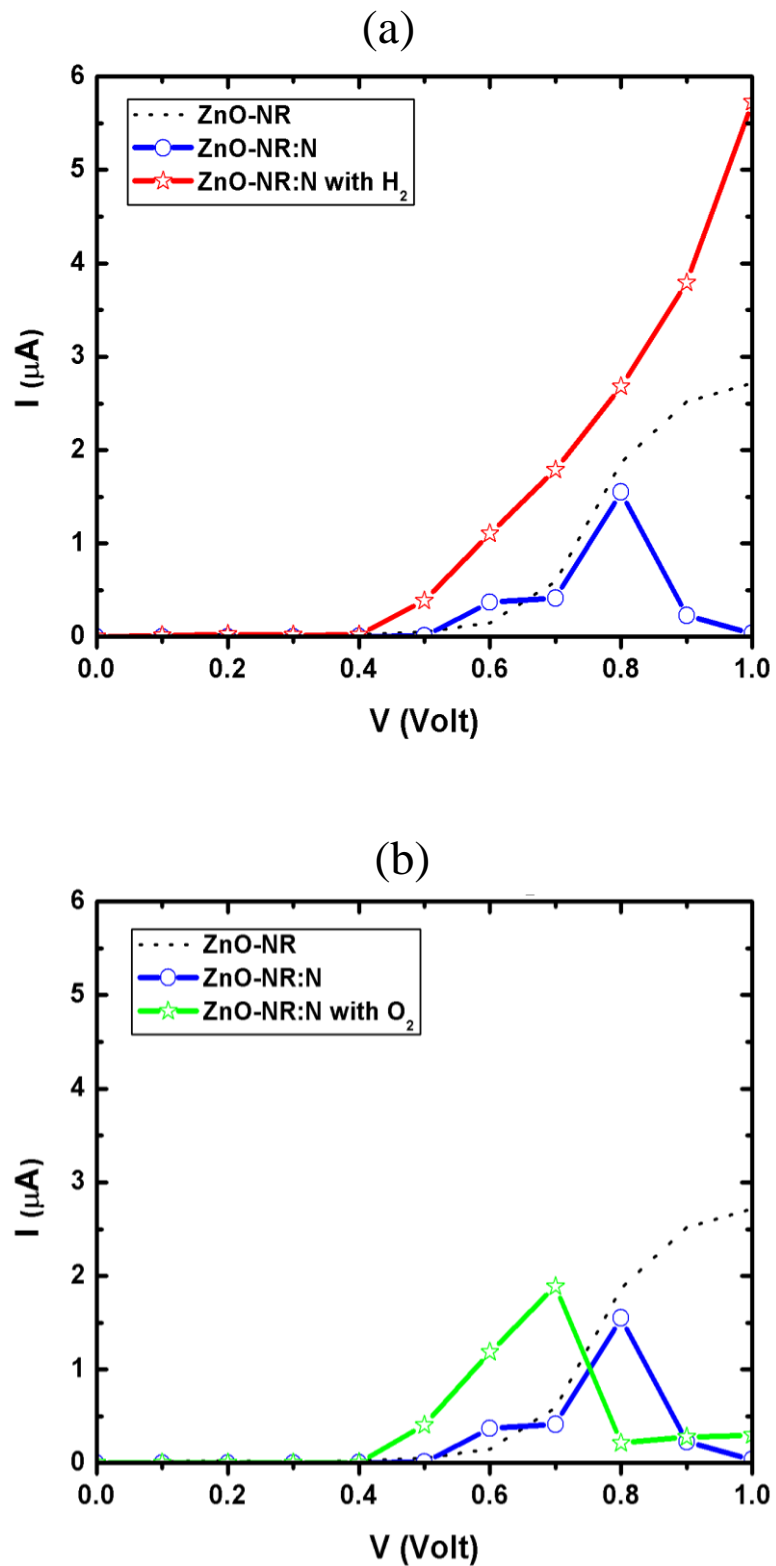
Figure 2.6 : IV Curves of ZnO-NR devices
(a) H_2 gas molecule (b) O_2 gas molecule on ZnO-NR:N device

2.7 Resistance and Sensor Response

Figure 2.7 displays the results of differential resistance versus bias for three devices whose central regions are consisted of: (a) ZnO-NR:N; (b) ZnO-NR:N after chemisorption of H_2 molecule; (c) ZnO-NR:N after chemisorption of O_2 molecule. Obviously, the NDR exists in the adsorbing bed before the landing of any molecule as shown in Figure 2.7(a). It is likely attributed to the unpaired electron on the nitrogen atom substituting oxygen as the N-atom has 5 electrons whereas O-atom has 6 electrons in the outer shells, respectively. Such nitrogen doping likely causes the formation of somewhat a dangling bond ready to capture electron whenever is passing through. The amazing thing happens when the device is exposed to a reduced gas such as H_2. The chemisorption associated with dissociation of H_2 molecule makes the H-atoms donate enough charge to the surface not only to saturate the N-dangling bonds but rather to raise the DOS at Fermi level and to enhance the conductivity. So, the NDR behavior disappears as can be seen in Figure 2.7(b). The decrease of resistance versus bias shown in Figure 2.7(b) might be attributed to the occurrence of resonances between the extended defect states and the states in the leads. Whereas, the chemisorption of an oxidizing-gas molecule, such as O_2 makes the sample more depleted from charge carriers and, consequently, would extend NDR region as shown in Figure 2.7(c). As a matter of fact, both oxygen is more electro-negative than the nitrogen atom so that it would drain charge from the surface to the molecule, reduce the DOS at Fermi level, and extend the NDR zone (i.e., zone between optima of IV curve). Yet, compared to the original NDR of the device, NDR magnitude is less as it occurs near optima of IV curve (maximum and minimum of I versus V). Overall, in both chemisorption cases H_2 and O_2, the differences between NDR before and after

the landing of molecules are so large with respect to the case after the devices' capture of molecule. Hence, such discrepancy would cause huge response function (i.e., enormous sensitivity as will be discussed next).

Figures 2.8(a) and 2.8(b) display the results of sensor response (sensitivity) versus bias for the two chemisorption cases of H_2, and O_2. The average value of sensitivity in case of chemisorption of H_2 $S_{ave}(H_2) = 3.92$ is higher than the one case of chemisorption of O_2, which is $S_{ave}(O_2) = 3.09$. This is expected and should be attributed to the fact that the adsorption of H_2 is associated with a dissociation of the molecule and a formation of an extended defect in vicinity of N-site. On the other hand, chemisorption of O_2 is weaker with possible desorption easy to occur/achieve.

(a)
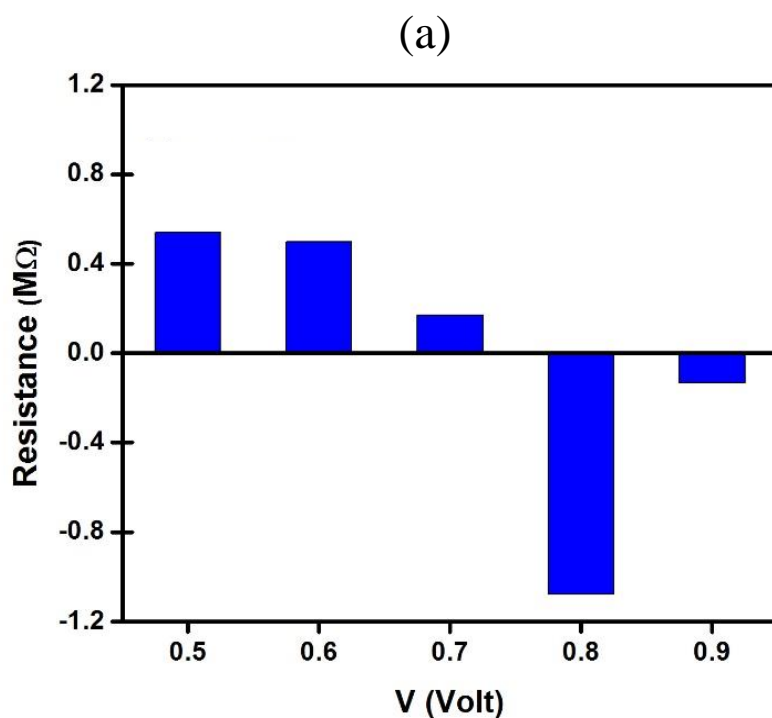
Figure 2.7 : Differential Resistance of ZnO-NR devices
(a) N-doped ZnO-NR device (b) H_2 molecule on ZnO-NR: N device (c) O_2 molecule on ZnO-NR: N device.

(b)

(c)
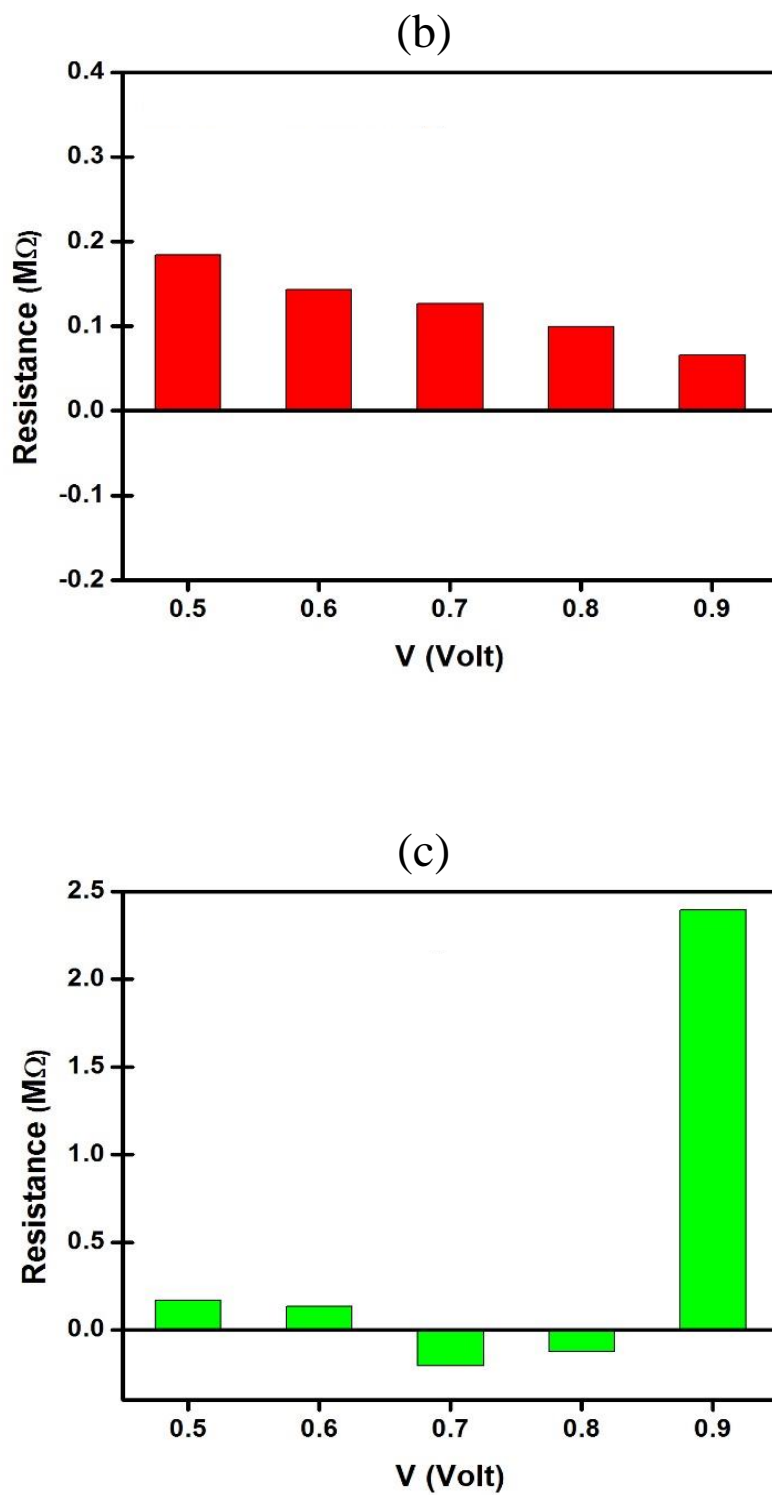
Figure 2.7 : Differential Resistance of ZnO-NR devices (continued)
a) N-doped ZnO-NR device (b) H_2 molecule on ZnO-NR: N device (c) O_2 molecule on ZnO-NR: N device.

(a)

(b)
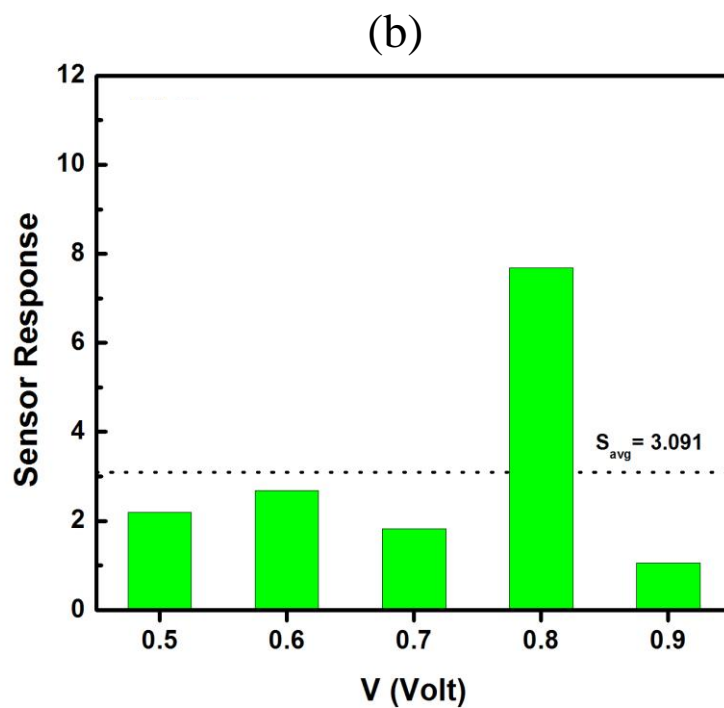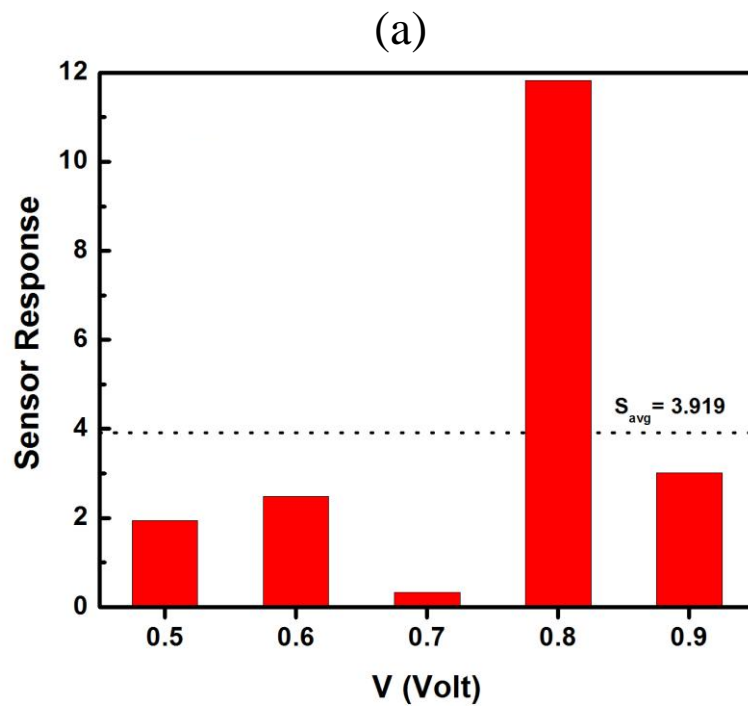
Figure 2.8 : Sensor response of ZnO-NR devices
(a) H_2 molecule on ZnO-NR: N device (c) O_2 molecule on ZnO-NR: N
device.

2.8 Combined Defect and Doping Effects

Intrinsic defects of oxygen vacancy (Vo) in metal oxide are common. Here, we study the effect of both defects and dopants existing at the same time. Figure 2.9 displays the IV curves for three devices whose central regions are: (a) ZnO-NR with Vo in black dotted curve; (b) ZnO-NR:N with Vo in blue solid curve; and (c) ZnO-NR:N with Vo after chemisorption of H_2 molecule in red solid curve. No NDR behavior is there in the red curve because the oxygen vacancy is known to play a role of donor and thus pays of the lack of charge due to both oxygen vacancy and nitrogen doping. It is clear that the red curve is larger than the blue one (which has already been amplified be x10). Yet, the difference between red and blue curves is not as big as in case of NDR like Figure 2.7(a) and Figure 2.7(b) So, in Figure 2.10, sensitivity is displayed versus bias. The average sensitivity $S_{ave} = 1.43$ is less than the cases without oxygen vacancy. One can comment on both blue and red curves as follows: (i) In case of co-existence of oxygen vacancy with N-dopant, there are at least two dangling bonds in the system (one on N-atom and one in the vicinity of oxygen vacancy). These defects create much localized state with a curdling/localized wave-function. They cause a large drawback in the electric current due to the back-scattering events. Basically, the current is at the critical value of Mott's minimum metallic conductivity (hard to detect experimentally). (ii) When the system is treated with hydrogen (H_2) and chemisorption took place, hydrogen atoms play the role of donors and saturate the two dangling bonds. Current become rectified and NDR gets eliminated.
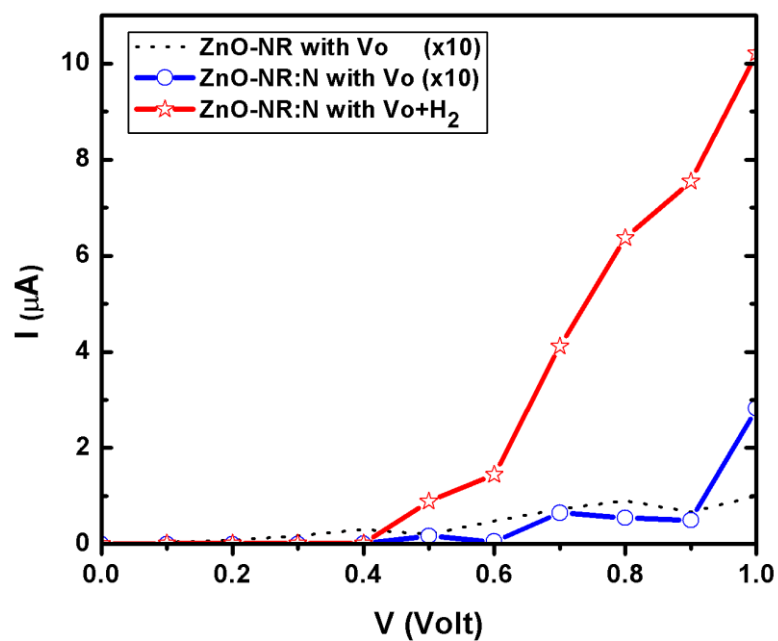
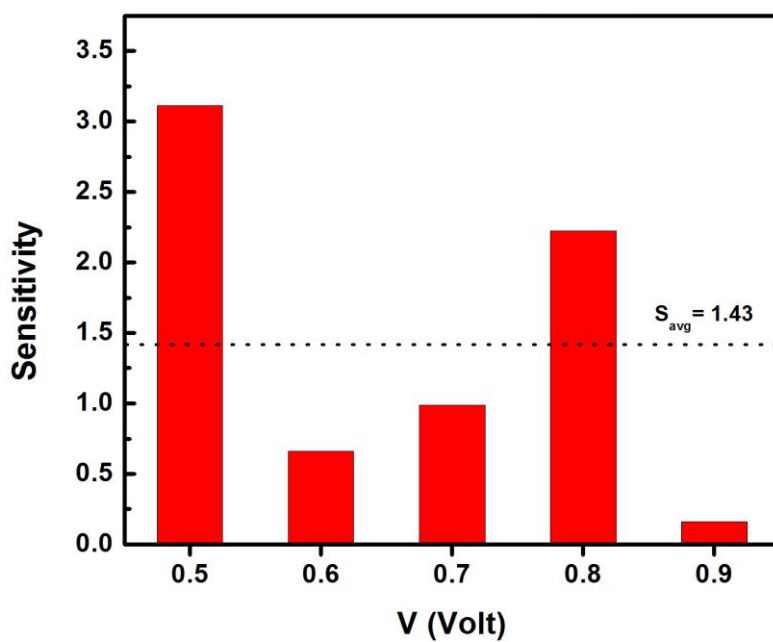Figure 2.9 : IV Curves of ZnO-NR device with V_O: H_2 gas molecule

Figure 2.10 : Sensor response of ZnO-NR device with V_O: H_2 gas molecule

Chapter 3: Origins of Negative Differential Resistance in ZnO-NR- N

3.1 Introduction

Negative differential resistance (NDR) and quantum tunneling were simultaneously discovered by Esaki in 1958 and earned him Nobel Prize in Physics in 1973. The discovery gave birth to new electronic devices starting from Esaki Diode (i.e., "tunnel diode"). Subsequently, J.B. Gunn discovered the Gunn's effect in 1962, when he observed random noise-like oscillations, validated by the existence of NDR, after applying a bias on n-type GaAs samples and crossing a certain voltage threshold. In the present chapter, NDR took place in ZnO-NR:N devices (see Chapter 2). As it is very important to many applications beyond gas sensing, we focus on studying its origins (cause and mechanisms) in the present chapter. NDR should take place in nano-devices as a collective manifestation of quantum coherence and statistical mechanics.

Three different devices are placed under the scope, in which single N-atom is placed to replace 1 native oxygen atom in the central zone of the device but in three respective locations with respect to the edges: (i) at the oxygen-rich edge, (ii) at the center, and (iii) at the zinc-rich edge. The universal conductance fluctuations are averaged using phase averaging so that the fluctuation obtained are physical. All three devices exhibit NDR. We will show that the cause of such NDR is the existence of unpaired electron in N-atom, which causes the curdling/localization of wave-function; that in turn causes a lot of back-scattering events. Such back scatterings cause suppression of conductive channels and thus a drawback in the electric current (that is named NDR).

3.2 Transport Properties of ZnO-NR Devices

A combination of DFT and NEGF methods is applied to investigate the transport properties of N-doped ZnO-NR based devices. Figure 3.1 presents the ZnO-NR:N devices in which nitrogen dopant is located at (a) Upper edge; (b) Center; (c) Lower edge .
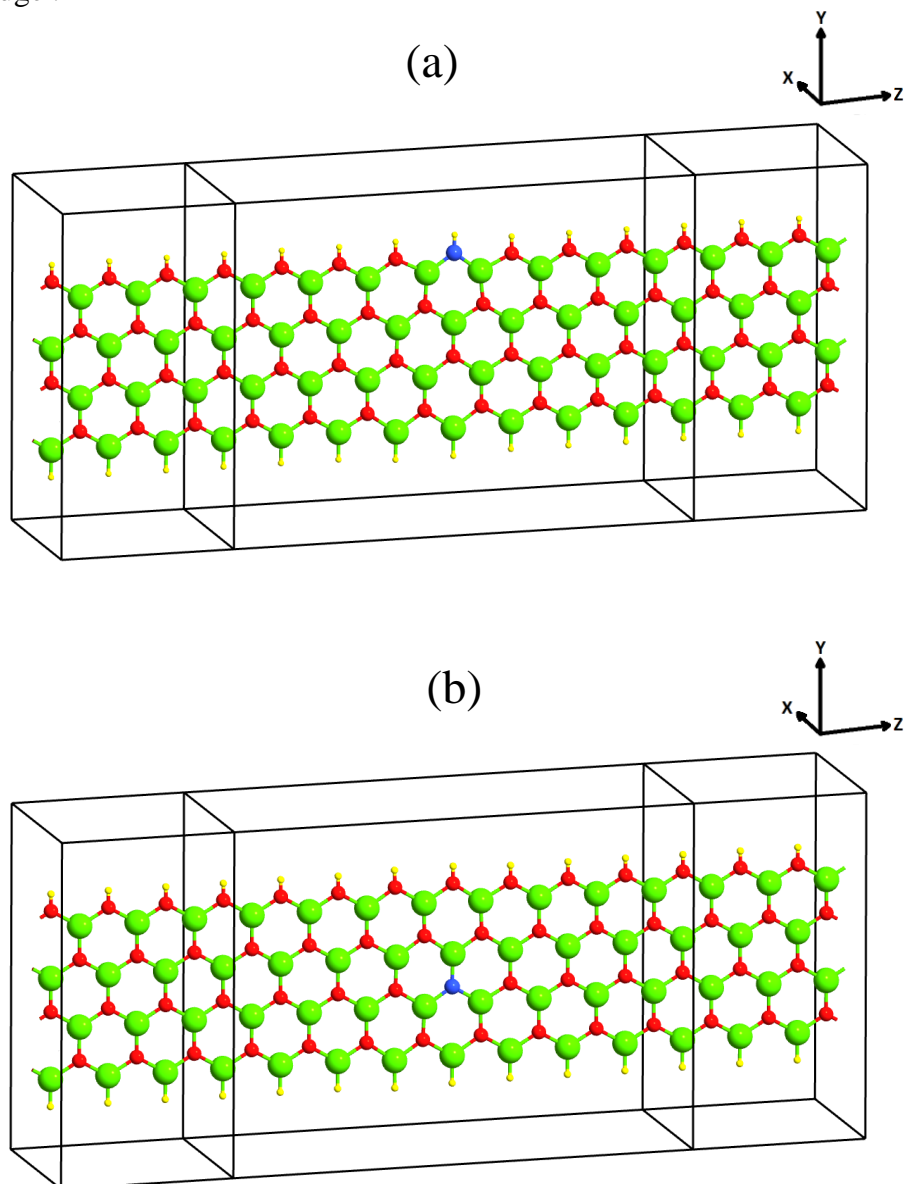

Figure 3.1 : Relaxed Structures of ZnO-NR:N devices
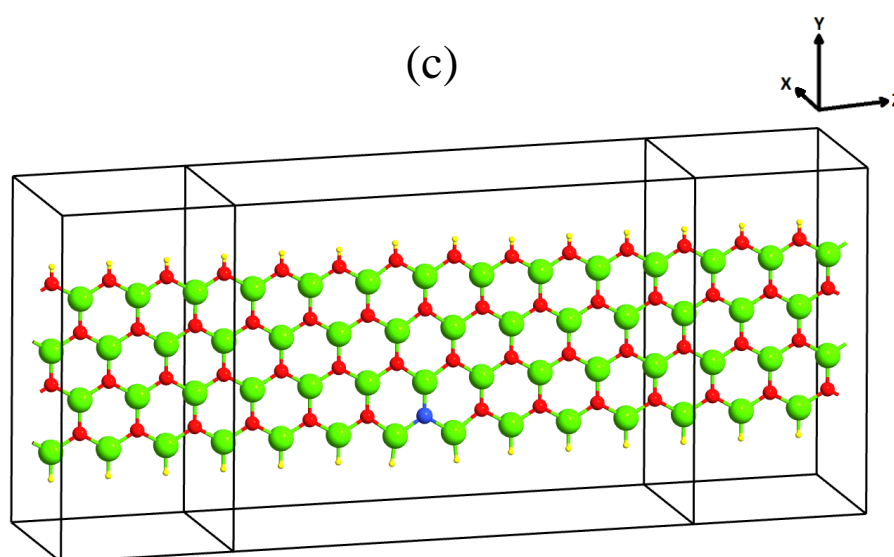(a) N at Upper edge (b) N at Center (c) N at Lower edge

(c)

Figure 3.1 : Relaxed Structures of ZnO-NR:N devices (continued)
(a) N at Upper edge (b) N at Center (c) N at Lower edge

Figure 3.2 and 3.3 displays the results of IV curves and device density of states

(DDOS) for three device samples of N-doped ZnO-NR, where N-atom is located at:

(i) the upper edge of NR along oxygen chain and surrounded by 2 hydrogen atoms and

1 zinc atom; (ii) the center of NR surrounded by 3 zinc neighbors; and (iii) the lower

edge of NR surrounded by 3 zinc neighbors. Figure 3.2 displays the IV characteristics

of these respective three samples in solid curves, whereas the dotted curve,

corresponding to the IV characteristics of pristine ZnO-NR, is shown just as a

reference. The three devices with N doping show evidence of NDR behaviors. Figure

3.3 displaying DDOSs, calculated at zero bias ($V = 0$) for the same three devices, show

that both the device band gap and Fermi level being invariant when the impurity N

changes its location (i.e., $Eg \approx 0.43$ eV remains the same). Perhaps the only residual

difference occurs in the filling of the conduction band edge (i.e., the LUMO state),

whose density of states increases as the N moves toward lower edge of NR.
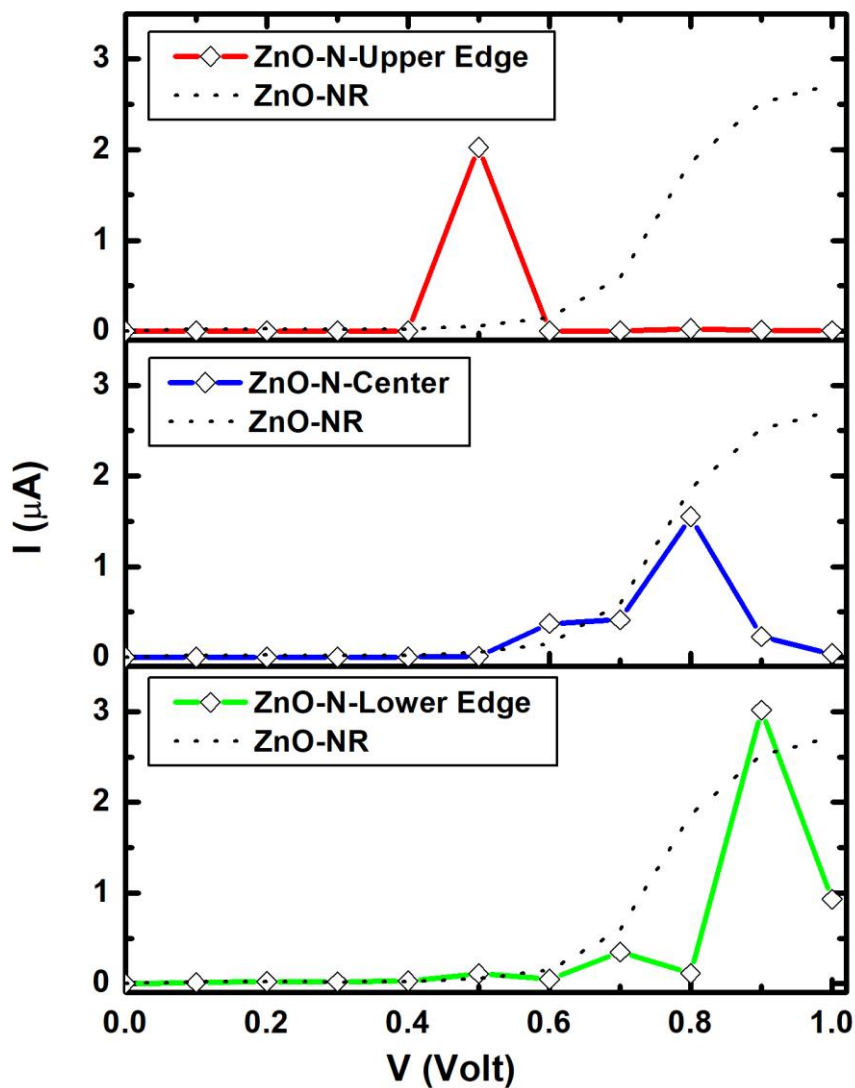
Figure 3.2 : IV Curves of ZnO-NR:N devices

The black dotted curve represents IV curve for pristine ZnO-NR. The red curve represents IV for N-doped at upper edge of the ZnO-NR. The blue curve represents IV curve for N-doped at the center and the green curve represents IV curve for N-doped at the lower edge of the ZnO-NR.
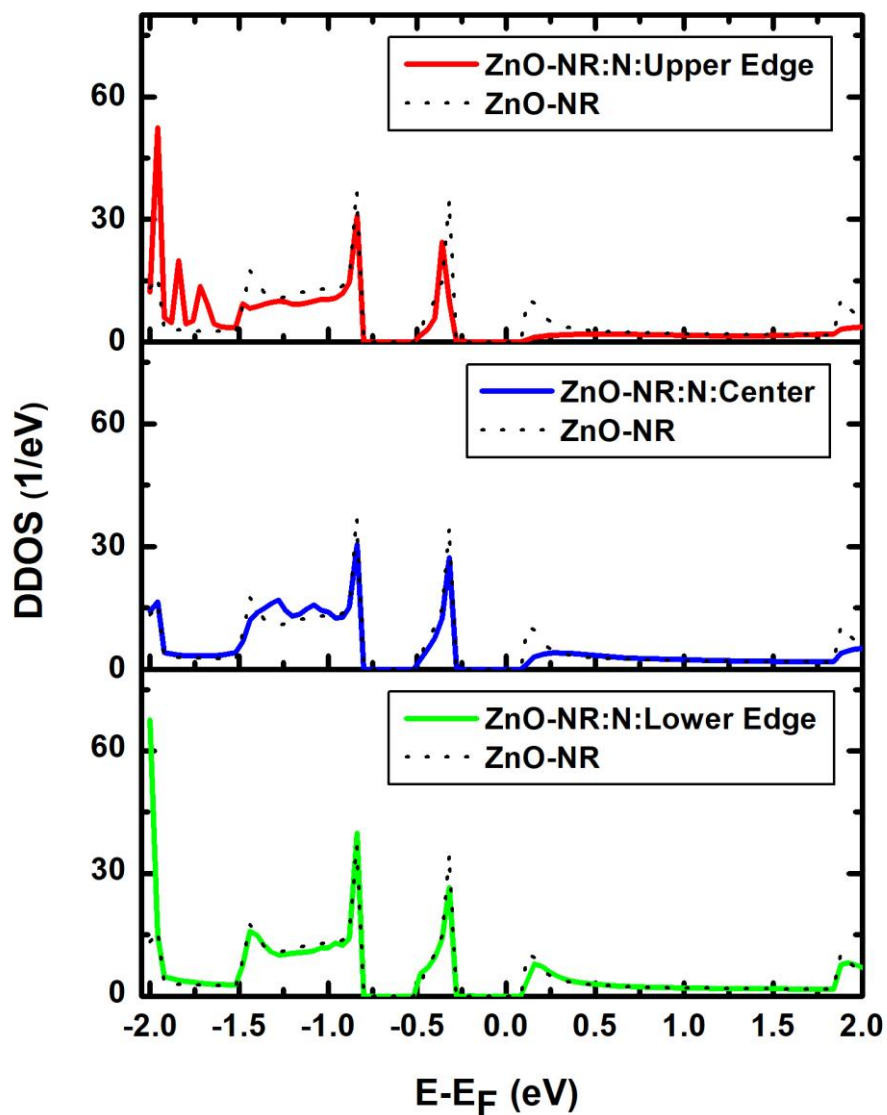
Figure 3.3 : Device Density of States (DDOS) of ZnO-NR:N devices
The black dotted curve represents DDOS for pristine ZnO-NR. The red curve represents DDOS for N-doped at upper edge of the ZnO-NR. The blue curve represents DDOS for N-doped at the center and the green curve represents DDOS for N-doped at the lower edge of the ZnO-NR.

Within the interval [0,1] Volt, Figure 3.2 shows the occurrence of maximum current at biases 0.5 V, 0.8 V and 0.9 V in the three devices, respectively. The top-to-valley current ratios (TVCRs) for these devices are: 5549, 6.8, and 3.2, respectively. It seems that as soon as the bias crosses the threshold of bandgap to yield an electric current, some conduction band channels get suppressed and such suppression does depend on the location of the impurity N-atom with respect to the NR-edges. One may summarize the following scenarios to simultaneously take place: (i) N has five electrons in its outer shell and its substitutional doping to oxygen (which has 6 electrons in its outer shell) would yield an unpaired electron to form like a dangling bond on the N dopant; somehow like a p-type doping (see discussion on the electronic structure below). Nonetheless a compromised effect can take place as the dangling bond needs one electron to become saturated/passivated while this electron makes the site negatively charged and repel the other electrons to come close. (ii) Unlike the atoms at the body of the nanoribbon, the hydrogen atoms at the edges have weak bonds and electrons there do predominantly populate Fermi level. The current density should be very high at the edges of the nanoribbon as they provide very conductive channels with less impedance, especially on the oxygen-rich edge. (iii) Having said these, it seems that moving N-atom toward the oxygen edge would cause high impedance and high TVCR, which are attributed to the suppression of many conductive channels as it is illustrated in Figure 3.4 (next discussion).

Figure 3.4 displays the transmission coefficient versus energy for various biases ramping from 0.5 V to 0.9 V for four devices, including (a) pristine ZnO-NR and (b-d) N-doped ZnO-NR with N-atom changing position from upper edge to center then to lower edge, respectively. Fermi energy is taken as an energy reference ($E_F = 0$). Even though the bias crosses the bandgap of the scattering zone (i.e., $E_g \approx 0.44$

eV), concerning conduction, many bands along the NR seem to be not penetrating and just to form suppressed channels. Figure 3.4(a), corresponding to pristine ZnO-NR, focusing at energy region around Fermi level, a conduction channel starts to develop when the bias reaches V = 0.7 V. Consistently, in Figure 3.2, as shown in dotted curve, the current starts growing at the same bias (0.7 V). Figure 3.4(b), corresponding to N-doped ZnO-NR with N-atom being placed at the upper edge of NR (i.e., along the oxygen-edge), near Fermi level, there exist just one conduction channel when a voltage V = 0.5 V is applied. No other conduction channels exist when a bias V in the range 0.5 < V ≤ 1.0 V is applied. Although DDOS of this device, shown in Figure 3.3, show the evidence of existence of quantum states in this energy interval; yet its seems that those states are quantum-mechanically curdled or confined due to the effect of defect (impurity blocking the conduction states "LUMO", see below for more details). It is amazing that LUMO states percolated the current at such bias V = 0.5 V then higher CB states seem either having flat band (not conductive channels) or not in resonance with Fermi levels of the two leads. Figure 3.4(c), corresponding to N-doped ZnO-NR with N-atom being placed at the center of NR, focusing on energy region around Fermi level, a conduction channel starts to develop at a bias V = 0.6 V, then it gets closer to E_F with larger amplitude when bias V = 0.8 V. Corroborated with this, the current reaches its maximum value at V = 0.8 V in Figure 3.2 (central panel). At such bias, one expects good connection between Fermi levels from leads to scattering region meanwhile the ZnO-NR's band at Fermi level to be dispersive (conducting). Figure 3.4(d), corresponding to N-doped ZnO-NR with N-atom being placed at the lower edge (near Zn-edge), within the energy region around Fermi level, It shows a small peak when V = 0.7 V and further develops into a much larger peak when V = 0.9 V. Consistent with these two peaks, the IV characteristics of this device

(shown in lower panel of Figure 3.2), shows accordingly two peaks at V = 0.7 V and 0.9 V, of small and large amplitudes, respectively.
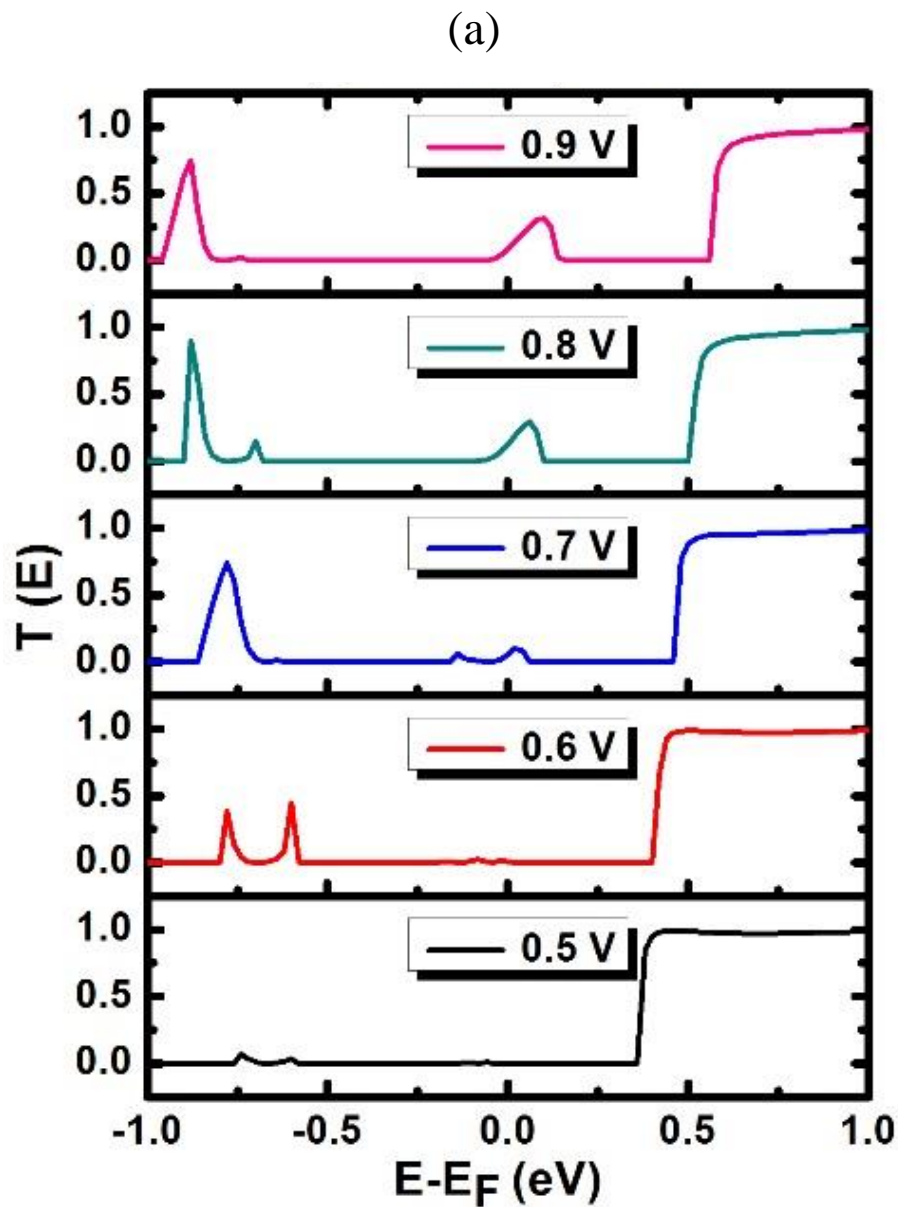
(a)

Figure 3.4 : Device Transmission Coefficient T(E) of ZnO-NR:N devices (a) Pristine ZnO-NR (b) N at upper edge on ZnO-NR (c) N at center on ZnO-NR (d) N at lower edge on ZnO-NR.
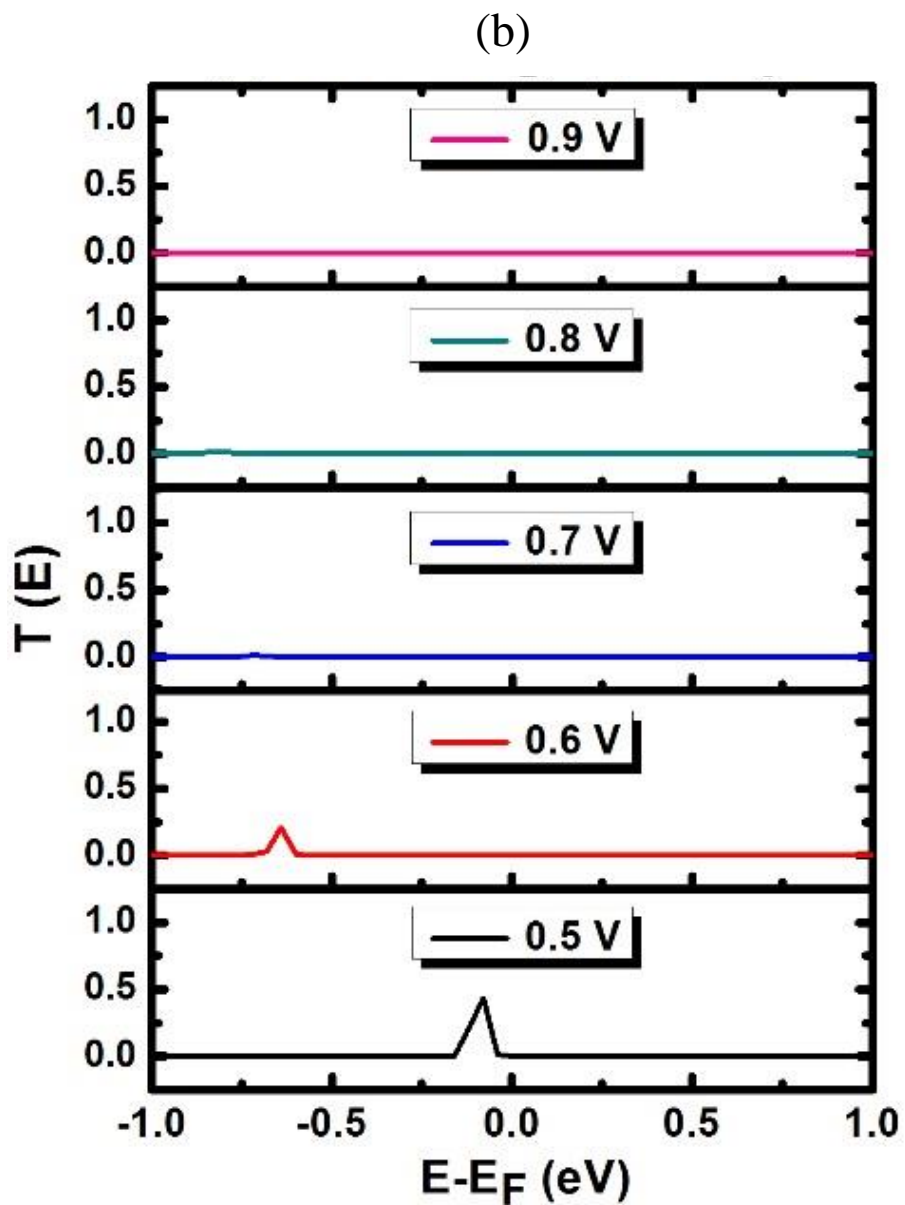
(b)

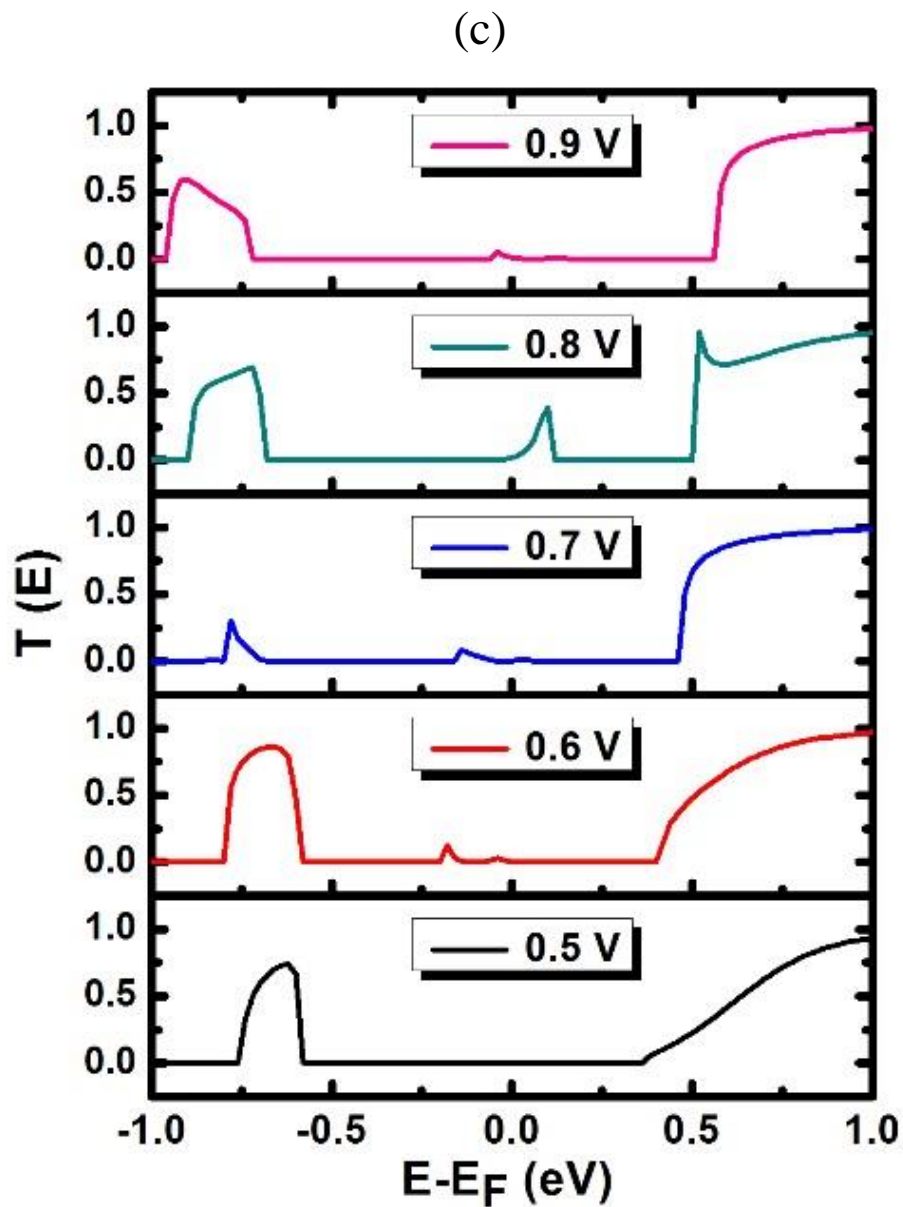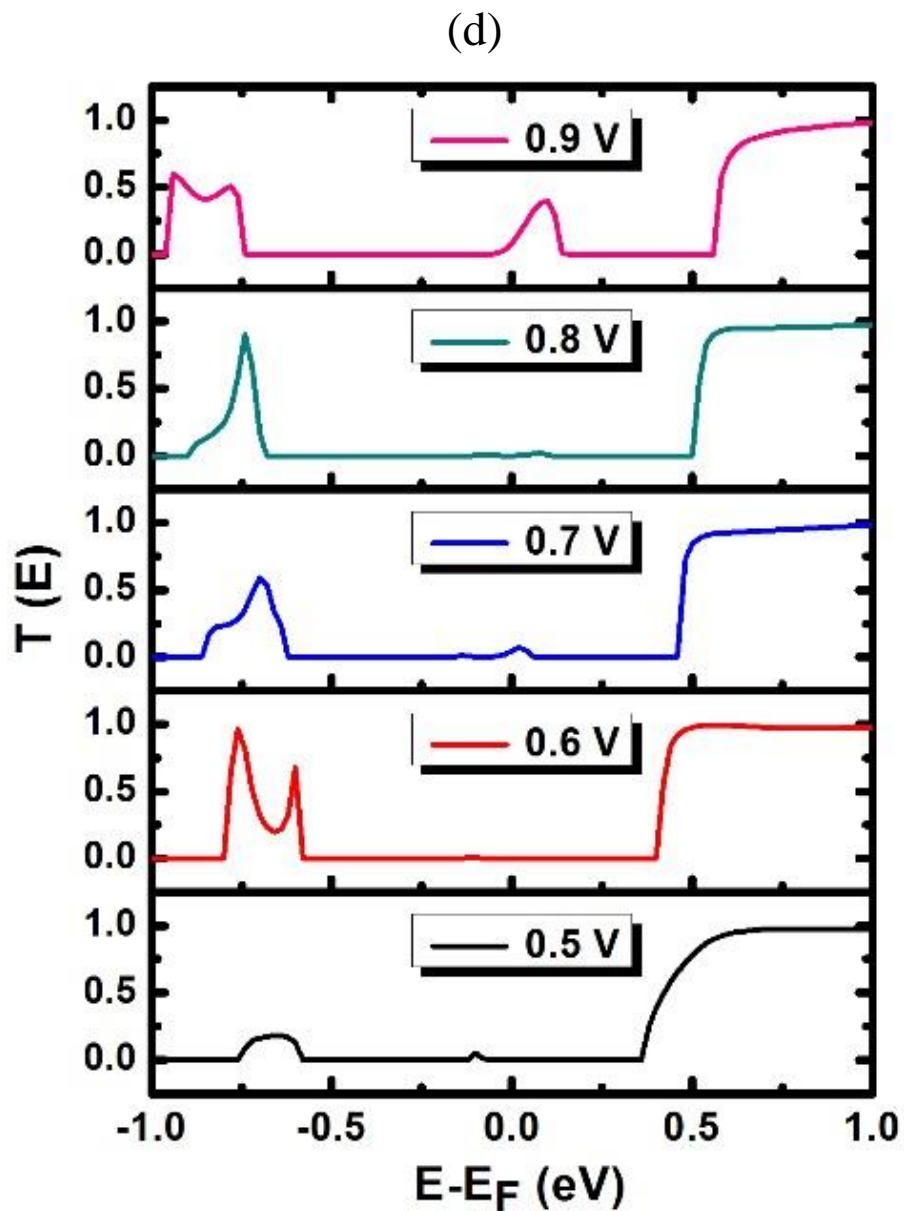Figure 3.4 : Device Transmission Coefficient T(E) of ZnO-NR:N devices
(continued)
(a) Pristine ZnO-NR (b) N at upper edge on ZnO-NR (c) N at center on
ZnO-NR (d) N at lower edge on ZnO-NR.

(c)

Figure 3.4 : Device Transmission Coefficient T(E) of ZnO-NR:N devices
(continued)
(a) Pristine ZnO-NR (b) N at upper edge on ZnO-NR (c) N at center on
ZnO-NR (d) N at lower edge on ZnO-NR.

(d)

Figure 3.4 : Device Transmission Coefficient T(E) of ZnO-NR:N devices
(continued)
(a) Pristine ZnO-NR (b) N at upper edge on ZnO-NR (c) N at center on
ZnO-NR (d) N at lower edge on ZnO-NR.

The differential resistance is calculated using the results of IV curves, shown in Figure 3.2. Figure 3.5 displays the differential resistance versus bias for the four devices, which were discussed in the previous figure. Figure 3.5(a), corresponding to pristine ZnO-NR, shows the differential resistance calculated for the bias interval 0.5 ≤ V ≤ 0.9 V. The pristine sample is clear of NDR behavior and the differential resistance is always positive. As it is revealed in the IV characteristics, the differential resistance starts large as soon as current starts flowing in the device (as V crosses Eg), then reduces to a minimum at a bias of about V = 0.8 then raises again. Figure 3.5(b), i.e., corresponding to ZnO-NR:N with N-atom at upper-edge of NR, shows the highest NDR with an algebraic value of about – 9 MΩ when a bias V = 0.9 V is applied. Figure 3.5(c), corresponding to ZnO-NR:N with N placed at center of NR, has NDR smaller in magnitude than the case of (b), as N-atom is displaced from upper edge toward the center of NR. The minimum value of NDR is about – 1.0 MΩ, which is achieved under bias V = 0.8 V. Figure 3.5(d), corresponding to ZnO-NR:N with N-atom placed at lower edge of NR (i.e., near Zn-edge), has the smallest NDR in magnitude, whose algebraic value is of about -0.25 MΩ, to occur when a bias of 0.9 V is applied. Thus, there is a reduction in the magnitude of NDR when the N-dopant is moved from upper to center to lower edge of NR revealing that the conduction is predominantly carried out by the oxygen edge in the absence of dopant. The channel gets blocked when the N-atom is placed there.
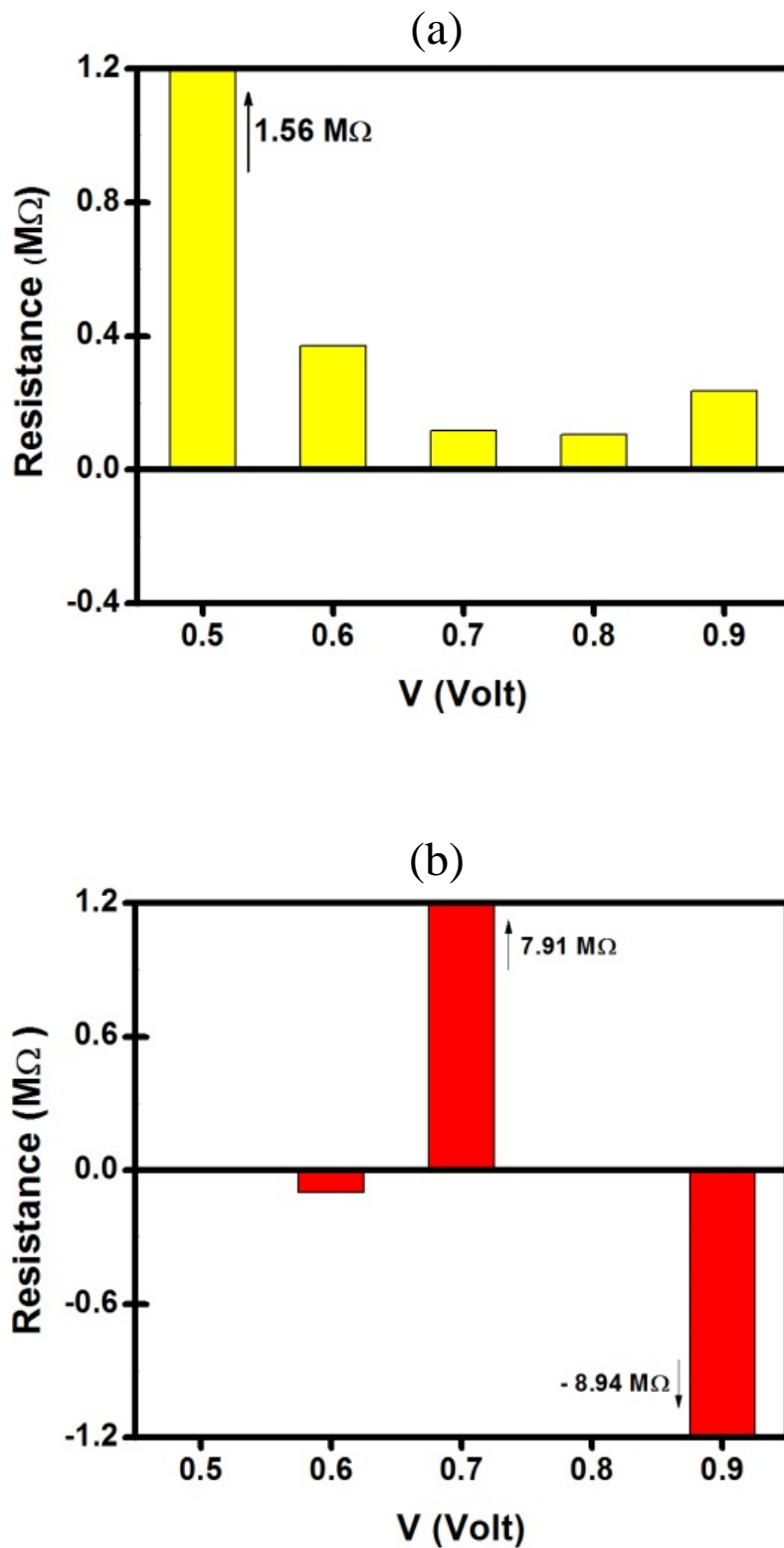
Figure 3.5 : Differential Resistance of ZnO-NR:N devices
(a) Pristine ZnO-NR (b) N at upper edge (c) N at center (d) N at lower edge
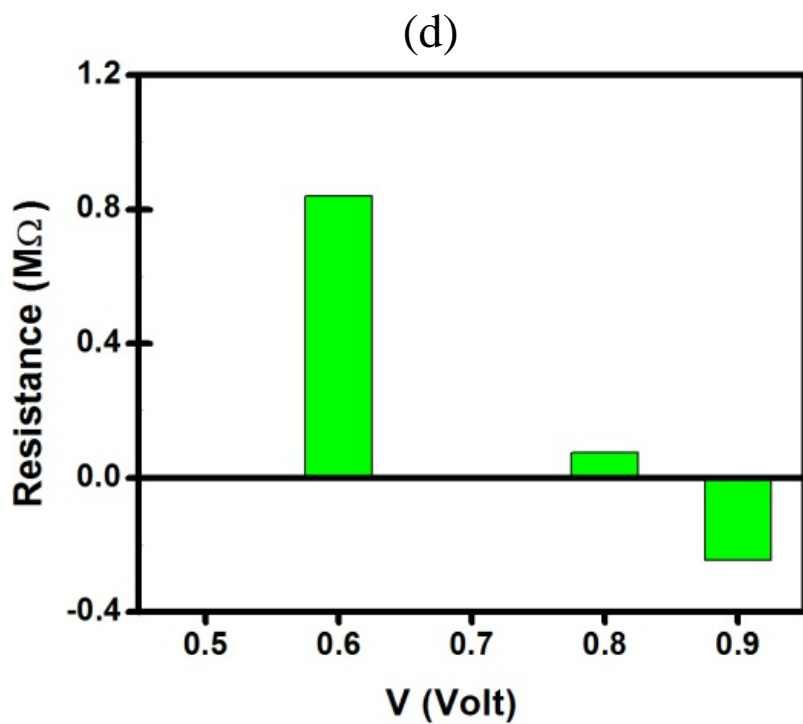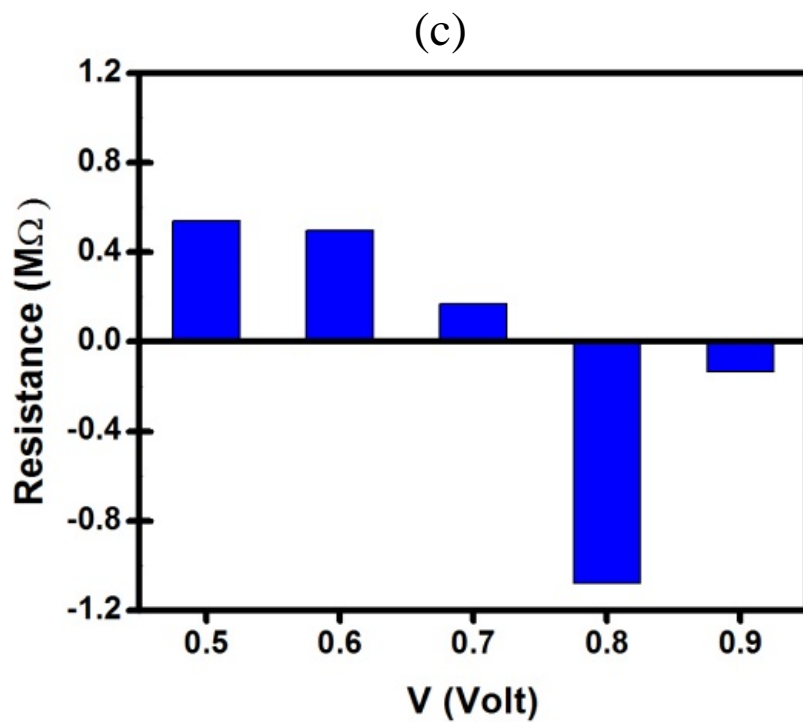
(c)

(d)

Figure 3.5 : Differential Resistance of ZnO-NR:N devices (continued)
(a) Pristine ZnO-NR (b) N at upper edge (c) N at center (d) N at lower edge

3.3 Electronic Properties of ZnO-NR Devices

Using DFT without NEGF methods, one can study pristine and N-doped ZnO-NR samples without the inclusion of electrodes. Such investigation constitutes another perspective or approach in understanding the origins and possible mechanisms causing the NDR in devices. Four samples, consisting the scattering regions of devices shown in Figure 3.1, in addition of the case of pristine ZnO-NR, have been relaxed and used in the calculations of bands and charge densities. Figure 3.6 shows the band structures of the four samples, where periodic boundary conditions were applied only along the z-direction. The results show the following: (i) In case of pristine ZnO-NR shown in Figure 3.6(a), the bandgap energy is $Eg = 0.533$ eV and Fermi level lays in the middle of the gap as in intrinsic semiconductor. The conduction bands look dispersive. Holes likely have heavier masses than electrons. (ii) In cases of N-doped ZnO-NR shown in Figure 3.6(b). 3.6(c), and 3.6(d), the bandgap energy reduces from $Eg = 0.916$ eV, to 0.533 eV and to 0.384 eV when the N-dopant is moved from upper edge to center then to lower edge of the NR, respectively. (iii) Fermi level lays near the valence band (VB) edge, which reveals that N dopant is playing the role of an acceptor. (iv) only the lowest conduction band appears to be flat, as it attributed to a localized state/orbital on a defect. The lowest CB becomes more dispersive as N-atom is moved toward lower edge of NR. (v) Many valence bands appear to be flat and get rather discretized in energy as N-atom is moved toward the lower edge. This discretization of top VBs is attributed to quantum-confinement effect. Apparently, charge get more and more localized around N-dopant when it is moved further downer close to the lower edge (see below for more details in the charge-density plots).
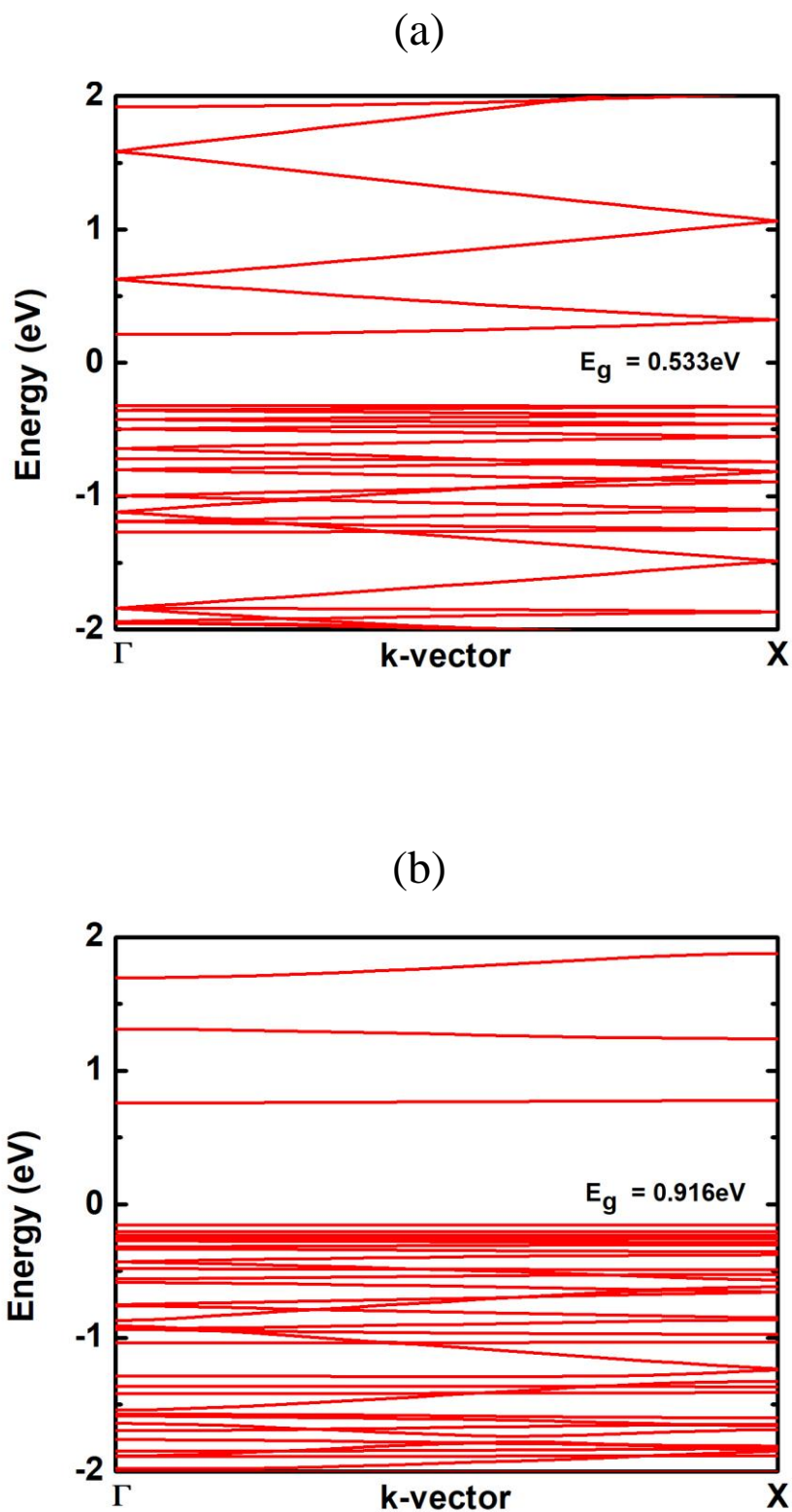
(a)

(b)

Figure 3.6 : Band Structure of ZnO-NR:N devices
(a) Pristine ZnO-NR (b) N at upper edge (c) N at center (d) N at lower edge
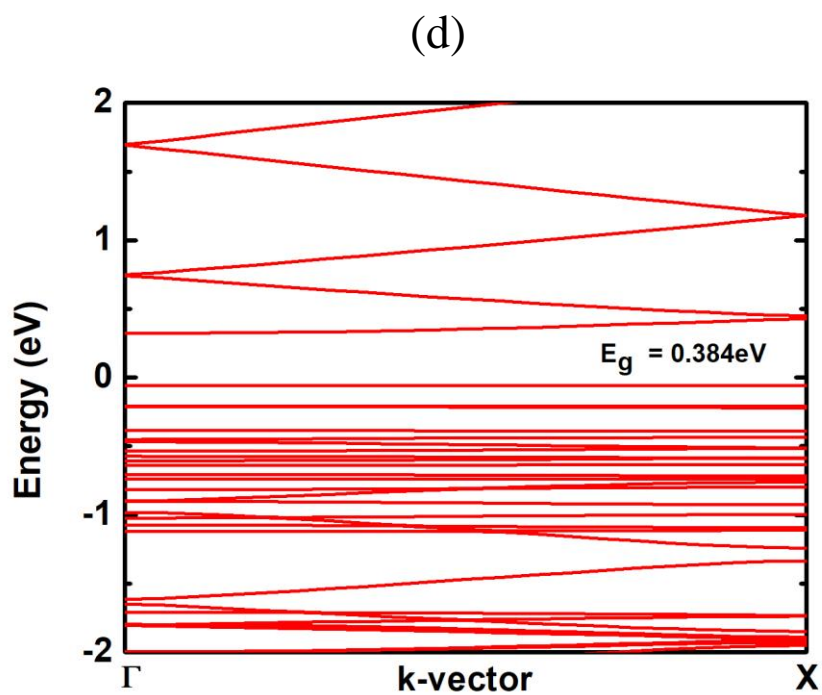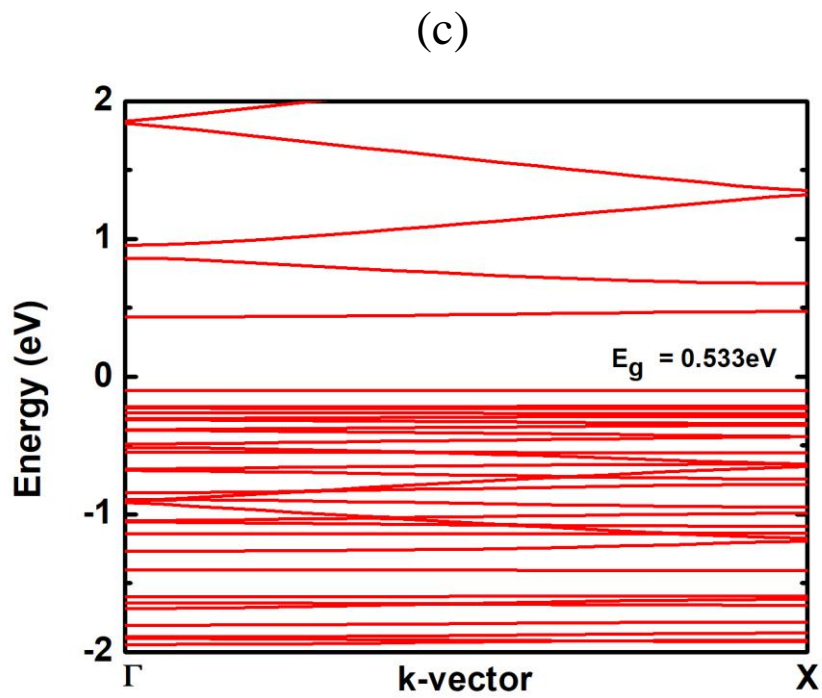
(c)

(d)

Figure 3.6 : Band Structure of ZnO-NR:N devices (continued)
(a) Pristine ZnO-NR (b) N at upper edge (c) N at center (d) N at lower edge

Figure 3.7 displays charge density plots of probability density of both the highest occupied molecular orbital (HOMO) and the lowest unoccupied molecular orbital (LUMO) for the three samples under focus as well as pristine ZnO-NR, which is taken as a reference. Both side and top views are shown. The probability density is shown in blue color. (a) In case of pristine ZnO-NR, both HOMO and LUMO are Bloch-like states being extended along z-direction. Notably, the HOMO is supported by the Zn-sites located at lower edge. Likely, Zn-atom has its d-states completely filled and should be deep in energy, laying much below the Fermi level, that can be considered as core states [53]. Meanwhile as far as the covalent bonding is concerned, the external s-states of Zn-atoms are predominantly contributing to the composition of the valence band. This picture (Figure 3.7(a) HOMO) reveals that the Zn-H bonds are weaker than the O-H bonds and the former do populate the HOMO states just below Fermi level. This is consistent with the bond-dissociation energies reported by Luo: E_b(Zn-H) = 0.89 ± 0.02 eV/bond being weaker than E_b(O-H) = 4.461 ± 0.003 eV/bond. On the other hand, the LUMO state should be predominantly populated by O-sites, especially those near O-H at the upper edge. Consequently, the conduction is expected to be carried out by these oxygen atoms at the upper edge. (b) In case of ZnO-NR with N dopant located at upper edge, the HOMO remains to be supported by the weakest Zn-H bonds (i.e., by Zn-located at lower edge) but the LUMO gets fragmented on both sides, with respect to z-direction, of the sample as indication of scattering due to defect. This fragmentation is the reason why the lowest CB in Figure 3.6(b) to be flat. (c) In case of ZnO-NR, with N-atom being moved to the center, the high electronegativity of N-atom starts playing a role so that the HOMO state gets clustered around the N-site. This charge confinement causes the top VB to become discretized and flat, as shown in Figure 3.6(c). For the LUMO state, the charges still behave like

in previous case being fragmented on both sides, along z-direction, of the ZnO-NR. Such fragmentations of LUMO cause the lowest CB to remain flat. (d) In case of ZnO-NR, with N dopant being placed near the lower edge, the confinement of HOMO state at N-dopant's vicinity becomes even stronger. Consequently, more bands become flat at the top of VB with clear discretization, as shown in Figure 3.6(d). The LUMO becomes less fragmented than before, as N-dopant moved away from the O-edge originally confining the LUMO state. Consequently, kind of a small dispersion in the lowest CB starts to appear, revealing a bit delocalization of LUMO state as corroborated in Figure 3.6(d).
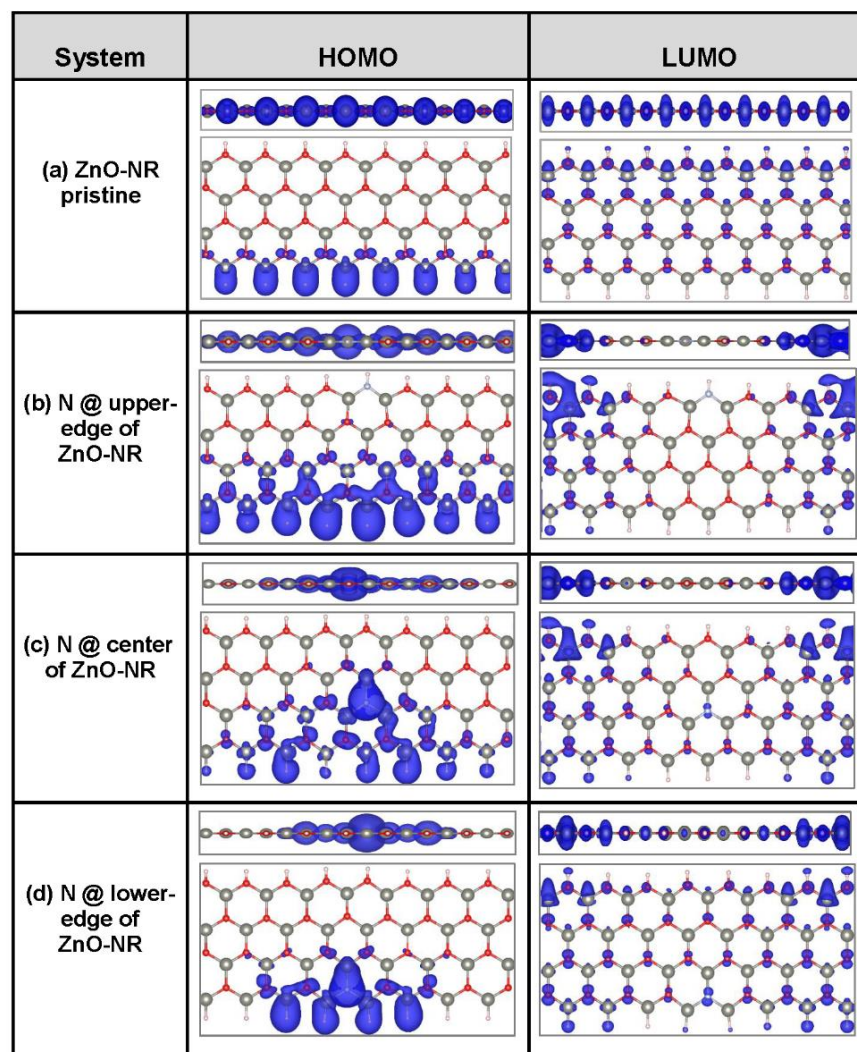
Figure 3.7 : HOMO and LUMO eigen-states of ZnO-NR:N devices

Chapter 4: Effect of Catalyst on Gas Sensing ZnO-NR- Catalyst

4.1 Introduction

This chapter deals with effect of catalysts on the gas sensing performance of ZnO nanoribbons using the same ATK-package. This work has been possible due to the installation of the ATK package in HPC at the UAEU with 512 parallel processors. So, this allows us to handle both the extension of the NR to become of sufficient length recommended in the package as well as to deal with transition metal atoms (e.g., Pt, Pd, Au, Ag and Fe) which we plan to use as catalysts. We had the opportunity to test the adsorption of many gases (e.g., H_2, H_2S, H_2O, CO_2, N_2, O_2). Actually, our plan is to search for the right catalysts to yield high selectivity toward three target gases (H_2, H_2S and CO_2), which are of great importance in energy and environmental sectors. Our package allows us to study both the adsorption and transport properties at room temperature (RT). Of course, while we carry on our calculations, experimental data are needed for benchmarking our findings. We have found some data available in the literature and we will show that our theoretical results are in good agreements with the experimental data.

Our theoretical results show that both Pt and Pd exhibit chemisorption with all gases at RT, but they have poor selectivity. This is consistent with experimental data that Pt reaches its highest selectivity at high temperature $T = 400$ ºC. Two catalysts (Au and Ag) show good selectivity towards detecting H_2S at RT. Whereas, Fe yields a selectivity towards detecting CO_2 at RT. These are corroborated with experimental evidence.

4.2 Atomic Relaxation

Seeking to reach the selectivity towards a specific gas, many transition metal atoms (e.g., Pt, Pd, Au, Ag, and Fe) are considered as catalysts deposited on ZnO-NR. Total energy calculations show that the deposition on hollow sites would yield the most stable configuration having strongest magnitude of binding energy. On these catalysts many gas molecules (e.g., H_2, H_2S, H_2O, N_2, O_2, CO_2) are considered in the study of adsorption. Nevertheless, in our focus, more interest is given basically to H_2, H_2S and CO_2 because of their potential interest in both environmental and energy sectors. Throughout our current study, we shall investigate the reasons why or why not having selectivity.

Both 1D periodic samples and devices were relaxed and used in probing the adsorption and gas sensing properties. Figure 4.1 shows relaxed atomic structures of five devices before and after the adsorption of gas molecules. Each device is composed of 1-atom-thick layer of ZnO nanoribbon (ZnO-NR). The thickness of NR is kept as narrow as to comprise 3 hexagons (i.e., 4 conducting channels). Regarding the chemisorption of hydrogen gas (H_2 molecule), it is shown to be associated with the dissociation of the molecule on both Pt and Pd. The geometrical parameters (bond lengths and bond angles) are summarized in Table 5. Without the H_2 molecule, both Pt and Pd prefer relaxing on the hollow site. The chemisorption processes of H_2 molecule on both Pt and Pd are both associated with dissociation of molecule to make two covalent bonds with respective angles Ang(H-Pt-H) = 53º and Ang(H-Pd-H) = 33º. Both chemisorption processes made Pt and Pd having 4 bonds (2 bonds with underneath Zn-atoms and 2 separate bonds with H-atoms). Although both Pt and Pd belong to the same column in the periodic table, as being transition metals with

occupancy of d^8 in their d-shells, they are different in electronegativity (i.e., $\chi^{Pt} = 2.20$ Pauling $< \chi^{Pd} = 2.26$ Pauling). Moreover, the smaller is the angle the stronger the covalent bond with H-atom is. This will be further discussed under the light of binding energy and charge transfer later.

Table 5 : Geometrical parameters of relaxed structures of five devices with catalysts before and after the arrival of gas molecules.

	Catalyst on ZnO-NR	Gas Molecule on Catalyst on ZnO-NR
H_2/Pt	D(Pt-Zn) = 2.52 Å, 2.72 Å, 2.67 Å D(Pt-O) = 1.99 Å	D(Pt-Zn) = 2.57 Å, 2.80 Å D(Pt-H) = 1.57 Å Ang(H-Pt-H) = 52.83º
H_2/Pd	D(Pd-Zn) = 2.59 Å, 2.60 Å, 2.63 Å D(Pd-O) = N/A	D(Pd-Zn) = 2.58 Å, 2.62 Å D(Pd-H) = 1.67 Å Ang(H-Pd-H) = 33.00º
CO_2/Fe	D(Fe-Zn) = 2.29 Å, 2.49 Å, 2.50 Å D(Fe-O) = 1.74 Å, 1.75 Å	D(Fe-Zn) = 2.27 Å D(Fe-C) = 1.84 Å D(Fe-O1) =1.95 Å D(C-O) = 1.21 Å, 1.30 Å Ang(C-Fe-O1) = 39.98º Ang(O-C-O) = 139.41º, molecule
H_2S/Ag	D(Ag-Zn) = 2.82 Å, 2.82 Å D(Ag-O) = N/A	D(Ag-Zn) = 2.78 Å D(Ag-S) = 2.47 Å D(S-H) = 1.37 Å, 1.37 Å Ang(Zn-Ag-S) =146.16º Ang(H-S-H) = 91.54º, molecule
H_2S/Au	D(Au-Zn) = 2.58 Å, 2.59 Å, 2.85 Å D(Au-O) = N/A	D(Au-Zn) = 2.61 Å, 2.62 Å D(Au-S) = 2.59 Å D(S-H) = 1.37 Å, 1.37 Å Ang(Zn-Au-S) =145.93º Ang(H-S-H) = 91.51º, molecule

Concerning the chemisorption of carbon dioxide (CO_2 molecule) on Fe catalyst, it is shown to occur without dissociation of molecule. Fe atom has 6 electrons in its outer d-shell. It seems that the 2 electrons in the outer s-shell and the 4 unpaired

electrons in that d-shell give the ability to the Fe atom to have high coordination. Without the CO_2 molecule, Fe atom relaxes as an ad-atom on the hollow site by making 5 bonds with Zn and O-atoms. When the CO_2 is on the Fe atom, the hybridization changes but the coordination is maintained the same. Fe atom makes five covalent bonds (3 bonds with the surface; 2 among which with O-atoms and 1 with Zn-atom) and two bonds with the CO_2 molecule (1 bond with C-atom and 1 bond with O-atom like a shoulder) to maximize the charge transfer and binding energy, as will be discussed later below. It seems that both C and O-atoms possess high electronegativity properties (χ^C = 2.55 Pauling and χ^O = 3.44 Pauling) to compete for making covalent bonds with the Fe ad-atom. Moreover, the bond angle O-C-O of the molecule is reduced from 180° when it was a free molecule to 139° when it binds to Fe atom as consequence of changing hybridization at level of molecule and breaking its π-bonds in paving the way to make new bonds with Fe and allowing more charge exchange (overlap of orbitals). Besides the C-O bonds become pure σ-like and more elongated. The new C-O bond lengths are 1.30 Å and 1.21 Å being larger than the double bond C=O in the free CO_2 molecule (which is about 1.16 Å).

Regarding the chemisorption of hydrogen sulfide (H_2S), it is shown not to be associated with any dissociation on both Ag and Au, similar to the previous case of CO_2 on Fe. Without H_2S molecule, both Ag and Au atoms seem to have limited coordination as their outer d-shells are basically composed of nine electrons d^9, but with a bit discrepancy in electronegativity. For instance, Ag atom relaxes on the hollow site by making 2 bonds with underneath Zn-atoms, whereas Au atom relaxes on the center of the hollow site by making 3 bonds with underneath Zn-atoms. Moreover, when the H_2S molecule gets adsorbed on Ag, the coordination of Ag is maintained the same (i.e., to be 2) but its hybridization changes to make just two new bonds (1 bond

with underneath Zn-atom and 1 bond with S atom of molecule). In a similar way, when H_2S gets adsorbed on Au, the coordination of Au is also preserved the same (i.e., to be 3) with a change in hybridization geometry to keep two bonds with two underneath Zn-atoms and make a new bond with S atom of molecule. Notably, the bond angle H-S-H reduces a little bit from 92.1^o (when it was free molecule) to 91.5^o when the molecule binds to either Ag or Au atoms. The new bonds in the molecule are a bit elongated to become 1.37 Å larger than the value in free H_2S molecule (which is about 1.33 Å), revealing the occurrence of charge transfer.

From point of view of energetics, Table 6 displays the total energies and binding energies of TM catalysts. The largest binding energy is shown to correspond to Fe that might be due to its low electronegativity (i.e., high electro-positivity, if one may say) and its electronic shell structure, which makes Fe chemically most active. The existing 4 unpaired electrons in the d-shell ($3d^6$) are basically giving the ability to Fe atom to have up to a coordination of 6 (i.e., 6 bonds with the neighboring atoms).

Table 7 shows the adsorption energies of various gas molecules on the studied five catalysts. The shaded regions, in orange, in Table 7 correspond to physisorption cases and the other ones correspond to the chemisorption cases. As expected, in case of physisorption, the magnitude of the binding energy should be much less than 0.5 eV (i.e., $|E_{bind}| \ll 0.5$ eV). The results are benchmarked with the available ones in literature [67-92]. One should emphasize that some discrepancies may appear as the literature values correspond to either experimental or computational estimations and are due to the interactions of molecules with either film surfaces or clusters; whereas in our present case E_{bind} is due to interaction of molecule with a single ad-atom on the surface of ZnO-NR. In chemisorption cases, Table 7 shows two trends: (i) Pd and Pt

have chemisorption energies being close among all the studied gas molecules with bit higher values toward Pt. This might reveal that Pt is a bit more chemically active than Pd. The values of $|E_{bind}|$ being about same order of magnitudes versus gases in each one of them may also reveal the lack of selectivity (to be discussed below); (ii) Oxygen has high adsorption energies with all catalysts may also reveal that oxidation to the catalysts is very active at RT.

Table 6 : Total Energies of studied systems and binding energies of catalysts.

System	Total Energy (eV)	E_{bind} of Catalyst (eV)	Electronegativity of Catalyst: χ (Pauling)[†]	Atomic Radius of Catalyst (Å)	Electronic Configuration of Catalyst
ZnO-NR	-295033.933	N/A	N/A	N/A	N/A
ZnO-NR:Pt	-298584.078	-2.288	2.2	1.830	[Xe] $4f^{14} 5d^9 6s^1$
ZnO-NR:Pd	-298717.747	-1.207	2.2	1.790	[Kr] $4d^{10}$
ZnO-NR:Fe	-298475.982	-3.855	1.8	1.720	[Ar] $3d^6 4s^2$
ZnO-NR:Ag	-299250.178	-0.228	1.9	1.750	[Kr] $4d^{10} 5s^1$
ZnO-NR:Au	-299064.355	-1.649	2.4	1.790	[Xe] $4f^{14} 5d^{10} 6s^1$

[†] References [67, 68].

Table 7 : Binding energies of molecules on catalysts for the five studied ZnO-NR devices.

	Catalysts				
	Pt	**Pd**	**Fe**	**Ag**	**Au**
H_2	-2.080[¶] eV -2.232[a] eV	-1.094[¶] eV -0.936[b] eV	0.027[¶] eV 0.050[c] eV	-0.152[¶] eV -0.180[d] eV	-0.066[¶] eV -0.090[e] eV
H_2S	-2.457[¶] eV -2.62[f] eV	-1.733[¶] eV -1.55[g] eV	-0.107[¶] eV -0.50[h] eV	-1.042 eV -1.426[i] eV	-0.788[¶] eV -0.90[j] eV
CO_2	-1.705[¶] eV -1.73[k] eV	-1.465[¶] eV -1.606[l] eV	-0.931[¶] eV -0.72[m],-1.25[m] eV	-0.102[¶] eV -0.25[n] eV	-0.202[¶] eV -0.26[o] eV
O_2	-2.824[¶] eV -2.46[p] eV -2.63[q] eV	-2.646[¶] eV -2.21[r] eV	-3.520[¶] eV -3.67[s] eV	-1.503[¶] eV -1.31[t],-1.81[t] eV	-1.827[¶] eV -1.99[u] eV
N_2	-1.524[¶] eV -1.221[v] eV	-1.392[¶] eV -1.397[w] eV	-0.059[¶] eV -0.165[x] eV	-0.453[¶] eV -0.5[y],-0.6[y] eV	-0.138[¶] eV -0.13[z] eV

[¶]Present work, [a][69],[b][70],[c][71],[d][72],[e][73],[f][74],[g][75],[h][76],[i][77],[j][78],[k][79],[l][80], [m][81],[n][82], [o][83], [p][84][q][85],[r][86],[s][87],[t][88],[u][89],[v][90],[w][91],[x][92],[y][93],[z][94]

(a)
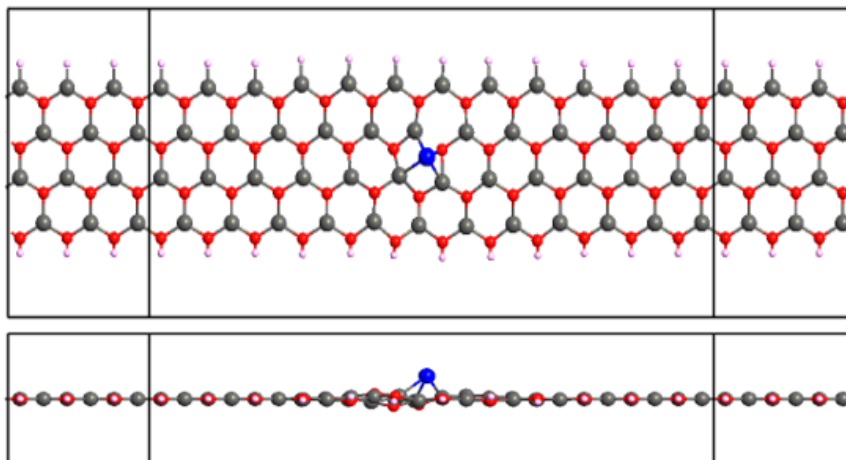
(b)
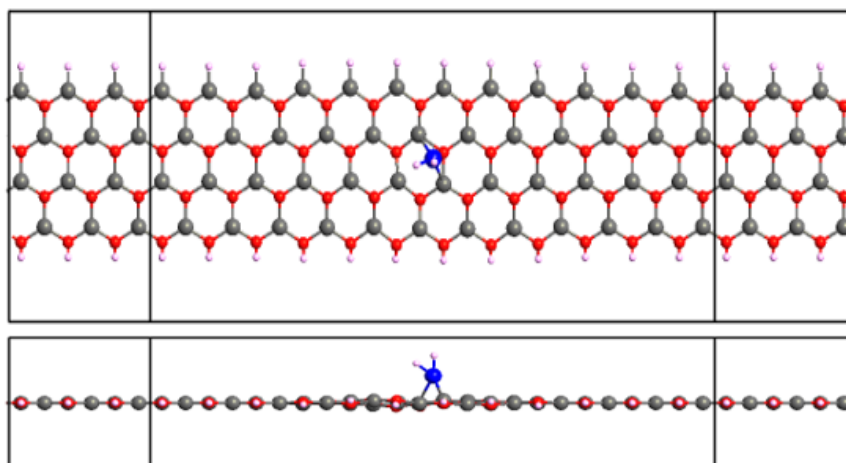
Figure 4.1 : Relaxed Structures of catalysts on ZnO-NR devices
(a) Pt catalyst on ZnO-NR (b) H_2 gas molecules on Pt on ZnO-NR (c) Pd catalyst on ZnO-NR (d) H_2 gas molecules on Pd on ZnO-NR (e) Fe catalyst on ZnO-NR (f) CO_2 gas molecules on Fe on ZnO-NR (g) Ag catalyst on ZnO-NR (h) H_2S gas molecules on Ag on ZnO-NR (i) Au catalyst on ZnO-NR (j) H_2S gas molecules on Au on ZnO-NR.
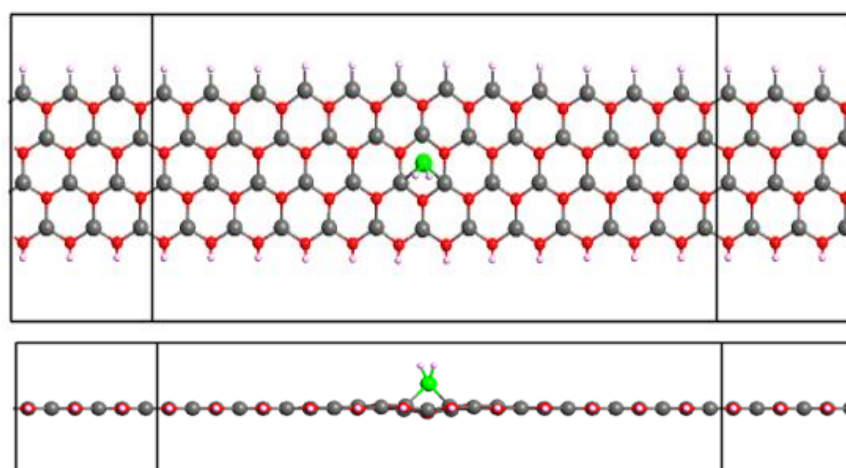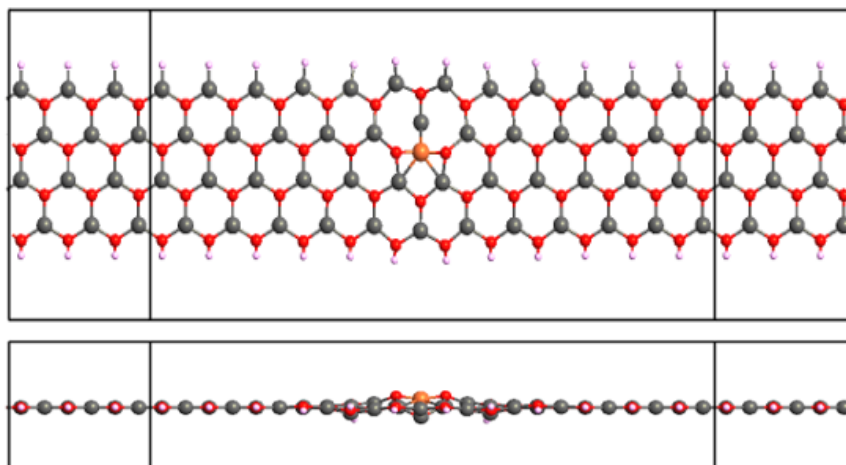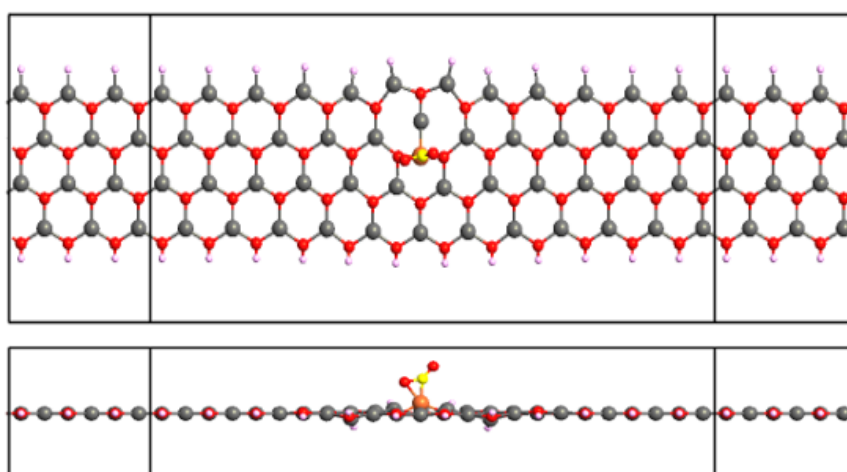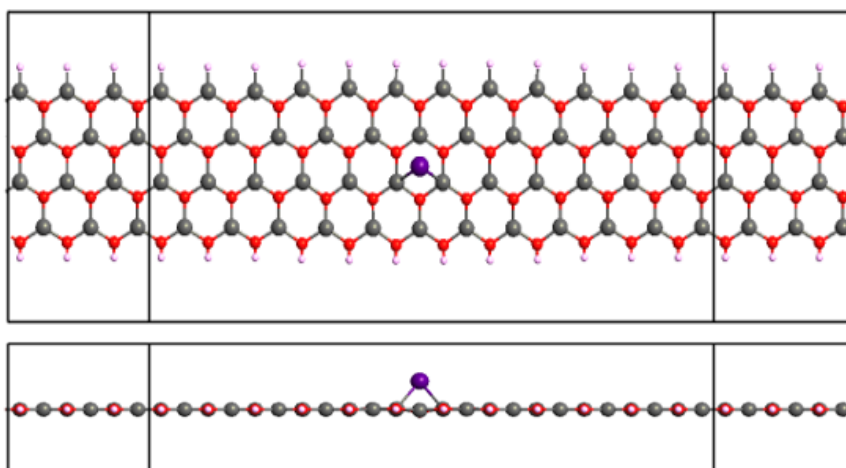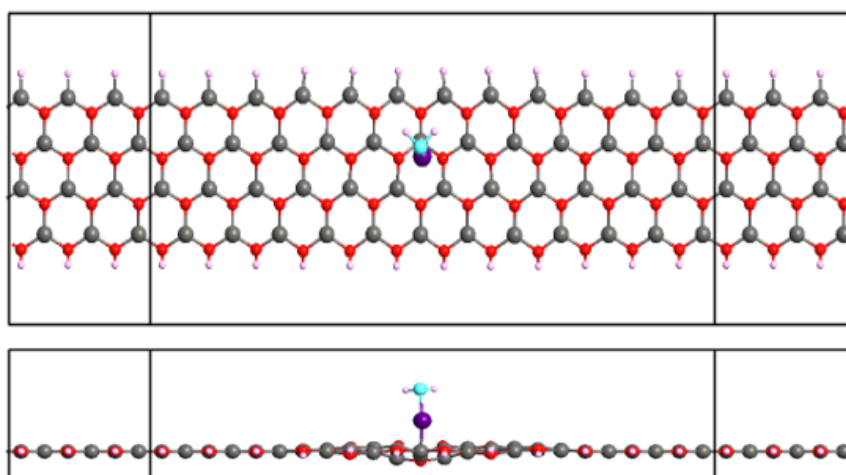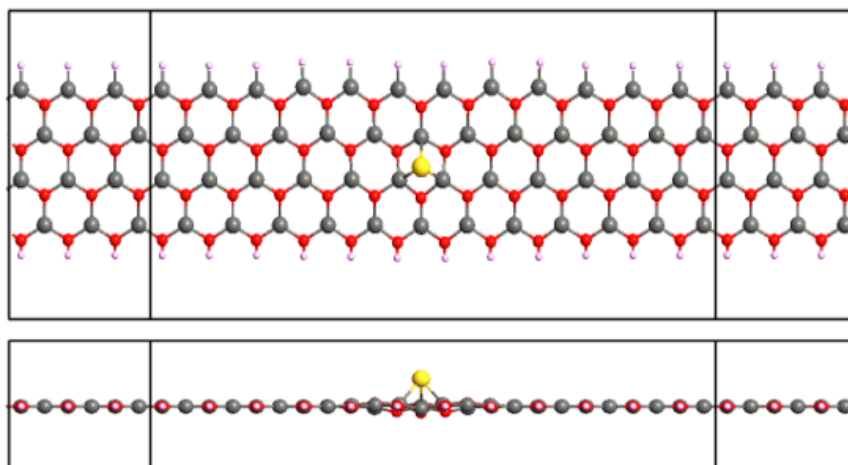
(c)
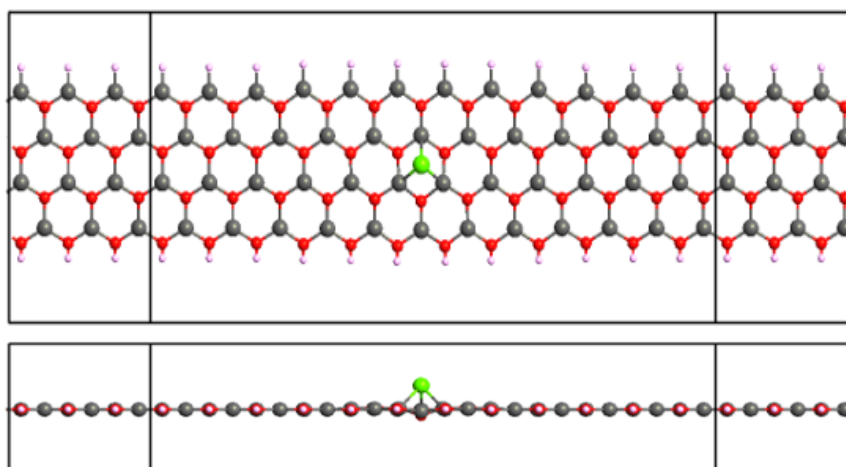
(d)

Figure 4.1 : Relaxed Structures of catalysts on ZnO-NR devices (continued) (a) Pt catalyst on ZnO-NR (b) H_2 gas molecules on Pt on ZnO-NR (c) Pd catalyst on ZnO-NR (d) H_2 gas molecules on Pd on ZnO-NR (e) Fe catalyst on ZnO-NR (f) CO_2 gas molecules on Fe on ZnO-NR (g) Ag catalyst on ZnO-NR (h) H_2S gas molecules on Ag on ZnO-NR (i) Au catalyst on ZnO-NR (j) H_2S gas molecules on Au on ZnO-NR.
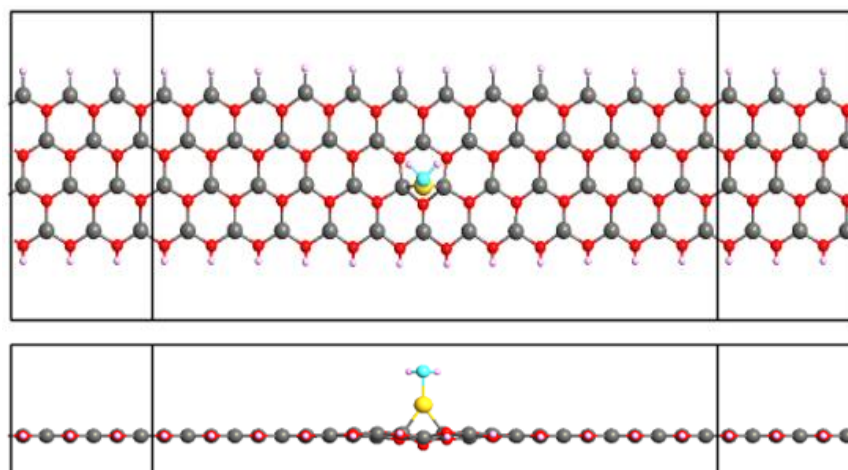
(e)

(f)

Figure 4.1 : Relaxed Structures of catalysts on ZnO-NR devices (continued)
(a) Pt catalyst on ZnO-NR (b) H_2 gas molecules on Pt on ZnO-NR (c) Pd catalyst on
ZnO-NR (d) H_2 gas molecules on Pd on ZnO-NR (e) Fe catalyst on ZnO-NR (f) CO_2
gas molecules on Fe on ZnO-NR (g) Ag catalyst on ZnO-NR (h) H_2S gas molecules
on Ag on ZnO-NR (i) Au catalyst on ZnO-NR (j) H_2S gas molecules on Au on ZnO-
NR.

(g)

(h)

Figure 4.1 : Relaxed Structures of catalysts on ZnO-NR devices (continued)
(a) Pt catalyst on ZnO-NR (b) H_2 gas molecules on Pt on ZnO-NR (c) Pd catalyst on ZnO-NR (d) H_2 gas molecules on Pd on ZnO-NR (e) Fe catalyst on ZnO-NR (f) CO_2 gas molecules on Fe on ZnO-NR (g) Ag catalyst on ZnO-NR (h) H_2S gas molecules on Ag on ZnO-NR (i) Au catalyst on ZnO-NR (j) H_2S gas molecules on Au on ZnO-NR.

(i)

(j)

Figure 4.1 : Relaxed Structures of catalysts on ZnO-NR devices (continued)
(a) Pt catalyst on ZnO-NR (b) H_2 gas molecules on Pt on ZnO-NR (c) Pd catalyst on
ZnO-NR (d) H_2 gas molecules on Pd on ZnO-NR (e) Fe catalyst on ZnO-NR (f) CO_2
gas molecules on Fe on ZnO-NR (g) Ag catalyst on ZnO-NR (h) H_2S gas molecules
on Ag on ZnO-NR (i) Au catalyst on ZnO-NR (j) H_2S gas molecules on Au on ZnO-
NR.

4.3 Band Structures

Figure 4.2 displays the band structures of the periodic supercell calculations, corresponding to 5 catalysts (Pt, Pd, Fe, Ag, and Au) before and after the chemisorption of molecules. Initially, within the scheme of our DFT calculation, pristine ZnO-NR possesses a bandgap energy $E_g = 0.440$ eV. It is noticeable that this later bandgap value does not deviate much in case of deposition of Pt or Pd catalysts on ZnO-NR either before or after the chemisorption of H_2 molecule. Conversely, in case of Fe catalyst, the gap almost closes (i.e., reaching a minimum value of $E_g = 0.092$ eV). The closure of the gap might be justified by the strong interaction/bonding of Fe with 3 underneath Zn-atoms beside the size of Bohr radius, $a_B \sim 23.4$ Å [95], which is large enough as compared to length of sample C = 40.75 Å, so electronic hoping to the mirror symmetric images of the catalyst might be possible. Nevertheless, the chemisorption of Fe catalyst to CO_2 molecule reduces the bonding to the ZnO-NR surface and reopen the gap to become $E_g = 0.233$ eV. In the case of Ag and Au catalysts, the bandgap gets reduced with realizations of many flat bands near Fermi level that might be attributed to the effect of localized paired d-states. Moreover, that many flat conduction bands should hamper the passage of electric current (see the IV characteristics below). The chemisorption of H_2S molecule on either Ag or Au causes their reduction in the bonding to ZnO-NR surface and changes a bit the bandgap and confinement behaviors. More conduction bands in case of H_2S/Ag become dispersive revealing the delocalization of states above Fermi level, starting from LUMO, as will be discussed in next sub-section.
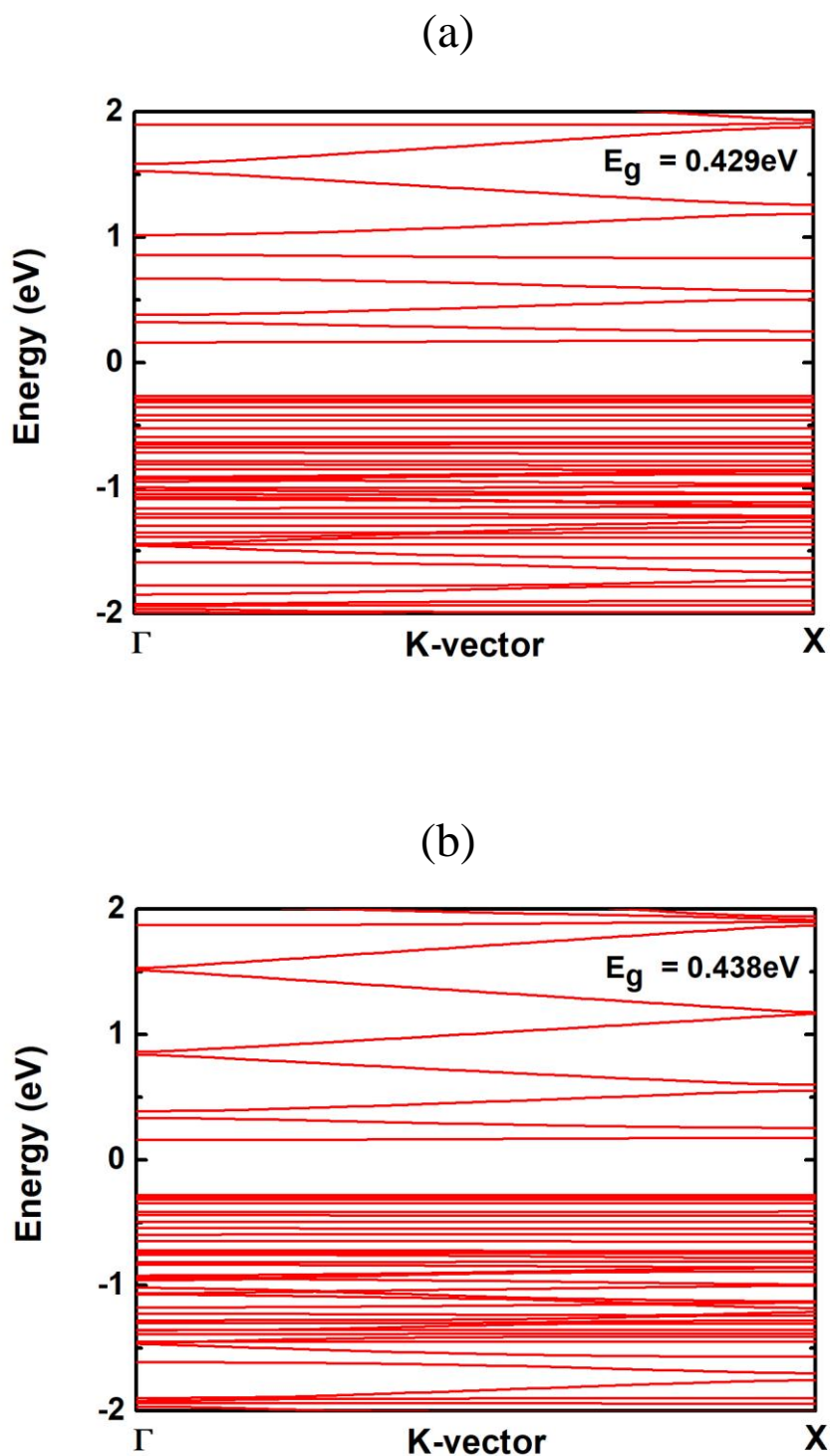
(a)

(b)

Figure 4.2 : Band Structure of catalysts on ZnO-NR devices
(a) Pt on ZnO-NR (b) H_2 on Pt on ZnO-NR (c) Pd on ZnO-NR (d) H_2 on Pd on ZnO-NR (e) Fe on ZnO-NR (f) CO_2 on Fe on ZnO-NR (g) Ag on ZnO-NR (h) H_2S on Ag on ZnO-NR (i) Au on ZnO-NR (j) H_2S on Au on ZnO-NR.
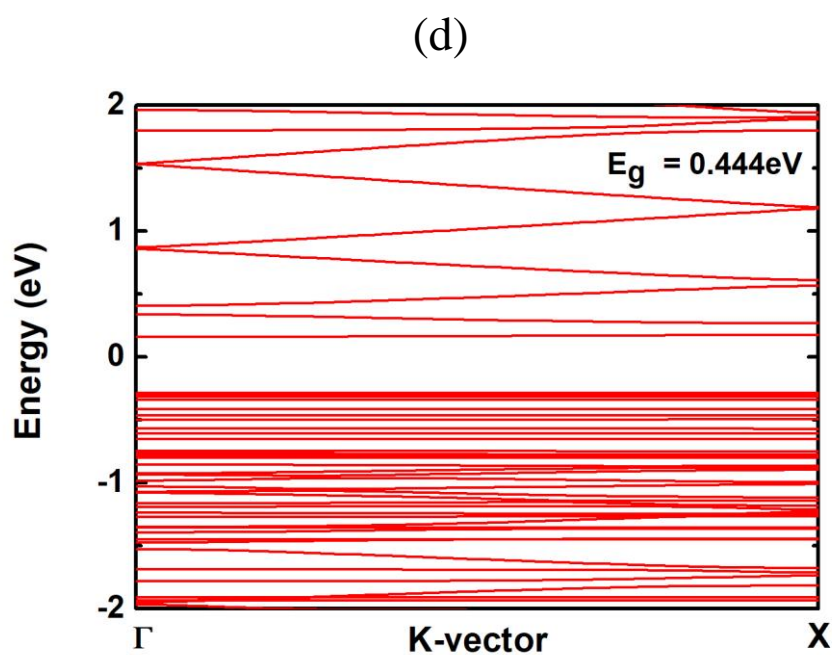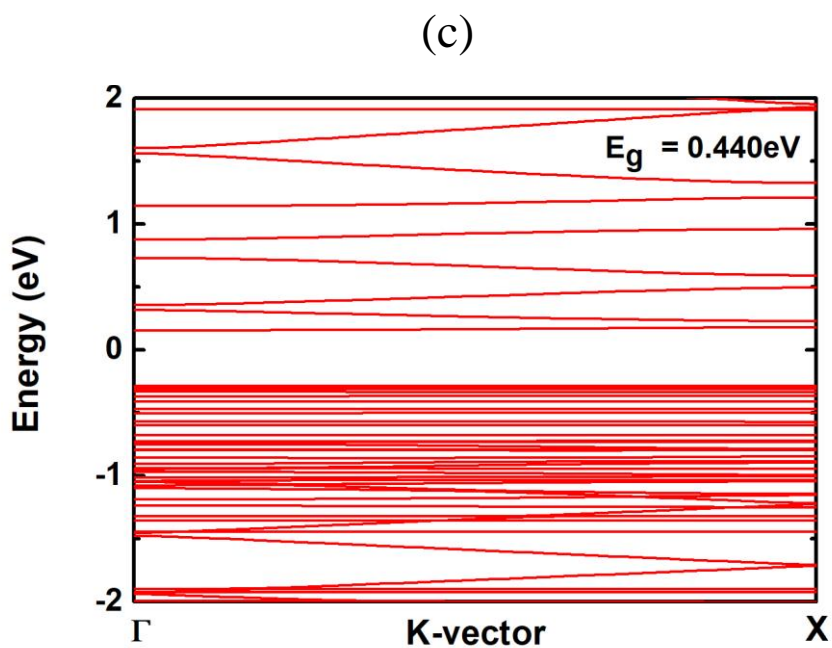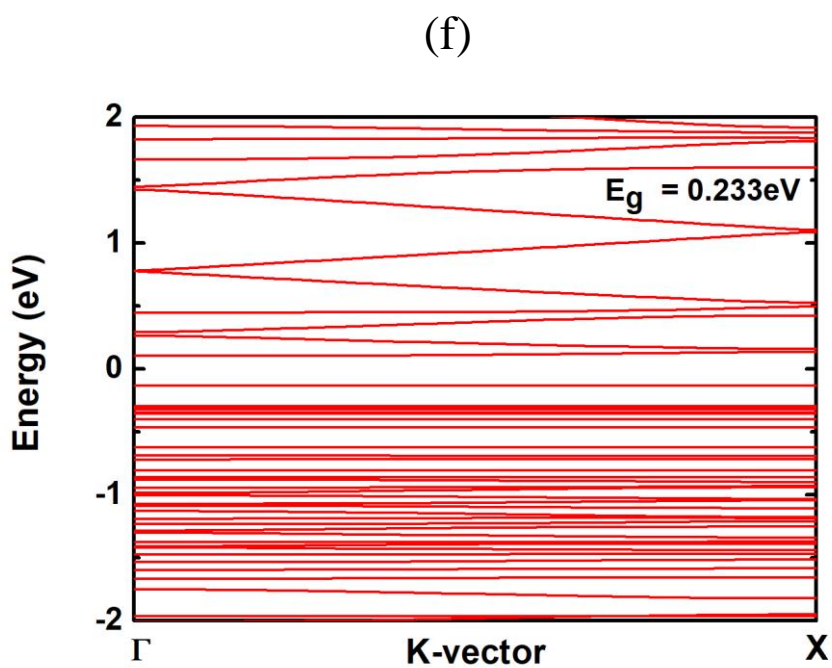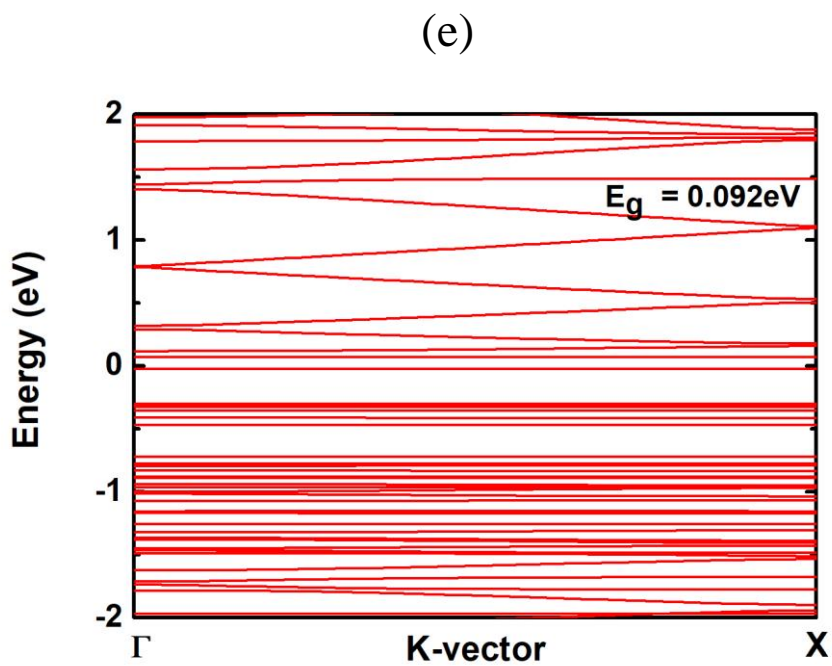
(c)

(d)

Figure 4.2 : Band Structure of catalysts on ZnO-NR devices (continued)
(a) Pt on ZnO-NR (b) H_2 on Pt on ZnO-NR (c) Pd on ZnO-NR (d) H_2 on Pd on ZnO-NR (e) Fe on ZnO-NR (f) CO_2 on Fe on ZnO-NR (g) Ag on ZnO-NR (h) H_2S on Ag on ZnO-NR (i) Au on ZnO-NR (j) H_2S on Au on ZnO-NR.
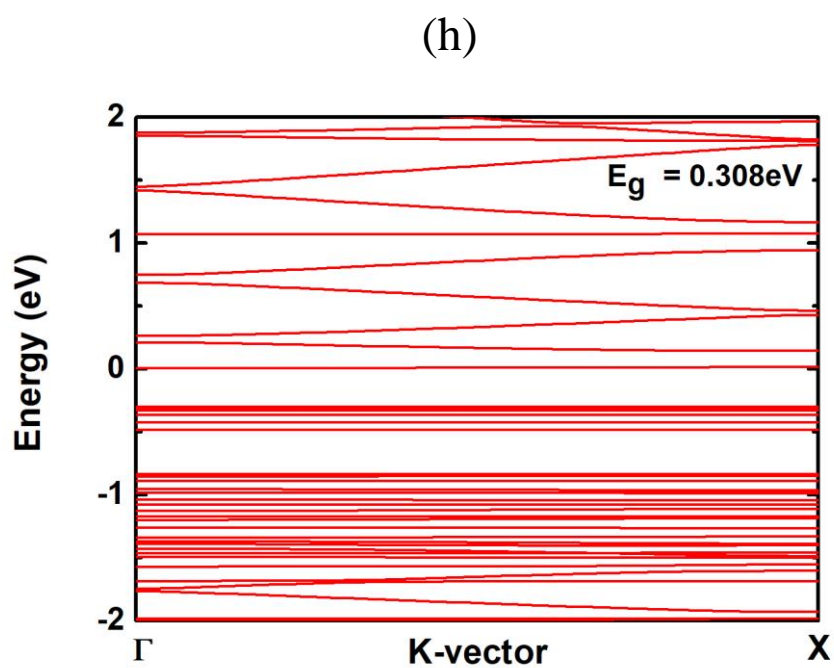
(e)

(f)

Figure 4.2 : Band Structure of catalysts on ZnO-NR devices (continued)
(a) Pt on ZnO-NR (b) H_2 on Pt on ZnO-NR (c) Pd on ZnO-NR (d) H_2 on Pd on ZnO-NR (e) Fe on ZnO-NR (f) CO_2 on Fe on ZnO-NR (g) Ag on ZnO-NR (h) H_2S on Ag on ZnO-NR (i) Au on ZnO-NR (j) H_2S on Au on ZnO-NR.
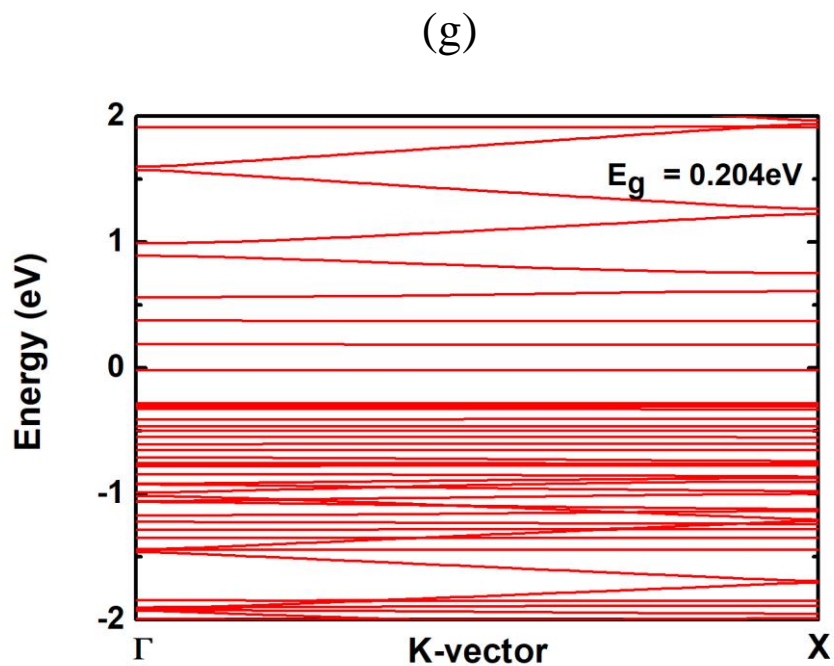
(g)

(h)

Figure 4.2 : Band Structure of catalysts on ZnO-NR devices (continued)
(a) Pt on ZnO-NR (b) H_2 on Pt on ZnO-NR (c) Pd on ZnO-NR (d) H_2 on Pd on ZnO-NR (e) Fe on ZnO-NR (f) CO_2 on Fe on ZnO-NR (g) Ag on ZnO-NR (h) H_2S on Ag on ZnO-NR (i) Au on ZnO-NR (j) H_2S on Au on ZnO-NR.
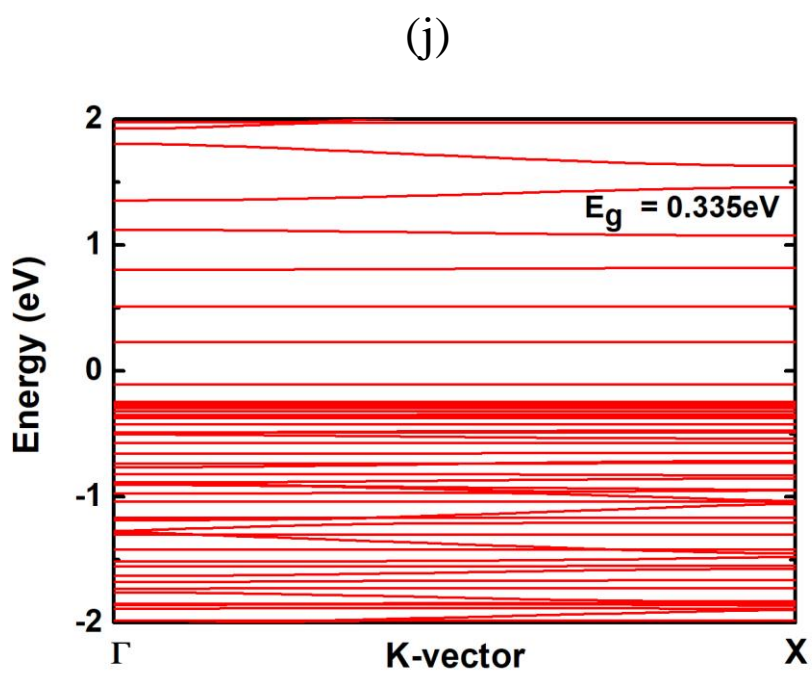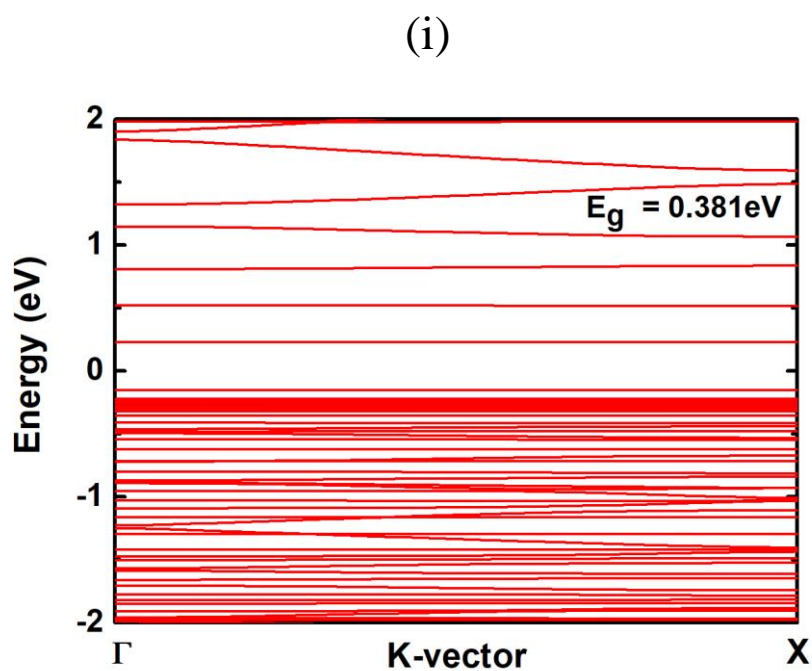
(i)

(j)

Figure 4.2 : Band Structure of catalysts on ZnO-NR devices (continued)
(a) Pt on ZnO-NR (b) H_2 on Pt on ZnO-NR (c) Pd on ZnO-NR (d) H_2 on Pd on ZnO-NR (e) Fe on ZnO-NR (f) CO_2 on Fe on ZnO-NR (g) Ag on ZnO-NR (h) H_2S on Ag on ZnO-NR (i) Au on ZnO-NR (j) H_2S on Au on ZnO-NR.

4.4 Charge Distribution

One way to assess the factors affecting the transport properties is to inspect the charge distributions of the highest occupied molecular orbital (HOMO) and the lowest unoccupied molecular orbitals (LUMO) states. They would give information about both the bonding and the charge localization/confinement characters. Figures 4.3 and Figures 4.4 display the charge distributions of HOMO/LUMO states before and after the occurrence of chemisorption with the molecule in concern, respectively.

Considering the chemisorption of H_2 molecule of either Pt or Pd catalyst, before the arrival of this molecule, the HOMO state shows some localization of hole as likely being induced by the asymmetry of the ZnO-NR, because the upper edge is composed of Zn-atoms (i.e., Zn-rich edge) while the lower edge is composed of O-atoms (i.e., O-rich edge). The location of the catalyst makes likely one side of the nanoribbon lower in potential than the other side. Consequently, one side more than the other would embrace the HOMO state. On the other hand, the LUMO state, before the arrival of the H_2 molecule, is kind of extended state with a bit localization near the catalyst in case of Pt. In case of Pd, the LUMO has more components on the edges revealing the existence of dispersive bands or conductive channels on the edges. After the arrival of H_2 molecule and occurrence of its chemisorption on the catalysts, it seems that that will cause a mimic effect on the HOMO state but a bit larger effect on the LUMO state. It seems that the chemisorption of H_2 molecule with its dissociation is playing the role of reducing the surface by giving more charge to it. Thus, this effect would enhance the conductivity (i.e., IV curve, as will be discussed below). In brief, the H_2 molecule is introducing donor states and enhancing the electronic transport.

Regarding the chemisorption of CO_2 on Fe catalyst, both HOMO and LUMO states, before the arrival of molecule, are shown to be strongly localized near the locality of Fe catalyst. However, after the occurrence of chemisorption of CO_2 on Fe catalyst, the HOMO state remains localized near the catalyst while the LUMO becomes extended. It is clear that such a deviation of LUMO state in confinement character from before to after the landing of CO_2 molecule would have effect on the transport properties (i.e., on IV curve, see below).

Concerning the chemisorption of H_2S on either Ag or Au catalysts, one would notice that before the arrival of H_2S molecule, both HOMO and LUMO states to be localized; one near the catalyst and the second one to the left-side of it, respectively. After the arrival of H_2S and the occurrence of its chemisorption on catalyst, huge changes in confinement characters of HOMO and LUMO states occur. In case of H_2S/Ag, the HOMO state changes its localization to be confined to the right side of the catalyst; whereas, the LUMO state becomes more extended revealing that it originates from a dispersive band (i.e., conductive channel supported more by the Zn-edge atoms). Definitely, such drastic changes in confinement character of especially the electron would enhance the transport properties of the whole device. On the other hand, in the case of H_2S/Au, both HOMO and LUMO states remain confined near the catalyst site. Such confinement characters would hamper the transport properties. These discussed confinement behaviors would manifest themselves in the IV characteristics, as will be discussed below. Nevertheless, the deviation in confinement characters of the wave-function from before to after the occurrence of chemisorption would affect both the IV curves and the sensor response, as will be discussed below.
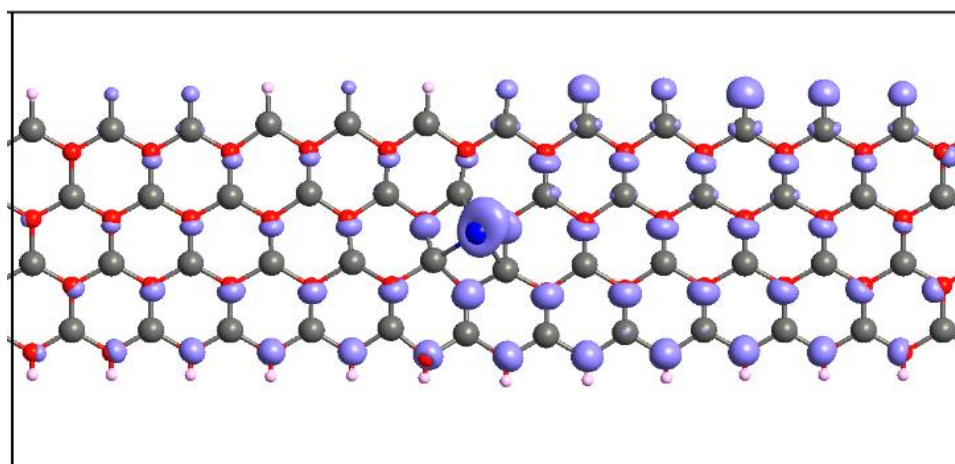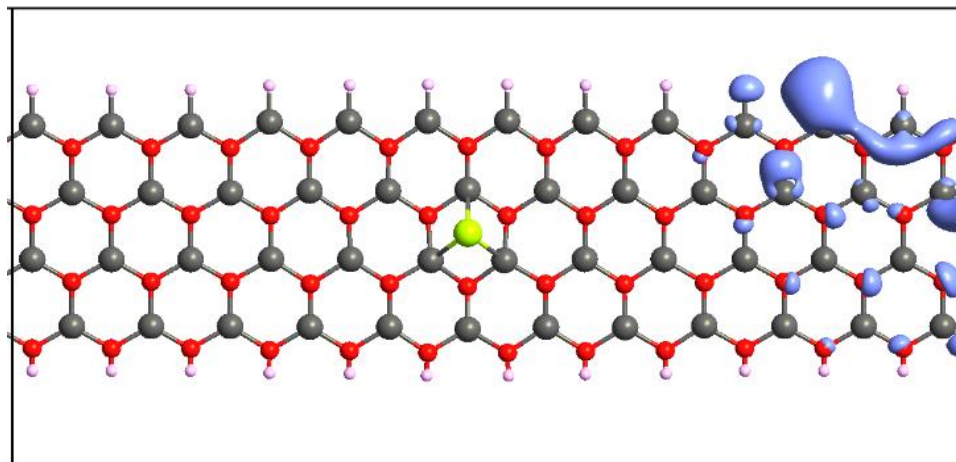
(a)
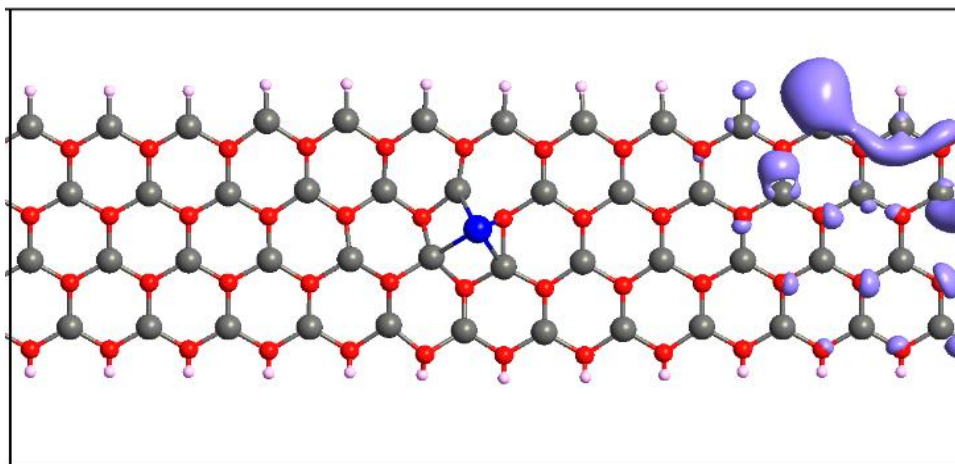
(b)

Figure 4.3 : HOMO and LUMO eigen-states of catalysts on ZnO-NR devices
(a) Pt on ZnO-NR device HOMO eigen-states (b) Pt on ZnO-NR device LUMO
eigen-states (c) Pd on ZnO-NR device HOMO eigen-states (d) Pd on ZnO-NR device
LUMO eigen-states (e) Fe on ZnO-NR device HOMO eigen-states (f) Fe on ZnO-NR
device LUMO eigen-states (g) Ag on ZnO-NR device HOMO eigen-states (h) Ag on
ZnO-NR device LUMO eigen-states (i) Au on ZnO-NR device HOMO eigen-states
(j) Au on ZnO-NR device LUMO eigen-states.

(c)

(d)

Figure 4.3 : HOMO and LUMO eigen-states of catalysts on ZnO-NR devices
(continued)
(a) Pt on ZnO-NR device HOMO eigen-states (b) Pt on ZnO-NR device LUMO
eigen-states (c) Pd on ZnO-NR device HOMO eigen-states (d) Pd on ZnO-NR device
LUMO eigen-states (e) Fe on ZnO-NR device HOMO eigen-states (f) Fe on ZnO-NR
device LUMO eigen-states (g) Ag on ZnO-NR device HOMO eigen-states (h) Ag on
ZnO-NR device LUMO eigen-states (i) Au on ZnO-NR device HOMO eigen-states
(j) Au on ZnO-NR device LUMO eigen-states.
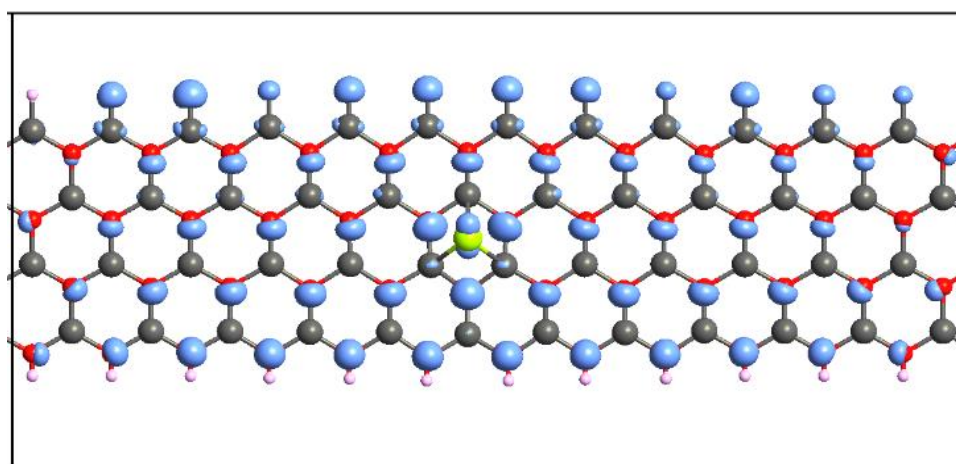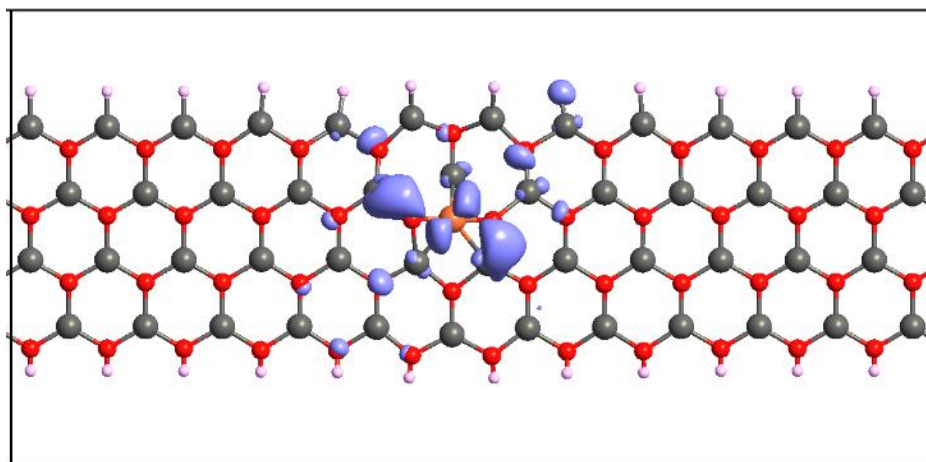
(e)

(f)

Figure 4.3 : HOMO and LUMO eigen-states of catalysts on ZnO-NR devices (continued)

(a) Pt on ZnO-NR device HOMO eigen-states (b) Pt on ZnO-NR device LUMO eigen-states (c) Pd on ZnO-NR device HOMO eigen-states (d) Pd on ZnO-NR device LUMO eigen-states (e) Fe on ZnO-NR device HOMO eigen-states (f) Fe on ZnO-NR device LUMO eigen-states (g) Ag on ZnO-NR device HOMO eigen-states (h) Ag on ZnO-NR device LUMO eigen-states (i) Au on ZnO-NR device HOMO eigen-states (j) Au on ZnO-NR device LUMO eigen-states.
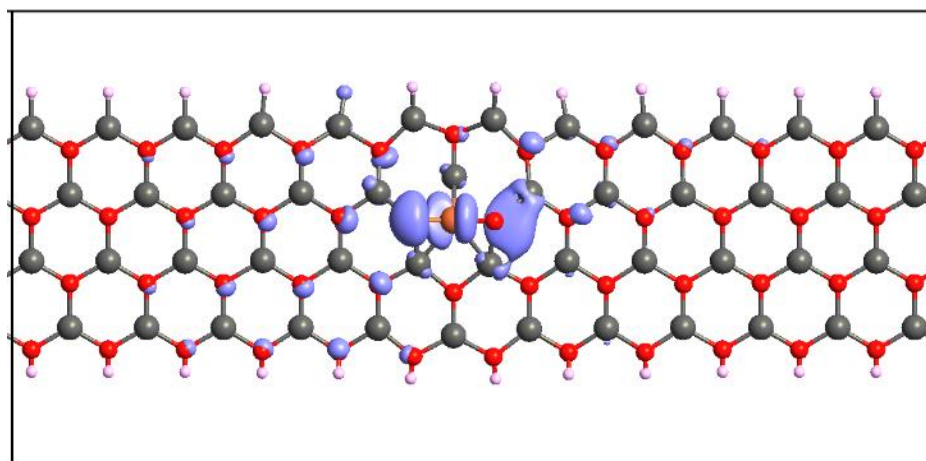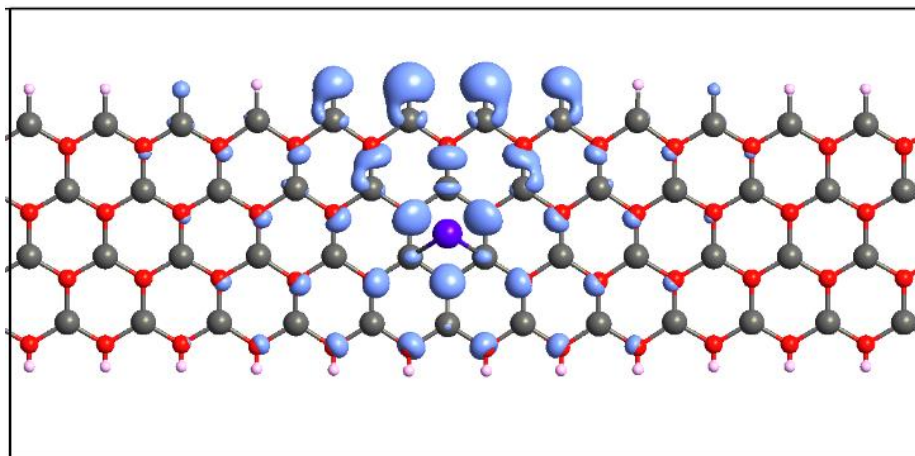
(g)

(h)

Figure 4.3 : HOMO and LUMO eigen-states of catalysts on ZnO-NR devices (continued)

(a) Pt on ZnO-NR device HOMO eigen-states (b) Pt on ZnO-NR device LUMO eigen-states (c) Pd on ZnO-NR device HOMO eigen-states (d) Pd on ZnO-NR device LUMO eigen-states (e) Fe on ZnO-NR device HOMO eigen-states (f) Fe on ZnO-NR device LUMO eigen-states (g) Ag on ZnO-NR device HOMO eigen-states (h) Ag on ZnO-NR device LUMO eigen-states (i) Au on ZnO-NR device HOMO eigen-states (j) Au on ZnO-NR device LUMO eigen-states.
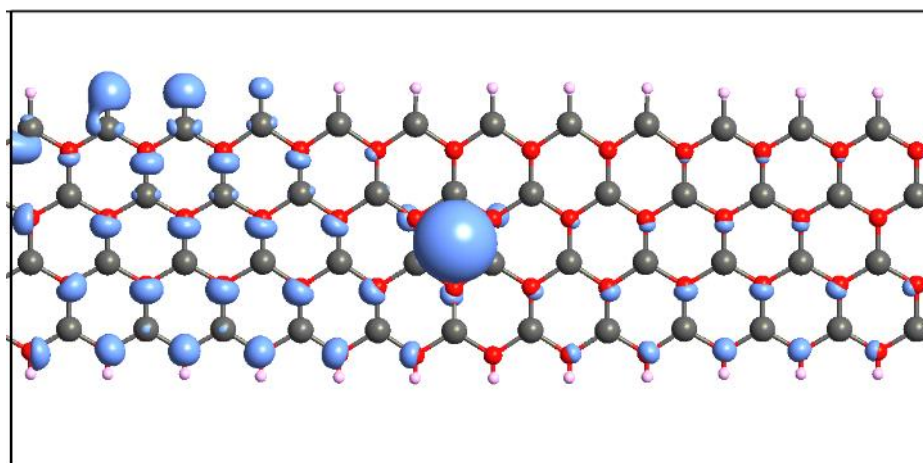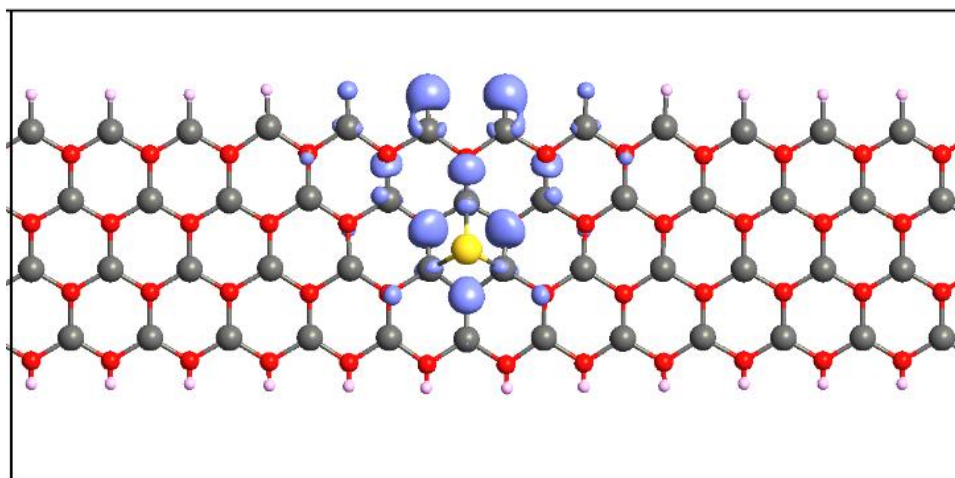
(i)

(j)

Figure 4.3 : HOMO and LUMO eigen-states of catalysts on ZnO-NR devices
(continued)

(a) Pt on ZnO-NR device HOMO eigen-states (b) Pt on ZnO-NR device LUMO eigen-states (c) Pd on ZnO-NR device HOMO eigen-states (d) Pd on ZnO-NR device LUMO eigen-states (e) Fe on ZnO-NR device HOMO eigen-states (f) Fe on ZnO-NR device LUMO eigen-states (g) Ag on ZnO-NR device HOMO eigen-states (h) Ag on ZnO-NR device LUMO eigen-states (i) Au on ZnO-NR device HOMO eigen-states (j) Au on ZnO-NR device LUMO eigen-states.
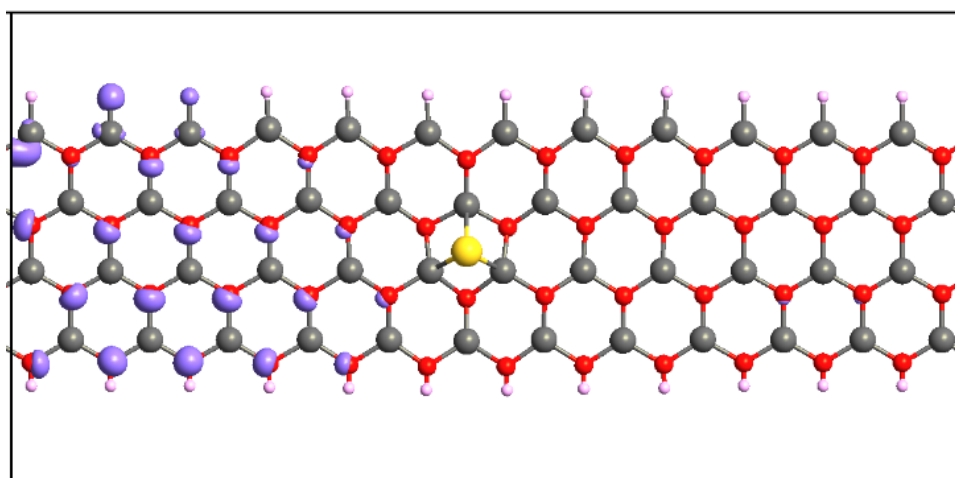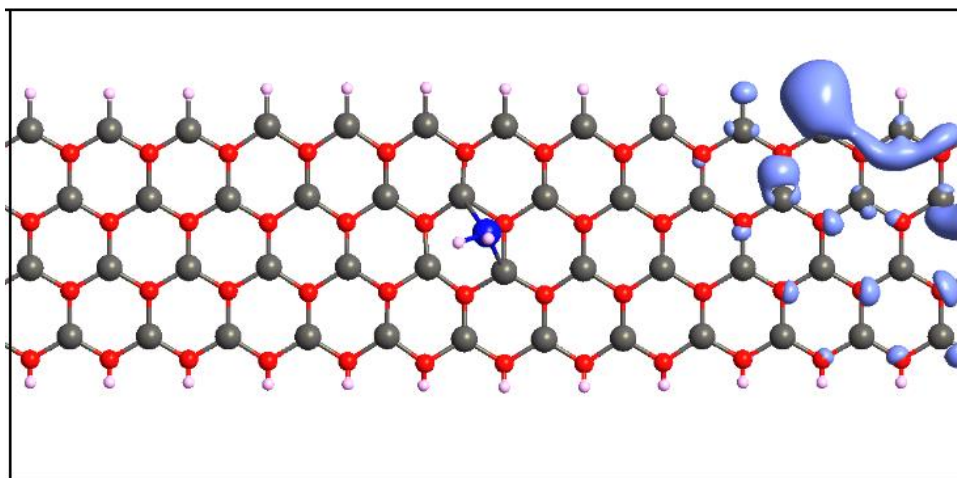
(a)

(b)

Figure 4.4 : HOMO and LUMO eigen-states of catalysts and gas molecule on ZnO-NR devices

(a) H_2 on Pt on ZnO-NR device HOMO eigen-states (b) H_2 on Pt on ZnO-NR device LUMO eigen-states (c) H_2 on Pd on ZnO-NR device HOMO eigen-states (d) H_2 on Pd on ZnO-NR device LUMO eigen-states (e) CO_2 on Fe on ZnO-NR device HOMO eigen-states (f) CO_2 on Fe on ZnO-NR device LUMO eigen-states (g) H_2S on Ag on ZnO-NR device HOMO eigen-states (h) H_2S on Ag on ZnO-NR device LUMO eigen-states (i) H_2S on Au on ZnO-NR device HOMO eigen-states (j) H_2S on Au on ZnO-NR device LUMO eigen-states.

(c)

(d)

Figure 4.4 : HOMO and LUMO eigen-states of catalysts and gas molecule on
ZnO-NR devices (continued)

(a) H_2 on Pt on ZnO-NR device HOMO eigen-states (b) H_2 on Pt on ZnO-NR device
LUMO eigen-states (c) H_2 on Pd on ZnO-NR device HOMO eigen-states (d) H_2 on
Pd on ZnO-NR device LUMO eigen-states (e) CO_2 on Fe on ZnO-NR device HOMO
eigen-states (f) CO_2 on Fe on ZnO-NR device LUMO eigen-states (g) H_2S on Ag on
ZnO-NR device HOMO eigen-states (h) H_2S on Ag on ZnO-NR device LUMO eigen-
states (i) H_2S on Au on ZnO-NR device HOMO eigen-states (j) H_2S on Au on ZnO-
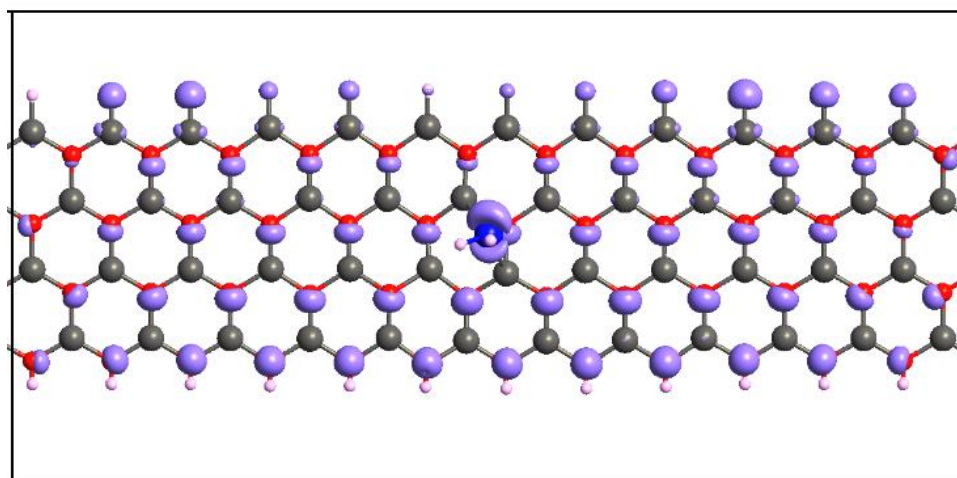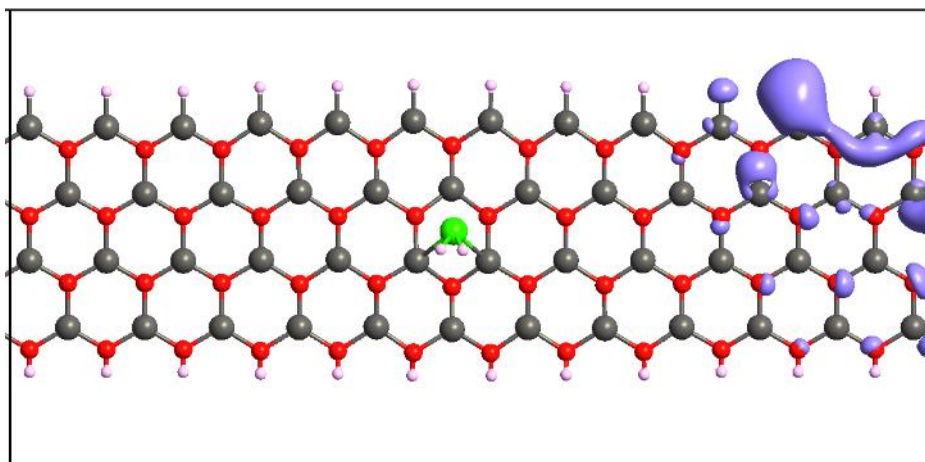NR device LUMO eigen-states.

(e)

(f)

Figure 4.4 : HOMO and LUMO eigen-states of catalysts and gas molecule on ZnO-NR devices (continued)

(a) H_2 on Pt on ZnO-NR device HOMO eigen-states (b) H_2 on Pt on ZnO-NR device LUMO eigen-states (c) H_2 on Pd on ZnO-NR device HOMO eigen-states (d) H_2 on Pd on ZnO-NR device LUMO eigen-states (e) CO_2 on Fe on ZnO-NR device HOMO eigen-states (f) CO_2 on Fe on ZnO-NR device LUMO eigen-states (g) H_2S on Ag on ZnO-NR device HOMO eigen-states (h) H_2S on Ag on ZnO-NR device LUMO eigen-states (i) H_2S on Au on ZnO-NR device HOMO eigen-states (j) H_2S on Au on ZnO-NR device LUMO eigen-states.
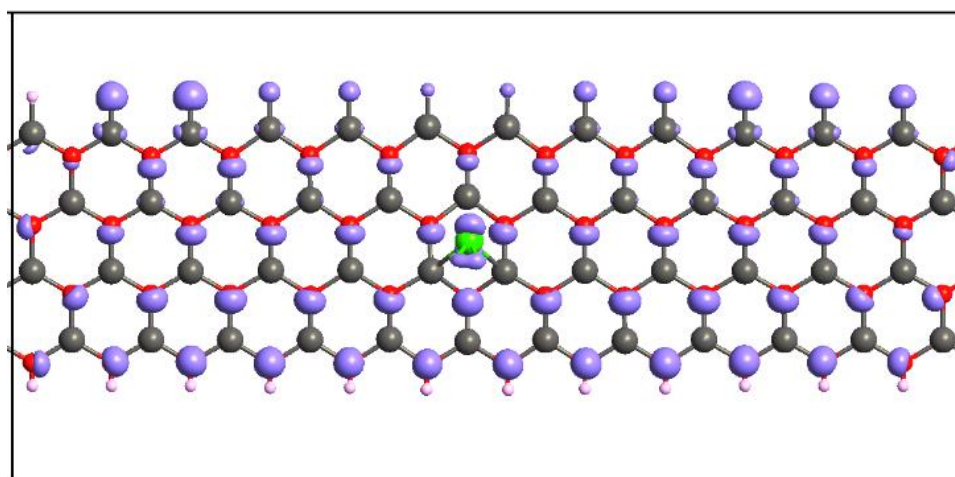
(g)

(h)

Figure 4.4 : HOMO and LUMO eigen-states of catalysts and gas molecule on ZnO-NR devices (continued)

(a) H_2 on Pt on ZnO-NR device HOMO eigen-states (b) H_2 on Pt on ZnO-NR device LUMO eigen-states (c) H_2 on Pd on ZnO-NR device HOMO eigen-states (d) H_2 on Pd on ZnO-NR device LUMO eigen-states (e) CO_2 on Fe on ZnO-NR device HOMO eigen-states (f) CO_2 on Fe on ZnO-NR device LUMO eigen-states (g) H_2S on Ag on ZnO-NR device HOMO eigen-states (h) H_2S on Ag on ZnO-NR device LUMO eigen-states (i) H_2S on Au on ZnO-NR device HOMO eigen-states (j) H_2S on Au on ZnO-NR device LUMO eigen-states.
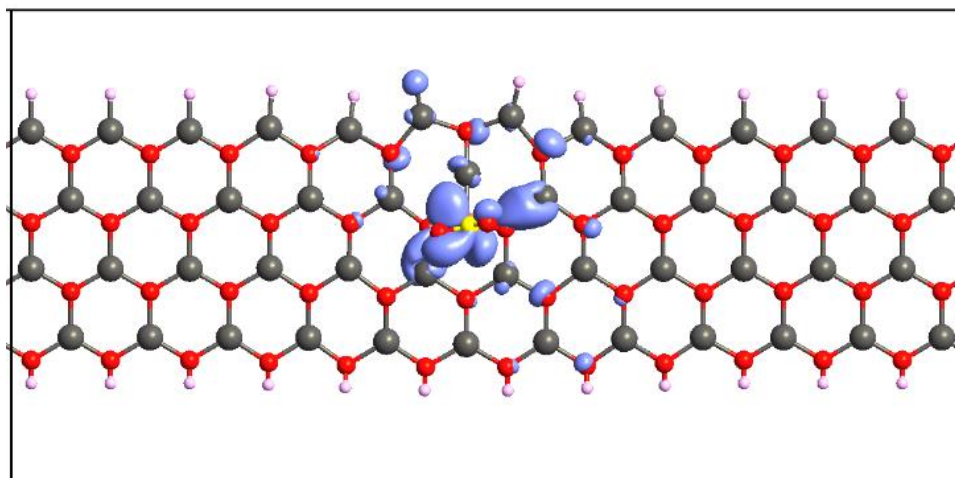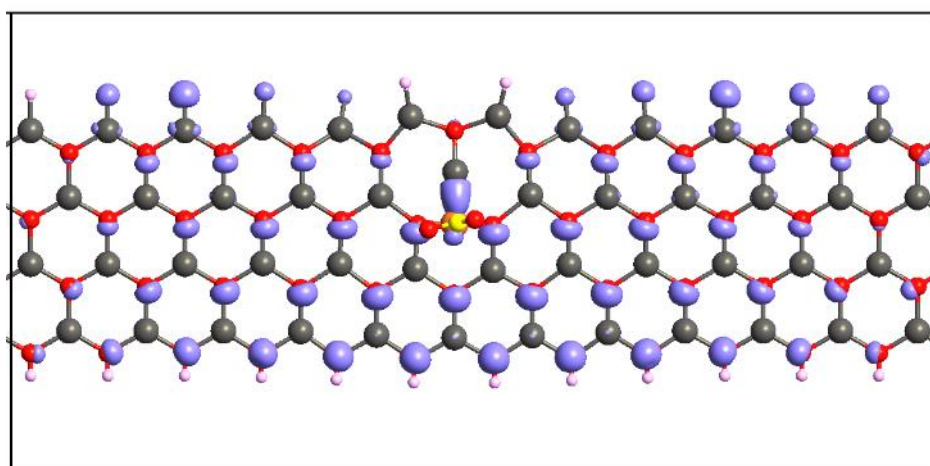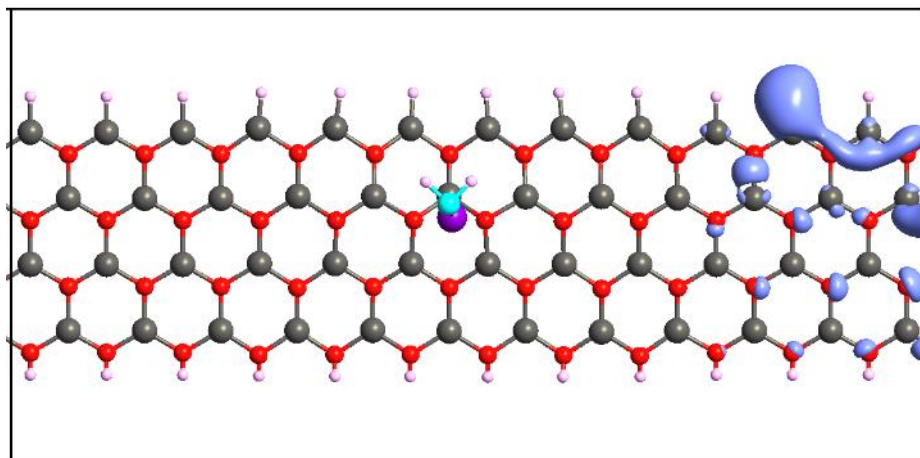
(i)

(j)

Figure 4.4 : HOMO and LUMO eigen-states of catalysts and gas molecule on ZnO-NR devices (continued)

(a) H_2 on Pt on ZnO-NR device HOMO eigen-states (b) H_2 on Pt on ZnO-NR device LUMO eigen-states (c) H_2 on Pd on ZnO-NR device HOMO eigen-states (d) H_2 on Pd on ZnO-NR device LUMO eigen-states (e) CO_2 on Fe on ZnO-NR device HOMO eigen-states (f) CO_2 on Fe on ZnO-NR device LUMO eigen-states (g) H_2S on Ag on ZnO-NR device HOMO eigen-states (h) H_2S on Ag on ZnO-NR device LUMO eigen-states (i) H_2S on Au on ZnO-NR device HOMO eigen-states (j) H_2S on Au on ZnO-NR device LUMO eigen-states.
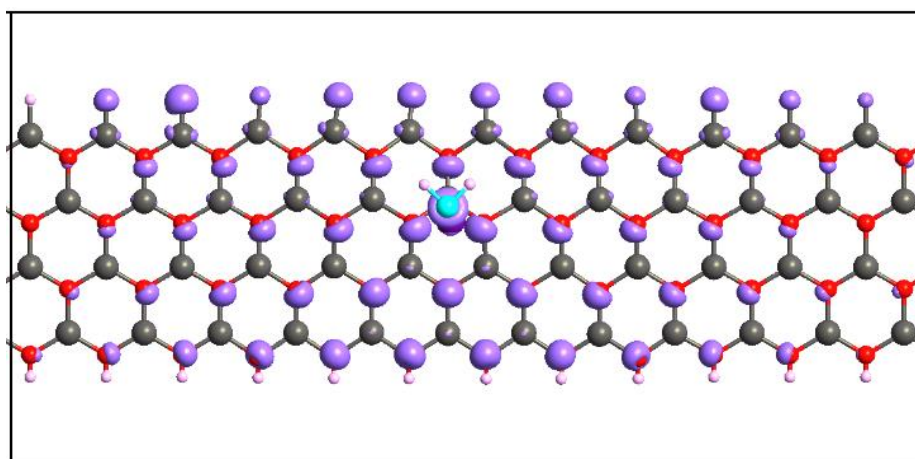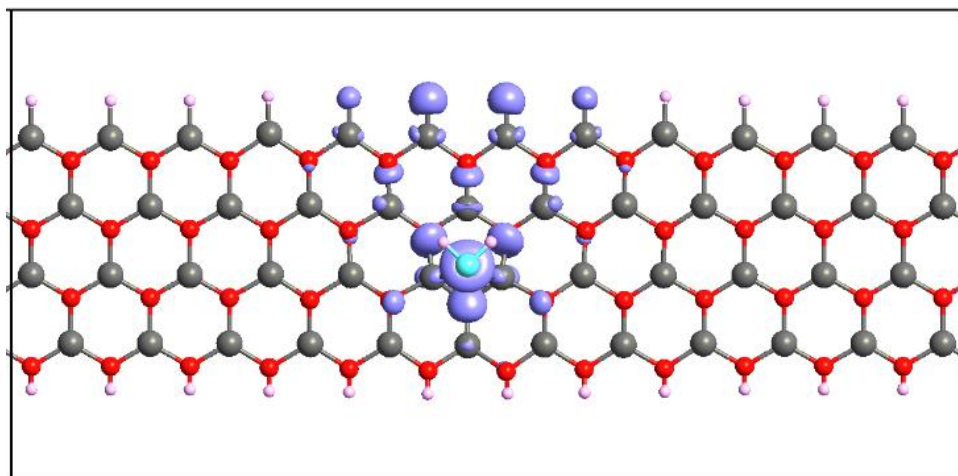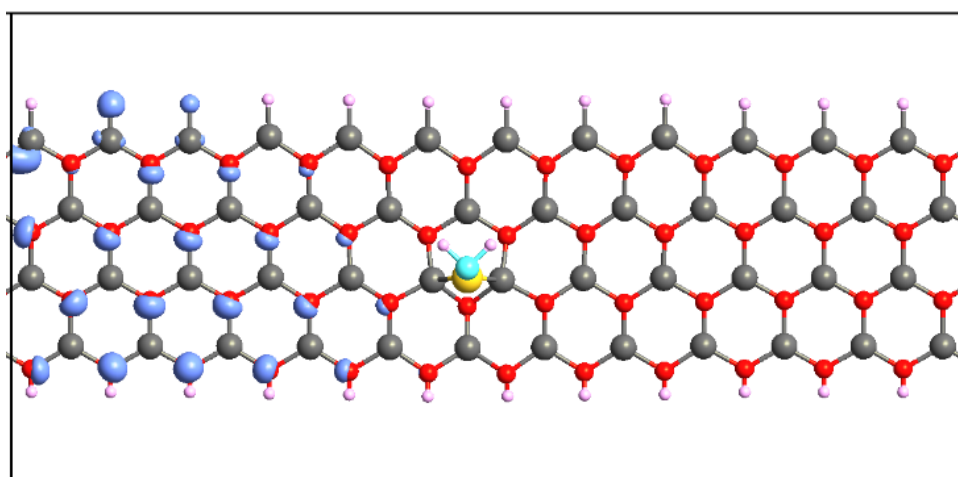
4.5 IV Characteristics

Figure 4.5 shows the results of simulated IV curves when a bias range from zero up to 1 V is applied on the four devices under focus. In each panel, the dotted black curve stands for IV curve due to pristine ZnO-NR without catalyst and without molecule. The green curve and red curve stand for the IV curves corresponding to the device with catalyst before and after the occurrence of chemisorption with the molecule, respectively. All the four devices with catalysts seem to exhibit negative differential resistance (NDR) behavior, which might be originated from the narrowness of the nanoribbon (i.e., finite number of conductive channels), in which quantum coherence has a pronounced effect. NDR behavior is very pronounced in case of Fe and Ag catalysts.

In case of chemisorption of H_2, it causes more rectification on Pt than it does on Pd. In Pt, H_2 is playing the role of n-type doping, it saturates the dangling bonds and enhances the n-type conductivity. However, on Pd, H_2 persists to keep NDR behavior but reduces top-to-valley ratio (i.e., less NDR behavior). It is obvious that regarding the transport properties, the effect of H_2 chemisorption on Pt is larger than the one on Pd. Meanwhile, we emphasize that we focus in our discussion on biases larger than 0.4 V, which correspond to the range of probing conduction band states, as the bandgap energy of pristine ZnO-NR is about 0.4 eV.

In cases of chemisorption processes of CO_2 on Fe catalyst and H_2S on Ag catalyst, NDR behaviors of the devices before the arrivals of molecules are very noticeable with large top-to-valley ratios. The chemisorption of the molecule on the catalyst enormously reduces the NDR behaviors and definitely improves the transport

properties. Such modifications would be relevant to the sensitivity of gas sensing as will be further discussed below.

Meanwhile, hampering the transport properties as in case of H_2S/Au due to the effect of HOMO and LUMO strong confinement around the catalyst would cause a huge reduction in the electric current. This by itself might also cause good sensor's response, as will be further discussed below.
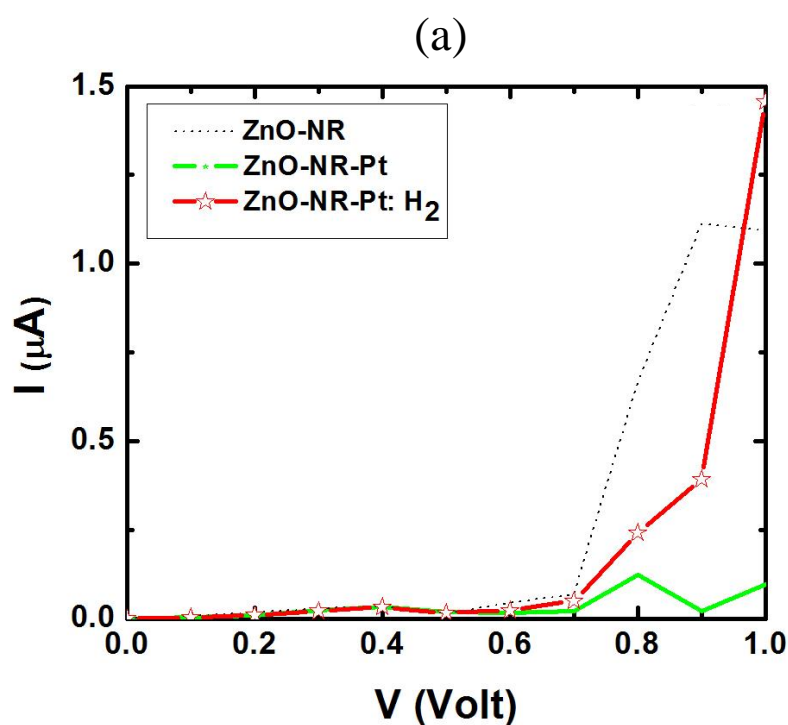
Figure 4.5 : IV Curves of catalysts on ZnO-NR devices
The black dotted curve represents pristine ZnO-NR. The green curve represents (a) Pt, (b) Pd, (c) Fe, (d) Ag, and (e) Au catalyst adsorbed on the ZnO-NR. The red curve represents (a) H_2 gas chemisorbed on Pt, (b) H_2 gas chemisorbed on Pd, (c) CO_2 gas chemisorbed on Fe, (d) H_2S chemisorbed on Ag, and (e) H_2S chemisorbed on Au.

(b)

(c)

Figure 4.5 : IV Curves of catalysts on ZnO-NR devices (continued)
The black dotted curve represents pristine ZnO-NR. The green curve represents (a) Pt, (b) Pd, (c) Fe, (d) Ag, and (e) Au catalyst adsorbed on the ZnO-NR. The red curve represents (a) H_2 gas chemisorbed on Pt, (b) H_2 gas chemisorbed on Pd, (c) CO_2 gas chemisorbed on Fe, (d) H_2S chemisorbed on Ag, and (e) H_2S chemisorbed on Au.

(d)

(e)

Figure 4.5 : IV Curves of catalysts on ZnO-NR devices (continued)
The black dotted curve represents pristine ZnO-NR. The green curve represents (a) Pt,
(b) Pd, (c) Fe, (d) Ag, and (e) Au catalyst adsorbed on the ZnO-NR. The red curve
represents (a) H_2 gas chemisorbed on Pt, (b) H_2 gas chemisorbed on Pd, (c) CO_2 gas
chemisorbed on Fe, (d) H_2S chemisorbed on Ag, and (e) H_2S chemisorbed on Au.

4.6 Resistance and Sensor Response

The differential resistance is calculated within the approximation of linear smoothening of IV curves and using a bias spacing of $\Delta V = H = 0.1$ V (i.e., errors of differential resistance is at the order of $O(H^2)$). The results are presented in Figure 4.6 for the five samples of interest before the occurrence of chemisorption. Before the arrival of molecule, all five ZnO-NR samples with catalyst (a) Pt, (b) Pd, (c) Fe, (d) Ag, and (e) Au show fluctuations of differential resistance as the bias varies within the range of 0-1 V. NDR persists in existing in all the five samples due to the existence of quantum coherence effects in the devices.
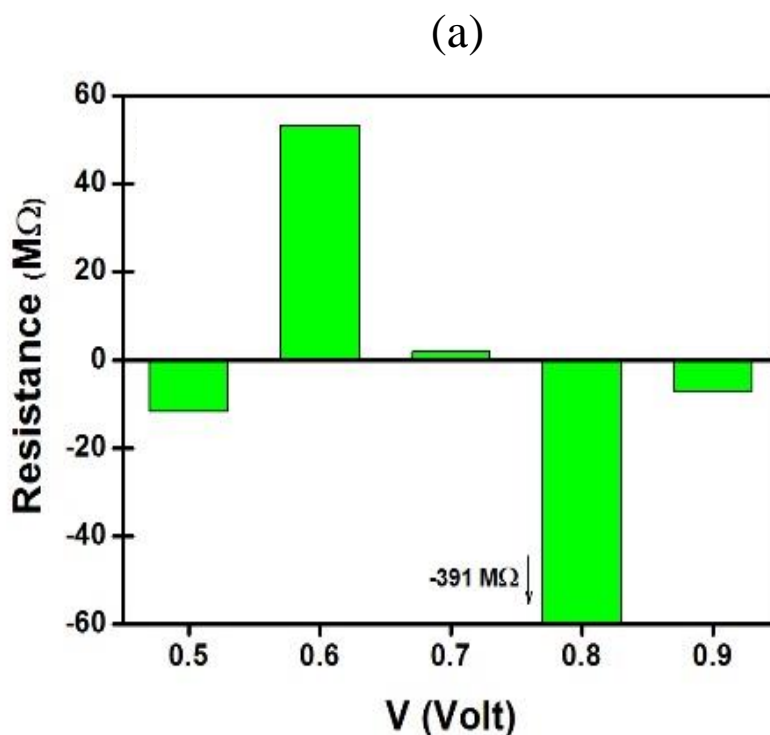
Figure 4.6 : Differential Resistance of catalysts on ZnO-NR devices
(a) Pt catalyst (b) Pd catalyst (c) Fe catalyst (d) Ag catalyst (e) Au catalyst
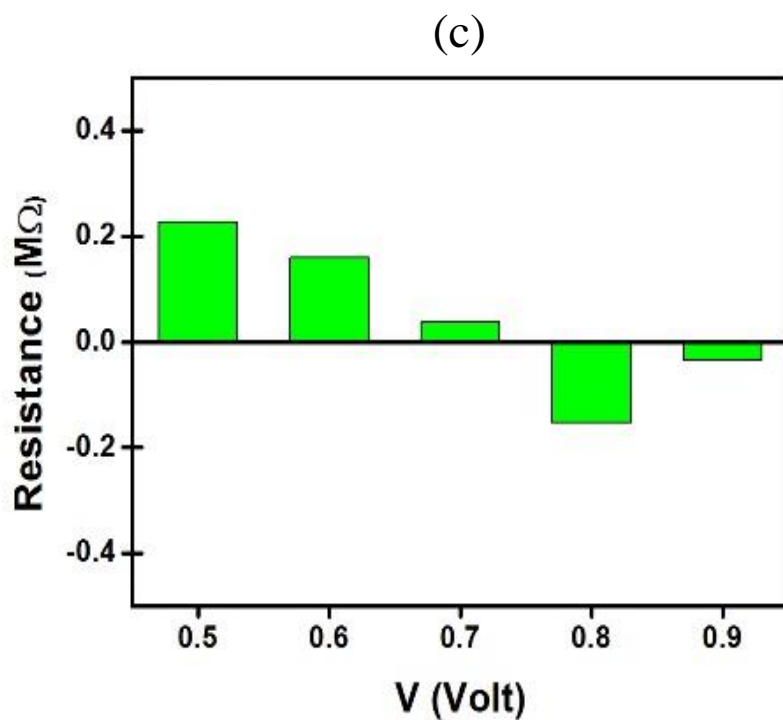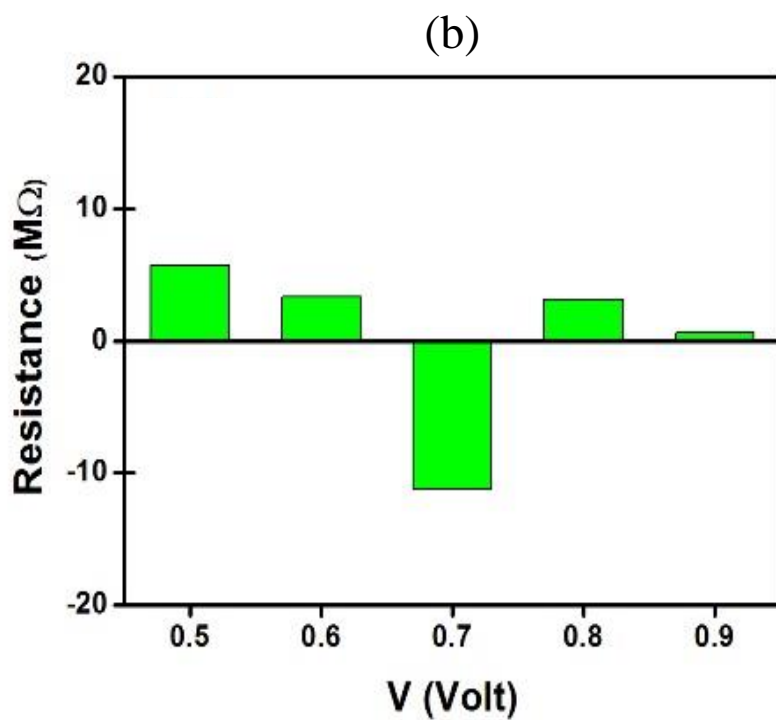
(b)

(c)

Figure 4.6 : Differential Resistance of catalysts on ZnO-NR devices (continued)
(a) Pt catalyst (b) Pd catalyst (c) Fe catalyst (d) Ag catalyst (e) Au catalyst

(d)

(e)
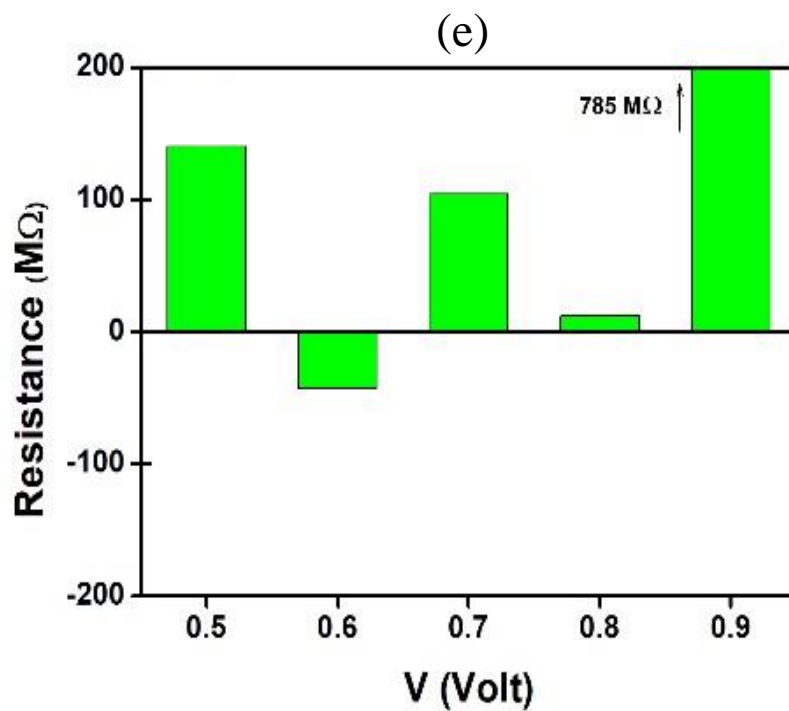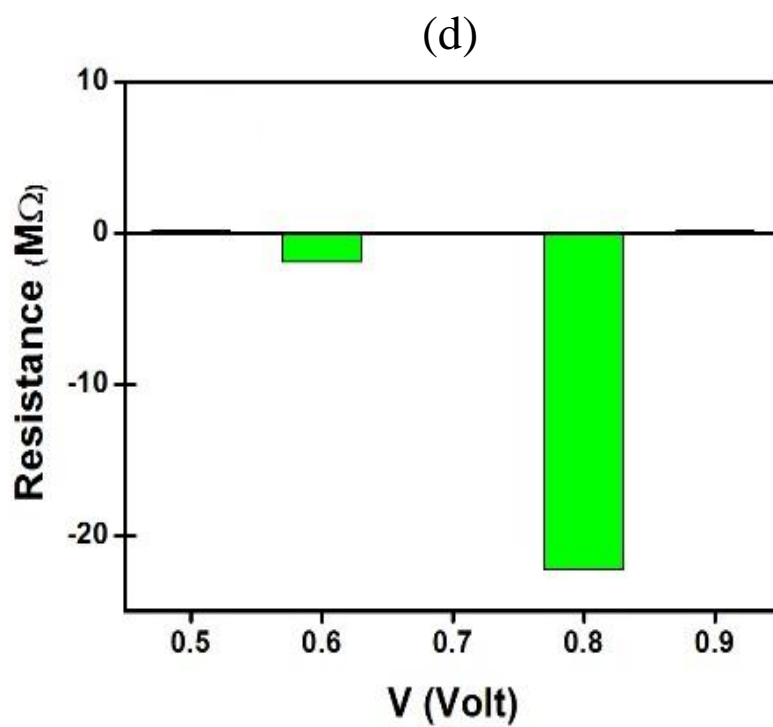
Figure 4.6 : Differential Resistance of catalysts on ZnO-NR devices (continued)
(a) Pt catalyst (b) Pd catalyst (c) Fe catalyst (d) Ag catalyst (e) Au catalyst

Figure 4.7 presents the results after the arrivals of molecules and the occurrence of chemisorption of: (a) H_2 on Pt, (b) H_2 on Pd, (c) CO_2 on Fe, (d) H_2S on Ag, and (e) H_2S on Au, fluctuations of differential resistance reduces enormously in some samples, due to the saturation of dangling bonds, change in confinement characters of HOMO and LUMO states. The variance of differential resistance from before to after the arrival of molecule would be important in gas sensitivity (or also named "sensor response").
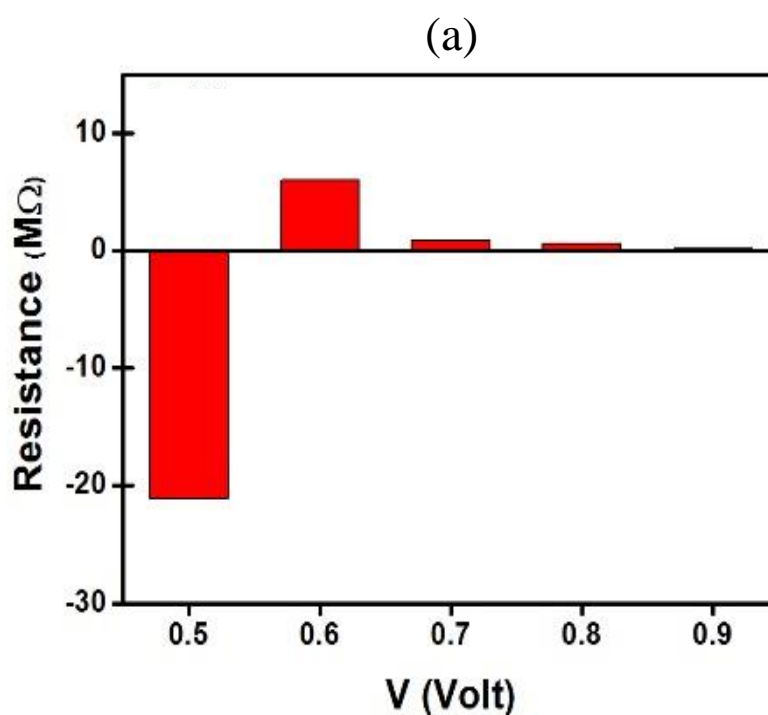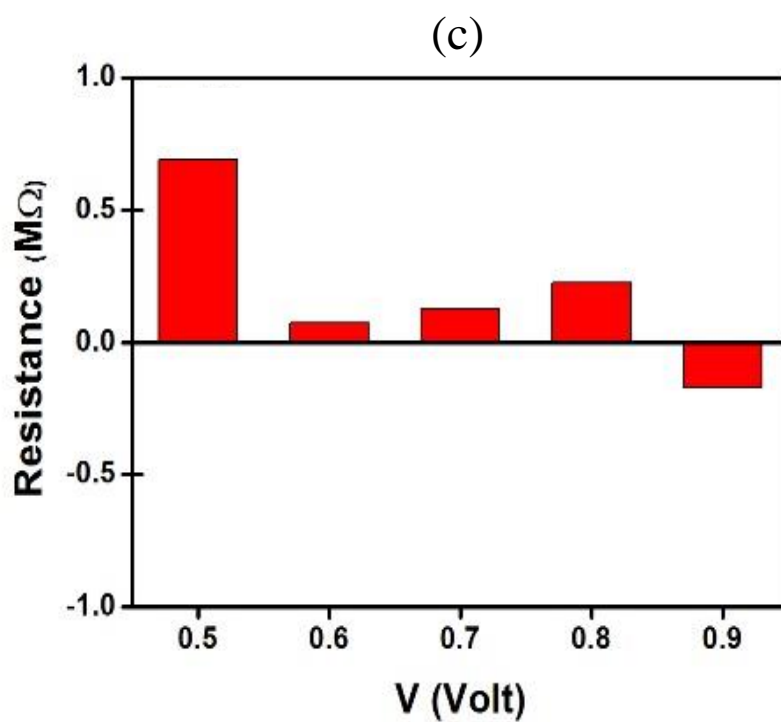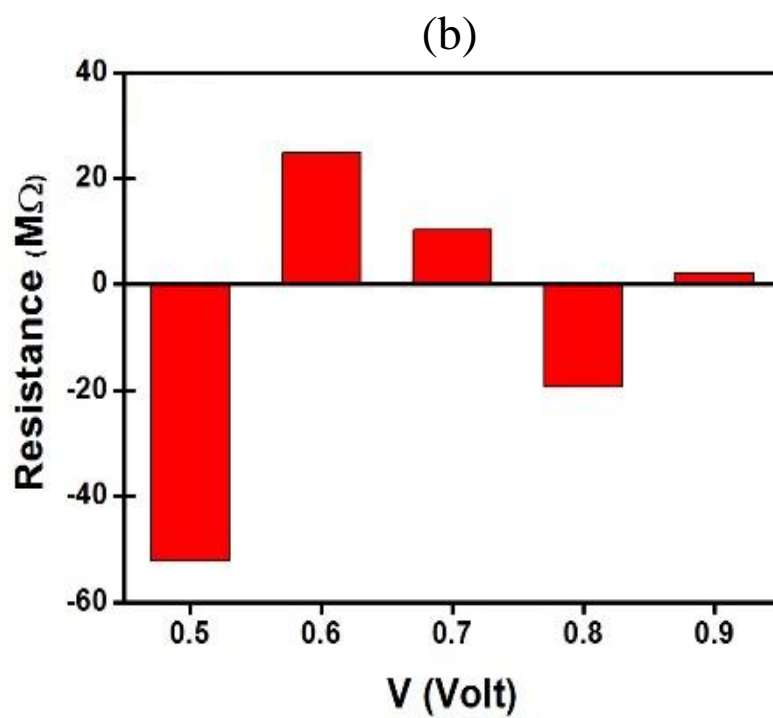
Figure 4.7 : Differential Resistance of catalysts and gas molecule on ZnO-NR devices
(a) H_2 on Pt catalyst (b) H_2 on Pd catalyst (c) CO_2 on Fe catalyst (d) H_2S on Ag catalyst (e) H_2S on Au catalyst.

Figure 4.7 : Differential Resistance of catalysts and gas molecule on ZnO-NR devices (continued)
(a) H_2 on Pt catalyst (b) H_2 on Pd catalyst (c) CO_2 on Fe catalyst (d) H_2S on Ag catalyst (e) H_2S on Au catalyst.

(d)

(e)
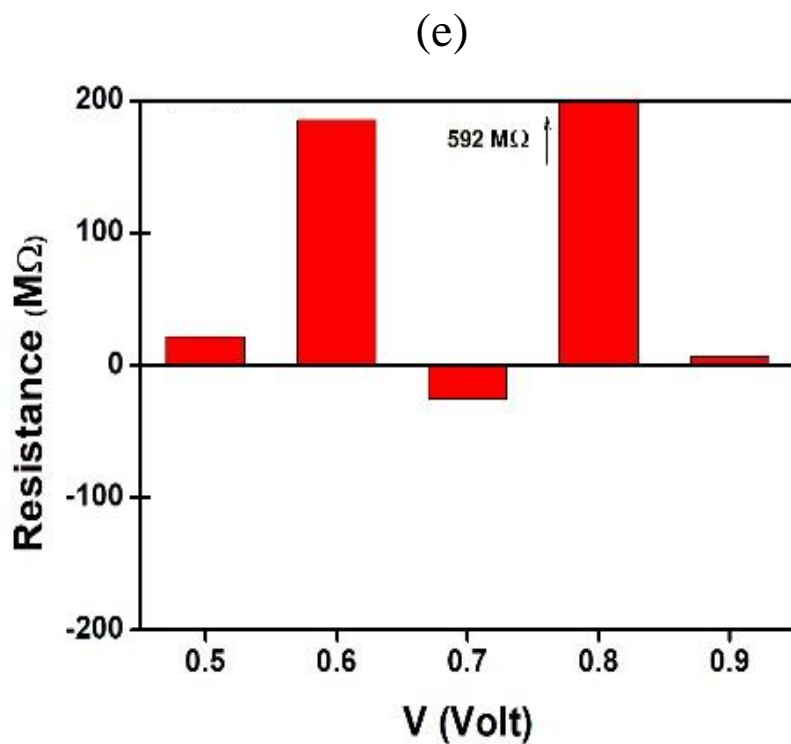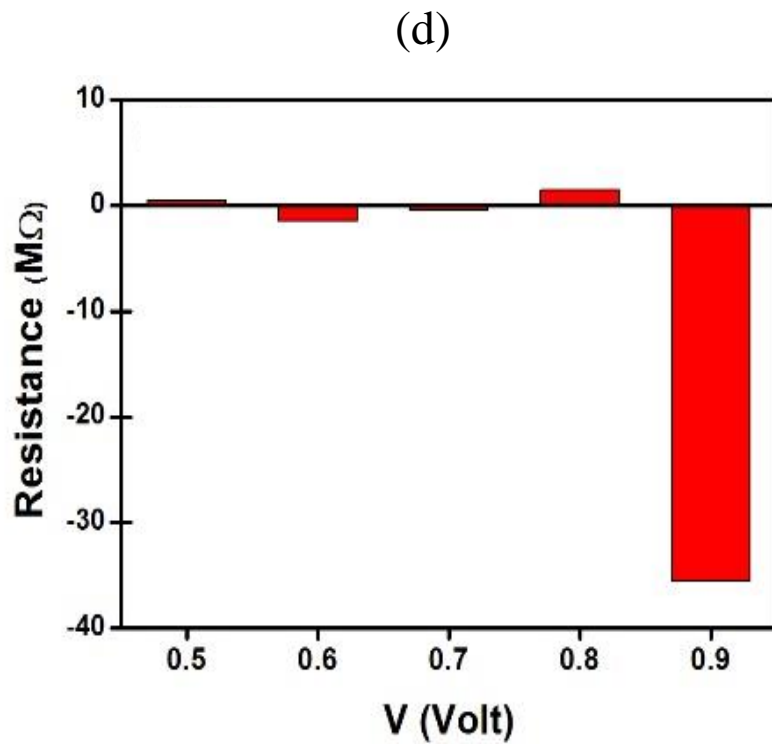
Figure 4.7 : Differential Resistance of catalysts and gas molecule on ZnO-NR devices (continued)
(a) H_2 on Pt catalyst (b) H_2 on Pd catalyst (c) CO_2 on Fe catalyst (d) H_2S on Ag catalyst (e) H_2S on Au catalyst.

Actually, based on the results of differential resistance, the sensor response is evaluated and presented in Figure 4.8 The averages of sensor responses to the gases: (a) H_2 on Pt, (b) H_2 on Pd, (c) CO_2 on Fe, (d) H_2S on Ag, and (e) H_2S on Au, after getting averaged over the shown five biases, are displayed in dotted lines. The obtained average values of sensor response are: S_{avg} = 1.09, 0.996, 16.5, 8.81, and 0.804 to correspond to the previous panels, respectively.

Figure 4.8 : Sensor Response of catalysts on ZnO-NR devices
(a) H_2 on Pt catalyst (b) H_2 on Pd catalyst (c) CO_2 on Fe catalyst (d) H_2S on Ag catalyst (e) H_2S on Au catalyst.

(b)

(c)

Figure 4.8 : Sensor Response of catalysts on ZnO-NR devices (continued)
(a) H_2 on Pt catalyst (b) H_2 on Pd catalyst (c) CO_2 on Fe catalyst (d) H_2S on Ag catalyst (e) H_2S on Au catalyst.

(d)

(e)
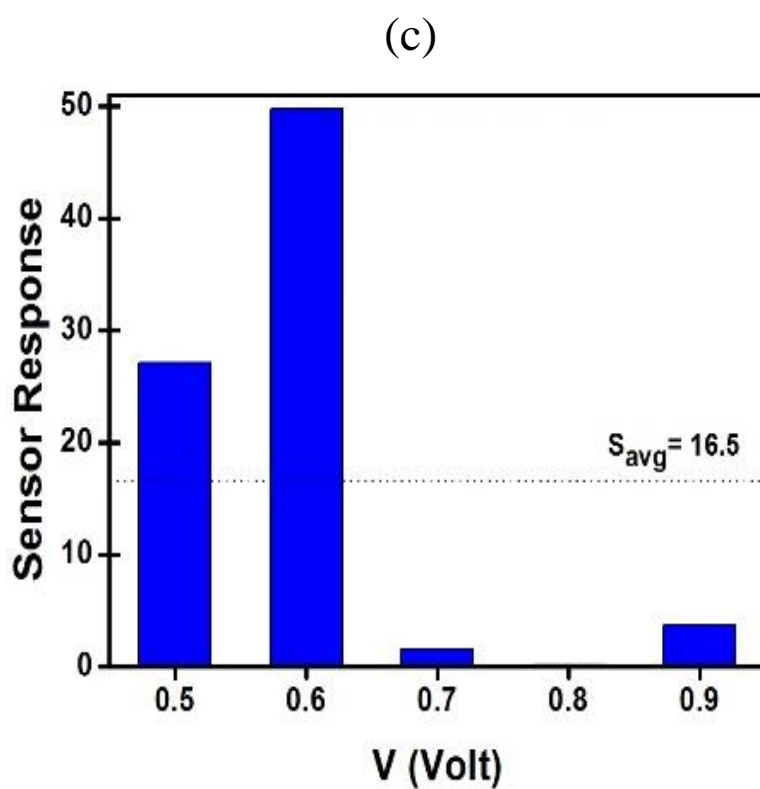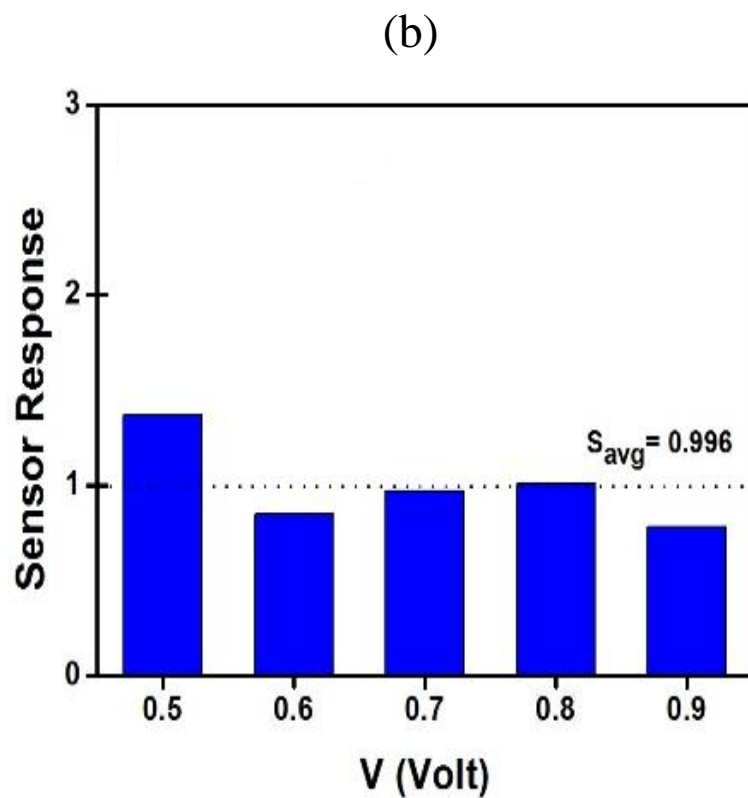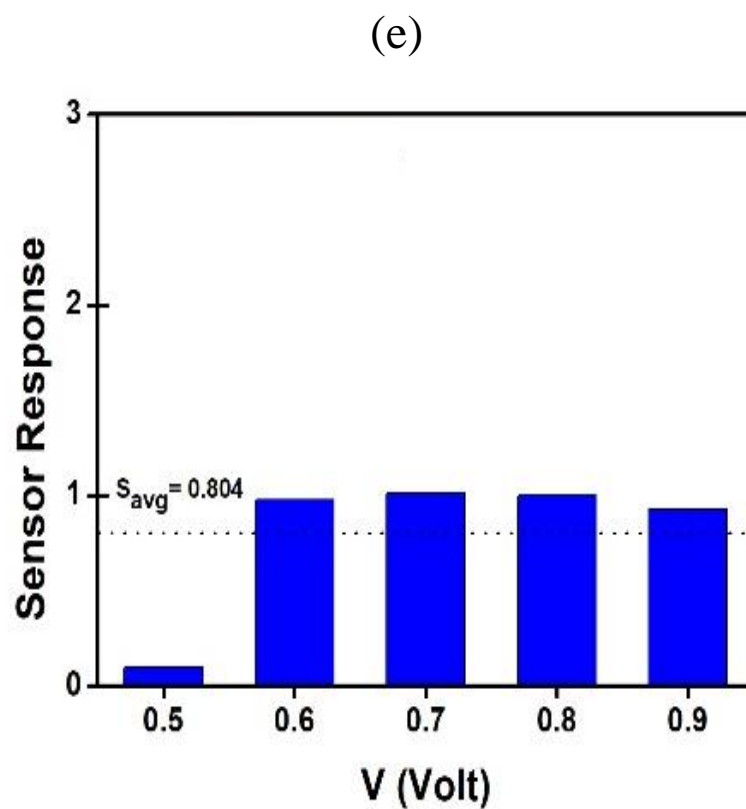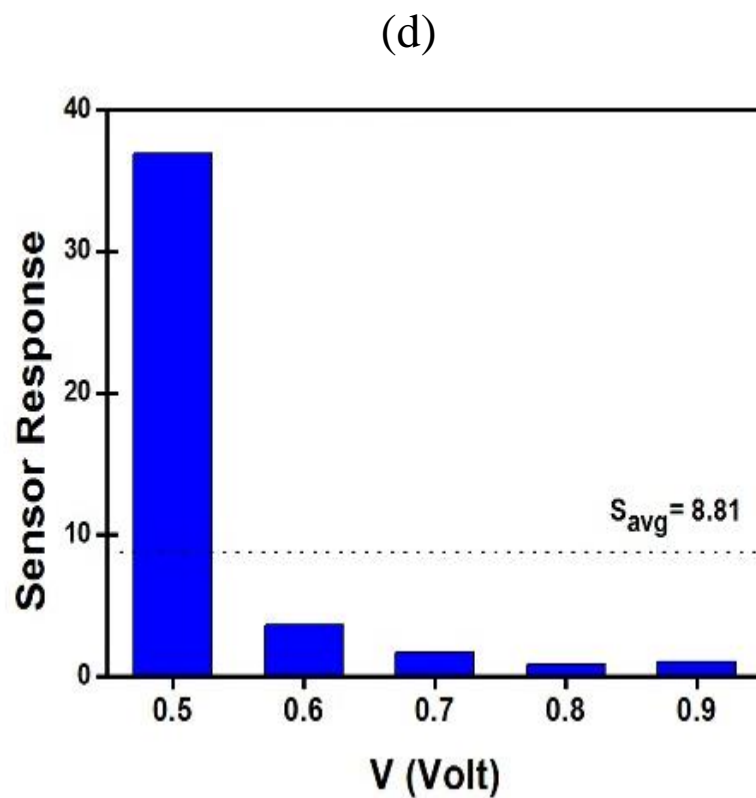
Figure 4.8 : Sensor Response of catalysts on ZnO-NR devices (continued)
(a) H_2 on Pt catalyst (b) H_2 on Pd catalyst (c) CO_2 on Fe catalyst (d) H_2S on Ag catalyst (e) H_2S on Au catalyst.

In order to further inspect the selectivity of each catalyst, we present in Figure 4.9 the sensor response of each catalyst when exposed to different gases at RT. While both Pt and Pd catalysts exhibit chemisorption processes at RT, they show no selectivity toward any case. Fe catalyst at RT exhibits physisorption processes with three gases (H_2, H_2S and N_2) and chemisorption processes with CO_2 and O_2. Nonetheless, Fe can be a good candidate for selectivity of CO_2 detection at RT. On the other hand, Ag catalyst exhibits physisorption processes with H_2 and CO_2 but chemisorption ones with H_2S, N_2 and O_2, with a relatively high selectivity towards H_2S at RT. Last but not least, Au exhibits chemisorption processes toward just two gases (H_2S and O_2); so it can be a good candidate for selectivity of H_2S at RT. Taking into account that oxygen and nitrogen being the main components in the air, then both Ag and Au should be the best to suit the detection of H_2 at RT. Furthermore, it is noticeable that all the studied catalysts do have high sensor response toward O_2; as it seems that oxidation is active process on all of them at RT.
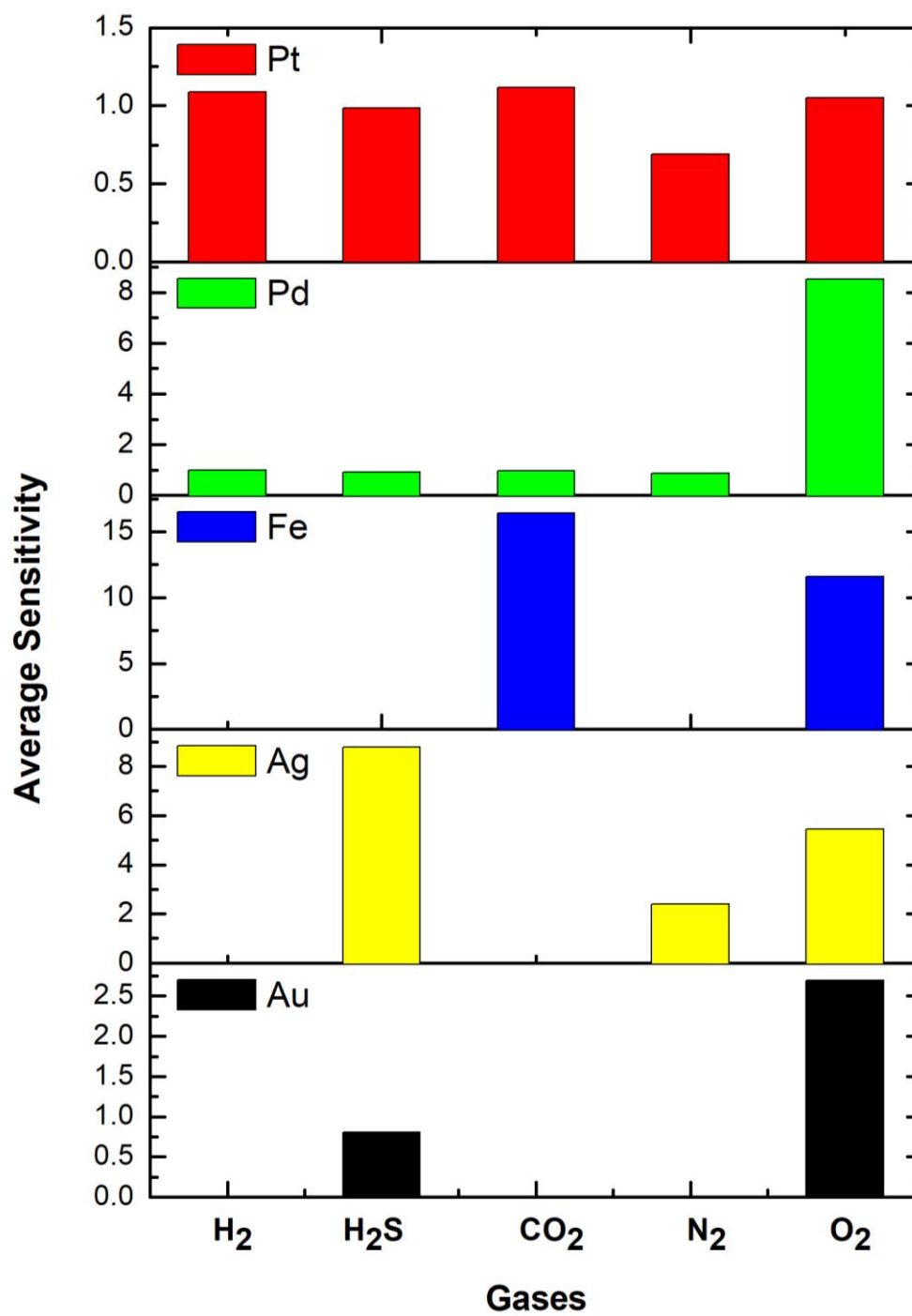
Figure 4.9 : Average sensor responses of the five catalysts versus various gases (e.g., H_2, H_2S, CO_2, N_2 and O_2) at RT.

Chapter 5: Conclusion

A combination of DFT and NEGF formalism is utilized to investigate the adsorption and transport properties of ZnO-NR based devices in order to assess their suitability for gas sensing applications. This thesis mainly focused on two different studies, (i) to study the effect of doping; and (ii) to study the effect of transition-metal catalysts on the sensor response of ZnO-NR based sensors. The main aims are to achieve selectivity towards three pollutant gases H_2, H_2S and CO_2 of interest in both energy and environmental sectors. Dopant like nitrogen element (N) was substituted by oxygen atom on hydrogen-passivated zigzag-edged ZnO-NRs. Accordingly, N-doped ZnO-NR based devices exhibited selectivity towards the chemisorption of H_2 and O_2 gas molecules. Following the atomic relaxations, the IV curves were calculated. Results can be summarized as follows:

(1) The IV characteristics of the ZnO-NR:N based device exhibits a negative differential resistance behavior. Such a trend is attributed to the unpaired electron on the dopant N-atom. Further work is planned to understand the origins of such NDR trend (see Chapter 3);

(2) The chemisorption of H_2 molecule is associated with a dissociation of the molecule causing a formation of an extended defect near the vicinity of N-site. The two H-atoms behave as donors and deliver charge (i.e., $\Delta q = +0.74e$) to the surface enough to not only saturate the N-dangling bonds but rather to rectify and to enhance the conductivity;

(3) The chemisorption of O_2 molecule is not associated with dissociation but just breaking of the π-bond to pave the way to its two oxygen atoms to form two new chemical bonds O-N and O-Zn. Such mechanism of chemisorption makes the

desorption process an easy task. The O-atoms of O_2 molecule play role of acceptors to drain charge from N-site and making it more depleted (i.e., Δq = -0.60e). Thus, this causes a reduction of conductivity and an extension of the NDR range;

(4) In case of combination of V_O and N-doping, before and after the chemisorption of H_2, no evidence for existence of NDR behavior is shown. The V_O seems able to provide enough charge to saturate the N dangling bonds and enhance the conductivity.

On the other hand, catalysts based on transition metal atoms (e.g., Pt, Pd, Au, Ag, and Fe) were deposited on hydrogen-passivated zigzag-edged ZnO-NRs. Various gas molecules (e.g., H_2, H_2S, CO_2, O_2 and N_2) were tested for adsorption on these catalysts at RT. Following the atomic relaxations, the IV curves were calculated also at RT. Results can be summarized as follows:

(1) No selectivity can be obtained using Pt and Pd at RT. There is an experimental evidence that these latter catalysts do have good selectivity towards H_2 gas at higher temperatures (like 400 ºC) [96, 97], which we did not test yet.

(2) Selectivity towards H_2S gas can be achieved at RT using either Ag or Au catalysts. Besides, the selectivity towards CO_2 can also be reached using Fe catalyst at RT.

(3) It is remarkable that all the studied catalysts to have good sensor response to oxygen, as the oxidation seems active at RT.

(4) Our results are in good agreement with experimental observations. Namely, the experimental work of Drmosh et al. [96, 97] corroborate the lack of selectivity of ZnO to detect H_2 at RT, when Pt catalyst is used. The experimental work, reported by Russell group [98], provides a strong evidence of the detection of H_2S on Ag at low temperatures. Again, detection of H_2S is realized at room temperature using

gold nanoparticles decorating CNTs, as was reported by Wang et al. [29] and Mubeen et al. [99]. Mishra and Ramaprabhu [46, 47] provide an experimental evidence of adsorption of CO_2 on iron at RT, in cases of magnetite decorating either graphene or MWCNTs. Similar role is played by Fe in the adsorption of CO_2 at RT in metal-organic frameworks (MOFs), as reported by Asgari et al. [100].

References

[1]   S. Zampolli, I. Elmi, F. Ahmed, M. Passini, G.C. Cardinali, …& L. Dori,"An electronic nose based on solid state sensor arrays for low-cost indoor air quality monitoring applications," *Sensors Actuators, B Chem.*, vol. 101, no. 1–2, pp. 39–46, 2004.

[2]   X. Liu, S. Cheng, H. Liu, S. Hu, D. Zhang, and H. Ning, "A survey on gas sensing technology," *Sensors (Switzerland)*, vol. 12, no. 7, pp. 9635–9665, 2012.

[3]   Y. F. Sun, S.B. Liu, F.L. Meng, J.Y. Liu, Z. Jin, …& J.H. Liu, "Metal oxide nanostructures and their gas sensing properties: A review," *Sensors*, vol. 12, no. 3, pp. 2610–2631, 2012.

[4]   Q. Wu, J. Li, and S. Sun, "Nano SnO_2 Gas Sensors," *Curr. Nanosci.*, vol. 2, pp. 525–538, 2010.

[5]   A. Sivapunniyam, N. Wiromrat, M. Tay, Z. Myint, and J. Dutta, "High-performance liquefied petroleum gas sensing based on nanostructures of zinc oxide and zinc stannate," *Sensors Actuators B. Chem.*, vol. 157, no. 1, pp. 232–239, 2011.

[6]   G. Neri, "First Fifty Years of Chemoresistive Gas Sensors," *Chemosensors*, vol. 3, no. 1, pp. 1–20, 2015.

[7]   G. F. Fine, L. M. Cavanagh, A. Afonja, and R. Binions, "Metal oxide semiconductor gas sensors in environmental monitoring," *Semicond. Gas Sensors*, vol. 10, pp. 5469–5502, 2010.

[8]   S. J. Patil, A.V. Patil, C.G. Dighavkar, K.S. Thakare, R.Y. Borase, …& R.R. Ahire, "Semiconductor metal oxide compounds based gas sensors: A literature review," *Front. Mater. Sci.*, vol. 9, no. 1, pp. 14–37, 2015.

[9]   C. Wang, L. Yin, L. Zhang, D. Xiang, and R. Gao, "Metal Oxide Gas Sensors: Sensitivity and Influencing Factors," *Sensors*, vol. 10, no. 3. pp. 2088–2106, 2010.

[10]   S. Leonardi, "Two-Dimensional Zinc Oxide Nanostructures for Gas Sensor Applications," *Chemosensors*, vol. 5, no. 17, pp. 1-28, 2017.

[11]   Z. L. Wang, "Zinc oxide nanostructures: growth, properties and applications," *J. Phys. Condens. Matter*, vol. 16, no. 25, pp. R829–R858, 2004.

[12]   P. Shankar, J. Bosco, and B. Rayappan, "Gas sensing mechanism of metal oxides : The role of ambient atmosphere, type of semiconductor and gases - A review," *Sci. Lett. J.*, vol. 4, no. 126, pp. 1-18, 2015.

[13]   D. R. Miller, S. A. Akbar, and P. A. Morris, "Nanoscale metal oxide-based heterojunctions for gas sensing: A review," *Sensors Actuators, B Chem.*, vol. 204, pp. 250–272, 2014.

[14] H. J. Kim and J. H. Lee, "Highly sensitive and selective gas sensors using p-type oxide semiconductors: Overview," *Sensors Actuators, B Chem.*, vol. 192, pp. 607–627, 2014.

[15] A. Kolodziejczak-Radzimska and T. Jesionowski, "Zinc oxide-from synthesis to application: A review," *Materials (Basel).*, vol. 7, pp. 2833–2881, 2014.

[16] N. Singh, R. M. Mehra, and A. Kapoor, "Synthesis and characterization of zno nanoparticles," *J. Nano. Electron. Phys.*, vol. 36, no. 3, pp. 132–139, 2011.

[17] A. Janotti and C. G. Van de Walle, "Fundamentals of zinc oxide as a semiconductor," *Reports Prog. Phys.*, vol. 72, no. 12, pp. 1-29, 2009.

[18] R. Y. Hong *et al.*, "Synthesis, surface modification and photocatalytic property of ZnO nanoparticles," *Powder Technol.*, vol. 189, no. 3, pp. 426–432, 2009.

[19] H. Wang, C. Li, H. Zhao, and J. Liu, "Preparation of nano-sized flower-like ZnO bunches by a direct precipitation method," *Adv. Powder Technol.*, vol. 24, no. 3, pp. 599–604, 2013.

[20] V. A. Coleman and C. Jagadish, "Zinc Oxide Bulk, Thin Films and Nanostructures," *UK, Elsevier*, pp. 1–5, 2006.

[21] P. J. P. Espitia, C. G. Otoni, and N. F. F. Soares, "Chapter 34 - Zinc Oxide Nanoparticles for Food Packaging Applications," J. B. T.-A. F. P. Barros-Velázquez, Ed. San Diego: Academic Press, pp. 425–431, 2016.

[22] N. Singh, R. M. Mehra, and A. Kapoo, "Synthesis and characterization of ZnO nanoparticles," *Journal of Nano and Electronic Physics*, vol. 3, no. 1, pp. 132-139, 2011.

[23] A. Tsukazaki *et al.*, "Repeated temperature modulation epitaxy for p-type doping and light-emitting diode based on ZnO," *Nature materials*, vol. 4, pp. 42-46, January, 2005.

[24] Y. Chen, D. Bagnall, and T. Yao, "ZnO as a novel photonic material for the UV region," *Mater. Sci. Eng. B75*, vol. 75, pp. 190–198, 2000.

[25] H.-J. Kim, C.-H. Lee, D.-W. Kim, and G.-C. Yi, "Fabrication and electrical characteristics of dual-gate ZnO nanorod metal–oxide semiconductor field-effect transistors," *Nanotechnology*, vol. 17, no. 11, pp. S327–S331, 2006.

[26] Ü. Özgür, Y. I. Alivov, and C. Liu, "A comprehensive review of ZnO materials and devices," *J. Appl. Pys.*, vol. 98, pp. 041301(1)-041301(105), 2005.

[27] A. Kudo and Y. Miseki, "Heterogeneous photocatalyst materials for water splitting," *Chem. Soc. Rev.*, vol. 38, no. 1, pp. 253–278, 2009.

[28] R. Singh and H. S. Nalwa, "Medical Applications of Nanoparticles in Biological Imaging , Cell Labeling, Antimicrobial Agents, and Anticancer Nanodrugs," *J. Biomed. Nanotechnol*, vol. 7, pp. 489–504, 2011.

[29] C. Wang, X. Chu, and M. Wu, "Detection of H_2S down to ppb levels at room

temperature using sensors based on ZnO nanorods," *Sensors Actuat. B.*, vol. 113, pp. 320–323, 2006.

[30]   M. Kaur, N. Jain, K. Sharma, S. Bhattacharya, M. Roy, …& J.V. Yakhmi, "Chemical Room-temperature H_2S gas sensing at ppb level by single crystal In_2O_3 whiskers," *Sensors Actuat. B.*, vol. 133, pp. 456–461, 2008.

[31]   S. C. Navale, S. W. Gosavi, and I. S. Mulla, "Controlled synthesis of ZnO from nanospheres to micro-rods and its gas sensing studies," *Talanta*, vol. 75, pp. 1315–1319, 2008.

[32]   J. X. Wang, X.W. Sun, A. Wei, Y. Lei, X.P. Cai, …& Z.L. Don, "Zinc oxide nanocomb biosensor for glucose detection," *Appl. phys. Lett*, vol. 88, pp. 233106(1)- 233106(3), 2006.

[33]   J. O. M. Backris, "Hydrogen economy in the future," *Int. J. Hydrogen Energy*, vol. 24, pp. 1–15, 1999.

[34]   L. Barreto, A. Makihira, and K. Riahi, "The hydrogen economy in the 21st century : a sustainable development scenario," *Int. J. Hydrogen Energy*, vol. 28, pp. 267–284, 2003.

[35]   T. Hübert, L. Boon-brett, G. Black, and U. Banach, "Hydrogen sensors – A review," *Sensors Actuators B Chem.*, vol. 157, pp. 329–352, 2011.

[36]   F. Rumiche, H. H. Wang, and J. E. Indacochea, "Development of a fast-response / high-sensitivity double wall carbon nanotube nanostructured hydrogen sensor," *Sensors Actuators B. Chem.*, vol. 163, no. 1, pp. 97–106, 2012.

[37]   V. Aroutiounian, "Metal oxide hydrogen , oxygen , and carbon monoxide sensors for hydrogen setups and cells," *Int. J. Hydrogen Energy*, vol. 32, pp. 1145–1158, 2007.

[38]   V. M. Aroutiounian, "Metal oxide hydrogen , oxygen and carbon monooxide sensors," *Int. Sci. J. Altern. Energy Ecol.*, vol. 3, pp. 12–22, 2005.

[39]   P. Patnaik, *A comprehensive guide to the hazardous properties of chemical substances*. John Wiley & Sons, 2007.

[40]   D. Sett and D. Basak, "Highly enhanced H_2 gas sensing characteristics of Co:ZnO nanorods and its mechanism," *Sensors Actuators B. Chem.*, vol. 243, pp. 475–483, 2017.

[41]   A. Paliwal, A. Sharma, M. Tomar, and V. Gupta, "Carbon monoxide (CO) optical gas sensor based on ZnO thin films," *Sensors Actuators B Chem.*, vol. 250, pp. 679–685, 2017.

[42]   L. Rana, R. Gupta, M. Tomar, and V. Gupta, "ZnO/ST-Quartz SAW resonator: An efficient NO_2 gas sensor," *Sensors Actuators B Chem.*, vol. 252, pp. 840–845, 2017.

[43]   L. Sun, W. L. Luan, T. C. Wang, W. X. Su, and L. X. Zhang, "Room-

temperature CO thermoelectric gas sensor based on Au/Co_3O_4 catalyst tablet," *Nanotechnology*, vol. 28, no. 7, pp. 75501(1)- 75501(10), 2017.

[44] G. Jiang *et al.*, "Free-Standing Functionalized Graphene Oxide Solid Electrolytes in Electrochemical Gas Sensors," *Adv. Funct. Mater.*, vol. 26, no. 11, pp. 1729–1736, 2016.

[45] K. Wetchakun *et al.*, "Semiconducting metal oxides as sensors for environmentally hazardous gases," *Sensors Actuators B Chem.*, vol. 160, no. 1, pp. 580–591, 2011.

[46] A. K. Mishra and S. Ramaprabhu, "Nano magnetite decorated multiwalled carbon nanotubes: a robust nanomaterial for enhanced carbon dioxide adsorption," *Energy Environ. Sci.*, vol. 4, no. 3, pp. 889–895, 2011.

[47] A. K. Mishra and S. Ramaprabhu, "Enhanced CO_2 capture in Fe_3O_4-graphene nanocomposite by physicochemical adsorption," *J. Appl. Phys.*, vol. 116, no. 6, pp. 64306(1)- 64306(5), 2014.

[48] Y. Li, M. Jiao, H. Zhao, and M. Yang, "High performance gas sensors based on in-situ fabricated ZnO/polyaniline nanocomposite: the effect of morphology on the sensing properties," *Sensors Actuators B Chem.*, vol. 264, pp. 285–295, 2018.

[49] J. Cai, C. Zhang, A. Khan, C. Liang, and W.-D. Li, "Highly transparent and flexible polyaniline mesh sensor for chemiresistive sensing of ammonia gas," *RSC Adv.*, vol. 8, no. 10, pp. 5312–5320, 2018.

[50] H. T. Hien, H. T. Giang, N. Van Hieu, T. Trung, and C. Van Tuan, "Elaboration of Pd-nanoparticle decorated polyaniline films for room temperature NH_3 gas sensors," *Sensors Actuators B Chem.*, vol. 249, pp. 348–356, 2017.

[51] A. I. Ayesh, A. F. S. Abu-Hani, S. T. Mahmoud, and Y. Haik, "Selective H_2S sensor based on CuO nanoparticles embedded in organic membranes," *Sensors Actuators B Chem.*, vol. 231, pp. 593–600, 2016.

[52] A. F. S. Abu-Hani, S. T. Mahmoud, F. Awwad, and A. I. Ayesh, "Design, fabrication, and characterization of portable gas sensors based on spinel ferrite nanoparticles embedded in organic membranes," *Sensors Actuators B Chem.*, vol. 241, pp. 1179–1187, 2017.

[53] M. Topsakal, S. Cahangirov, E. Bekaroglu, and S. Ciraci, "First-principles study of zinc oxide honeycomb structures," *Phys. Rev. B*, vol. 80, no. 23, pp. 235119(1)- 235119(14), 2009.

[54] J. M. Soler, E. Artacho, J. D. Gale, A. García, J. Junquera, …& D. Sánchez-Portal, "The SIESTA method for ab initio order-N materials simulation," *J. Phys. Condens. Matter*, vol. 14, no. 11, pp. 2745-2779, 2002.

[55] M. Brandbyge, J.-L. Mozos, P. Ordejón, J. Taylor, and K. Stokbro, "Density-functional method for nonequilibrium electron transport," *Phys. Rev. B*, vol. 65, no. 16, pp. 165401(1)-165401(17), 2002.

[56] J. Taylor, H. Guo, and J. Wang, "Ab initio modeling of quantum transport properties of molecular electronic devices," *Phys. Rev. B*, vol. 63, no. 24, pp. 245407(1)- 245407(13), 2001.

[57] J. P. Perdew, K. Burke, and M. Ernzerhof, "Generalized gradient approximation made simple," *Phys. Rev. Lett.*, vol. 77, no. 18, pp. 3865-3866, 1996.

[58] H. J. Monkhorst and J. D. Pack, "Special points for Brillouin-zone integrations," *Phys. Rev. B*, vol. 13, no. 12, pp. 5188-5192, 1976.

[59] S. Grimme, "Semiempirical GGA-type density functional constructed with a long-range dispersion correction," *J. Comput. Chem.*, vol. 27, no. 15, pp. 1787–1799, 2006.

[60] M. Büttiker, Y. Imry, R. Landauer, and S. Pinhas, "Generalized many-channel conductance formula with application to small rings," *Phys. Rev. B*, vol. 31, no. 10, pp. 6207-6215, 1985.

[61] M. A. Haija, A. F. S. Abu-Hani, N. Hamdan, S. Stephen, and A. I. Ayesh, "Characterization of H_2S gas sensor based on $CuFe_2O_4$ nanoparticles," *J. Alloys Compd.*, vol. 690, pp. 461–468, 2017.

[62] M. J. Madou and S. R. Morrison, *Chemical sensing with solid state devices*. Elsevier, 2012.

[63] S. J. Blanksby and G. B. Ellison, "Bond dissociation energies of organic molecules," *Acc. Chem. Res.*, vol. 36, no. 4, pp. 255–263, 2003.

[64] L. Pauling, "The nature of the chemical bond. IV. The energy of single bonds and the relative electronegativity of atoms," *J. Am. Chem. Soc.*, vol. 54, no. 9, pp. 3570–3582, 1932.

[65] F. Al-Dirini, F. M. Hossain, A. Nirmalathas, and E. Skafidas, "Asymmetrically-gated graphene self-switching diodes as negative differential resistance devices," *Nanoscale*, vol. 6, no. 13, pp. 7628–7634, 2014.

[66] Y. An, K. Wang, Z. Yang, Z. Liu, G. Jia, …& G. Xu, "Negative differential resistance and rectification effects in step-like graphene nanoribbons," *Org. Electron.*, vol. 17, pp. 262–269, 2015.

[67] L. Pauling, *The Nature of the Chemical Bond...*, vol. 260. Cornell university press Ithaca, NY, pp. 3175-3187, 1960.

[68] A. Qteish, "Electronegativity scales and electronegativity-bond ionicity relations: A comparative study," *J. Phys. Chem. Solids*, vol. 124, pp. 186–191, 2019.

[69] J. Ludwig, D. G. Vlachos, A. C. T. Van Duin, and W. A. Goddard, "Dynamics of the dissociation of hydrogen on stepped platinum surfaces using the ReaxFF reactive force field," *J. Phys. Chem. B*, vol. 110, no. 9, pp. 4274–4282, 2006.

[70] Y. Zhao, Y.-H. Kim, A. C. Dillon, M. J. Heben, and S. B. Zhang, "Hydrogen storage in novel organometallic buckyballs," *Phys. Rev. Lett.*, vol. 94, no. 15,

pp. 155504(1)-155504(4), 2005.

[71]   S. Amaya Roncancio, D. H. Linares, H. A. Duarte, G. Lener, and M. K. Sapag, "Effect of Hydrogen in Adsorption and Direct Dissociation of CO on Fe (100) Surface: A DFT Study," *American Journal of Analytical Chemistry*, vol. 6, pp. 38-46, 2015.

[72]   M. Pozzo and D. Alfe, "Hydrogen dissociation and diffusion on transition metal (= Ti, Zr, V, Fe, Ru, Co, Rh, Ni, Pd, Cu, Ag)-doped Mg (0001) surfaces," *Int. J. Hydrogen Energy*, vol. 34, no. 4, pp. 1922–1930, 2009.

[73]   A. Lyalin and T. Taketsugu, "A computational investigation of H_2 adsorption and dissociation on Au nanoparticles supported on TiO_2 surface," *Faraday Discuss.*, vol. 152, pp. 185–201, 2011.

[74]   A. Michaelides and P. Hu, "Hydrogenation of S to H_2S on Pt (111): a first-principles study," *J. Chem. Phys.*, vol. 115, no. 18, pp. 8570–8574, 2001.

[75]   Z. Jiang, P. Qin, and T. Fang, "Investigation on adsorption and decomposition of H_2S on Pd (1 0 0) surface: A DFT study," *Surf. Sci.*, vol. 632, pp. 195–200, 2015.

[76]   D. E. Jiang and E. A. Carter, "Effects of Alloying on the Chemistry of CO and H_2S on Fe Surfaces," *J. Phys. Chem. B*, vol. 109, no. 43, pp. 20469–20478, 2005.

[77]   C. Qin and J. L. Whitten, "Interaction of S, SH and H_2S with Ag (1 0 0)," *Surf. Sci.*, vol. 588, no. 1–3, pp. 83–91, 2005.

[78]   X. Zhang, L. Yu, X. Wu, and W. Hu, "Experimental sensing and density functional theory study of H_2S and SOF_2 adsorption on Au-modified graphene," *Adv. Sci.*, vol. 2, no. 11, pp. 1500101(1)-1500101(10), 2015.

[79]   Jo. Sang Jun, P. Dong Ho and H. Dong Seong, "Adsorption and dissociation reaction of carbon dioxide on Pt (111) and Fe (111) surface: MO-study," *Bull. Korean Chem. Soc.*, vol. 21, no. 8, pp. 779–784, 2000.

[80]   J. A. Hinojosa Jr, A. Antony, C. Hakanoglu, A. Asthagiri, and J. F. Weaver, "Adsorption of CO_2 on a PdO (101) thin film," *J. Phys. Chem. C*, vol. 116, no. 4, pp. 3007–3016, 2012.

[81]   N. Y. Dzade, A. Roldan, and N. H. de Leeuw, "Activation and dissociation of CO_2 on the (001),(011), and (111) surfaces of mackinawite (FeS): A dispersion-corrected DFT study," *J. Chem. Phys.*, vol. 143, no. 9, pp. 94703(1)- 94703(8), 2015.

[82]   M. R. Singh, J. D. Goodpaster, A. Z. Weber, M. Head-Gordon, and A. T. Bell, "Mechanistic insights into electrochemical reduction of CO_2 over Ag using density functional theory and transport models," *Proc. Natl. Acad. Sci.*, vol. 114, no. 42, pp. E8812–E8821, 2017.

[83]   H. Mistry, R. Reske, Z. Zeng, Z. J. Zhao, J. Greeley, …& B. R. Cuenya,"Exceptional size-dependent activity enhancement in the

electroreduction of CO_2 over Au nanoparticles," *J. Am. Chem. Soc.*, vol. 136, no. 47, pp. 16473–16476, 2014.

[84] D. C. Ford, Y. Xu, and M. Mavrikakis, "Atomic and molecular adsorption on Pt (1 1 1)," *Surf. Sci.*, vol. 587, no. 3, pp. 159–174, 2005.

[85] M. Lynch and P. Hu, "A density functional theory study of CO and atomic oxygen chemisorption on Pt (111)," *Surf. Sci.*, vol. 458, no. 1–3, pp. 1–14, 2000.

[86] J. Shah, S. Kansara, S. K. Gupta, and Y. Sonvane, "Oxygen adsorption on palladium monolayer as a surface catalyst," *Phys. Lett. A*, vol. 381, no. 36, pp. 3084–3088, 2017.

[87] W. Wang, G. Wang, and M. Shao, "First-principles modeling of direct versus oxygen-assisted water dissociation on Fe (100) surfaces," *Catalysts*, vol. 6, no. 2, pp. 29(1)-29(11), 2016.

[88] W.-X. Li, C. Stampfl, and M. Scheffler, "Subsurface oxygen and surface oxide formation at Ag (111): A density-functional theory investigation," *Phys. Rev. B*, vol. 67, no. 4, pp. 45408(1)- 45408(16), 2003.

[89] H. Shi and C. Stampfl, "First-principles investigations of the structure and stability of oxygen adsorption and surface oxide formation at Au (111)," *Phys. Rev. B*, vol. 76, no. 7, pp. 75327(1)- 75327(14), 2007.

[90] M. Wilf and P. T. Dawson, "Adsorption of nitrogen on platinum," *Surf. Sci.*, vol. 60, no. 2, pp. 561–581, 1976.

[91] T. Matsubara, T. Nagai, M. Nagaoka, and T. Yamabe, "Ab Initio MO Study of the Structures of N_2, NO, and CO Molecules Coordinated to the Pd n (n= 1, 2, 5, 25) Clusters as a Model of Pd (110) Surface," *J. Phys. Chem. B*, vol. 105, no. 16, pp. 3235–3244, 2001.

[92] G. Ertl, S. B. Lee, and M. Weiss, "Kinetics of nitrogen adsorption on Fe (111)," *Surf. Sci.*, vol. 114, no. 2–3, pp. 515–526, 1982.

[93] P. J. Rous, "The lifetime and energy of the 2Πg shape resonance of N_2 adsorbed on Ag (111): the role of the substrate electronic structure," *Surf. Sci.*, vol. 326, no. 1–2, pp. 67–79, 1995.

[94] X. Ding, J. Yang, J. G. Hou, and Q. Zhu, "Theoretical study of molecular nitrogen adsorption on Au clusters," *J. Mol. Struct. THEOCHEM*, vol. 755, no. 1–3, pp. 9–17, 2005.

[95] Y. Gu, I. L. Kuskovsky, M. Yin, S. O'Brien, and G. F. Neumark, "Quantum confinement in ZnO nanorods," *Appl. Phys. Lett.*, vol. 85, no. 17, pp. 3833–3835, 2004.

[96] Q. A. Drmosh, Z. H. Yamani, and M. K. Hossain, "Hydrogen gas sensing performance of low partial oxygen-mediated nanostructured zinc oxide thin film," *Sensors Actuators B Chem.*, vol. 248, pp. 868–877, 2017.

[97] Q. A. Drmosh and Z. H. Yamani, "Hydrogen sensing properties of sputtered

ZnO films decorated with Pt nanoparticles," *Ceram. Int.*, vol. 42, no. 10, pp. 12378–12384, 2016.

[98] S. M. Russell, D.-J. Liu, M. Kawai, Y. Kim, and P. A. Thiel, "Low-temperature adsorption of H_2S on Ag (111)," *J. Chem. Phys.*, vol. 133, no. 12, pp. 124705(1)- 124705(8)-, 2010.

[99] S. Mubeen, T. Zhang, N. Chartuprayoon, Y. Rheem, A. Mulchandani, N. V. Myung, & M. A. Deshusses, M. A., "Sensitive detection of H_2S using gold nanoparticle decorated single-walled carbon nanotubes," *Anal. Chem.*, vol. 82, no. 1, pp. 250–257, 2009.

[100] M. Asgari, *S.* Jawahery, E.D. Bloch, M.R. Hudson, R. Flacau, … &W.L. Queen, "An experimental and computational study of CO_2 adsorption in the sodalite-type M-BTT (M= Cr, Mn, Fe, Cu) metal–organic frameworks featuring open metal sites," *Chem. Sci.*, vol. 9, no. 20, pp. 4579–4588, 2018.

[101] Y. Zhu and L. Liu, *Atomistic Simulation of Ouantum Transport in Nanoelectronic Devices*. World Scientific, 2016.

[102] S. Bohloul, L. Zhang, K. Gong, and H. Guo, "Theoretical impurity-limited carrier mobility of monolayer black phosphorus," *Appl. Phys. Lett.*, vol. 108, no. 3, pp. 33508(1)- 33508(8), 2016.

[103] P. A. Lee and A. D. Stone, "Universal conductance fluctuations in metals," *Phys. Rev. Lett.*, vol. 55, no. 15, pp. 1622-1625, 1985.

[104] Y. Imry, "Active transmission channels and universal conductance fluctuations," *EPL (Europhysics Lett.)*, vol. 1, no. 5, pp. 249-256, 1986.

[105] P. A. Mello, P. A. Mello, N. Kumar, and D. Narendra Kumar, *Quantum transport in mesoscopic systems: complexity and statistical fluctuations, a maximum-entropy viewpoint*, no. 4. Oxford University Press on Demand, 2004.

[106] E. Abrahams, P. W. Anderson, D. C. Licciardello, and T. V Ramakrishnan, "Scaling theory of localization: Absence of quantum diffusion in two dimensions," *Phys. Rev. Lett.*, vol. 42, no. 10, pp. 673-676, 1979.

[107] M. Kaveh, "A diffusive-hopping transition in a disordered two-dimensional system," *J. Phys. C Solid State Phys.*, vol. 18, no. 21, pp. 4165-4172, 1985.

[108] N. Tit, N. Kumar, J. W. Halley, and H. Shore, "Possibility of two types of localized states in a two-dimensional disordered lattice," *Phys. Rev. B*, vol. 47, no. 23, pp. 15988-15991, 1993.

[109] Y. Hu, H. Liu, H. Jiang, and X. C. Xie, "Numerical study of universal conductance fluctuations in three-dimensional topological semimetals," *Phys. Rev. B*, vol. 96, no. 13, pp. 134201(1)-134201(9), 2017.

[110] N. F. Mott, "Conduction in non-crystalline systems IX. the minimum metallic conductivity," *Philos. Mag. A J. Theor. Exp. Appl. Phys.*, vol. 26, no. 4, pp. 1015–1026, 1972.

[111] E. A. Davis and W. D. Compton, "Compensation dependence of impurity conduction in antimony-doped germanium," *Phys. Rev.*, vol. 140, no. 6A, pp. A2183, 1965.

[112] N. Tit, P. Pradhan, and N. Kumar, "Length-scale-dependent ensemble-averaged conductance of a 1D disordered conductor: Conductance minimum," *Phys. Rev. B*, vol. 49, no. 20, pp. 14715(1)-14715(14), 1994.

[113] D. Farka, A. O. F. Jones, R. Menon, N. S. Sariciftci, and P. Stadler, "Metallic conductivity beyond the Mott minimum in PEDOT: Sulphate at low temperatures," *Synth. Met.*, vol. 240, pp. 59–66, 2018.

[114] J. Kammhuber, M.C. Cassidy, H. Zhang, O. Gül, F. Pei, B. Nijholt, … & S.R. Plissard, "Conductance Quantization at Zero Magnetic Field in InSb Nanowires," *Nano Lett.*, vol. 16, no. 6, pp. 3482–3486, 2016.

[115] K. Terabe, T. Hasegawa, T. Nakayama, and M. Aono, "Quantized conductance atomic switch," *Nature*, vol. 433, no. 7021, pp. 47–50, 2005.

[116] H. Zhang, C. X. Liu, S. Gazibegovic, D. Xu, J. A. Logan, G. Wang, ... & R. L. O. het Veld, "Quantized Majorana conductance," *Nature*, vol. 556, pp. 1-26, 2018.

[117] R. Kubo, "Statistical-Mechanical Theory of Irreversible Processes. I. General Theory and Simple Applications to Magnetic and Conduction Problems," *J. Phys. Soc. Japan*, vol. 12, no. 6, pp. 570–586, 1957.

[118] D. A. Greenwood, "The Boltzmann Equation in the Theory of Electrical Conduction in Metals," *Proc. Phys. Soc.*, vol. 71, no. 4, pp. 585–596, 1958.

[119] R. Landauer, "Electrical resistance of disordered one-dimensional lattices," *Philos. Mag. A J. Theor. Exp. Appl. Phys.*, vol. 21, no. 172, pp. 863–867, 1970.

List of Publications

[1]   Tit, N., Ali, M., & Shaheen, A. (2019). Effect of Catalysis-clustering on Gas- sensing Performance. Bulletin of the American Physical Society.

[2]   Tit, N., Othman, W., Shaheen, A., & Ali, M. (2018). High selectivity of N-doped ZnO nano-ribbons in detecting H_2, O_2 and CO_2 molecules: Effect of negative-differential resistance on gas-sensing. Sensors and Actuators B: Chemical, 270, 167-178.

[3]   Tit, N., Shaheen, A., Othman, W., Aitladi, Y., Atatri, S., Abdelhadi, Y., & Berdiyorov, G. (2018). Selective Adsorption of H_2 Molecule on N-doped ZnO Nano- ribbons: Ab-initio Investigation. Bulletin of the American Physical Society.

[4]   Othman, W., Shaheen, A., Aitladi, Y., Atatri, S., Abdelhadi, Y., Berdiyorov, G. and Tit, N. (2018, February). Selective adsorption of H_2 on N-doped ZnO nano-ribbons: First-principle analysis. In 2018 5th International Conference on Renewable Energy: Generation and Applications (ICREGA) (pp. 227-231). IEEE.

[5]   Shaheen, A., Ali, M., Othman, W., & Tit, N. (2019). "Origins of Negative Differential Resistance in N-doped ZnO Nanoribbons: Ab-initio Investigation", *Scientific. Reports*. Accepted.

Appendix A

Reliability and Accuracy of NEGF-DFT in Calculating IV curves

A critical review about the topic was recently reported by Zhu and Liu [101]. Within the framework of bottom-top approach [101, 102], the properties are predicted based on fundamental atomic-orbitals basis set (first-principles). In this perspective, unlike the macroscopic world, quantum transport in nano-electronic devices is controlled by quantum coherence and non-equilibrium statistics. The addition of one dopant or removal of an atom might cause unpredictable trends. In the present investigation, a combination of non-equilibrium Green's function (NEGF) formalism and DFT in the version of SIESTA is used in the evaluation of transport properties (i.e., namely IV curves). While DFT method is a reliable method in predicting the ground-state properties, it has shortcomings in estimating the excited states such as estimating the bandgap energy. Consequently, possible sources of error in the IV-curve calculations should be: (1) Exchange-correlation functional: LDA and GGA are not always satisfactory for the purpose of transport properties. It is a compromised trade to reduce the error, for instance, one can adjust the hybrid functional to improve the estimation of bandgap energy but on the expense of other properties; (2) Incomplete basis set is a common challenge to all atomic orbital methods. For instance, in the plane-wave method, one can reduce the error by increasing the grid density in the k-space. As a matter of fact, in real space, the inclusion of more LCAO basis has been demonstrated to improve the quantum transport simulation [102]; (3) The error due to the discretization is common to all numerical simulations. Increasing the energy cut-off and the k-space grid always improve the results. Tests has to be carried out to ensure convergence of results such as atomic structures and DOS; (4) The error due to

the non-equilibrium coherent potential approximation (CPA) is specific to disordered systems. This did not alter our calculations of the present investigation; (5) Scattering mechanisms, such as electron-phonon scattering and impurity scattering, are either neglected or crudely approximated in NEGF in purpose to reduce the computational cost.

Last but not the least, one should pay attention that the errors are not independent or accumulative but may cancel with each other. One should not examine the errors one by one, but instead one can "calibrate" the electronic structure by comparing to the results of other methods or experimental data in bulk systems. It is reasonable to expect that the results of a quantum transport simulation are reliable as long as the electronic structures have been "calibrated" properly.

Appendix B

Quantum transport tips in mesoscopic systems

B.1 Universal conductance fluctuations

The measured electrical conductance in mesoscopic systems usually varies from sample to sample as being controlled by scattering events [103-105]. Within the scheme of the localization theory, the one-parameter scaling theory of Abrahams et al. [106] predicts the absence of quantum diffusion in disordered 1D and 2D systems and that all eigen-states to be exponentially localized. In this 1-parameter scaling theory, the mobility edge exists only in 3D disordered systems to separate between extended and exponentially localized electronic states. Further progress was done due to the two-parameter scaling theory by Kaveh [107] on 2D finite-size disordered systems. Using the Anderson model, Kaveh predicted the existence of a pseudo-mobility edge in 2D to separate two types of localized states; the power-law localized states towards the center of the band and the exponentially localized states towards the tails of the band. Yet, concerning the origins of the universal conductance fluctuations (UCF), the claims attributed them to both disorder (potential ensemble) and coherence effects of electronic wavefunctions (phase ensemble) [108]. These two effects can appear simultaneously in the dc-conductivity when the system size is smaller than both coherence length (L_Φ) and localization length (ξ), as Fermi level lies on defect states. Furthermore, the conductance fluctuations are even more pronounced when electrical transport is taking place in the weak localization regime (such as our devices). In weakly-localized systems, the fluctuation in conductance could reach the fundamental conductance "quanta", $G_o = \frac{2e^2}{h} = 7.75 \times 10^{-5} \Omega^{-1}$ where e is the electron charge and h is Planck constant, regardless of the number of conducting channels.

In disordered systems, where scattering events are predominant, a self-averaging quantity, like DOS, obeys the central-limit theorem and thus the iterations over the realization-random sets converge fast. Unlike this, the dc-conductivity is non-self-converging quantity and requires many iterations over random sets of phases. In brief, in nano-devices such as our present case, the magnitude of the universal conductance fluctuation is mainly influenced by two factors, the symmetry and the size of the sample. A third factor been recently added is due to the anisotropy of Fermi surface [109].

B.2 Minimum Metallic Conductivity:

In dirty (disordered) metals, it has been noticed that the dc-conductivity vanishes as temperature goes to 0 K in continuous way within a minimum value of $\sigma_{min} \cong 0.025 e^2/\hbar a$ (i.e., $G_{min} \cong 6.08 \times 10^{-6} \Omega^{-1}$, which corresponds to a maximum resistance $R_{max} \cong 0.2\ M\Omega$), where a is the average distance between impurities. This was reported by Mott [110] and experimentally observed by Davis and Compton [111]. From Drude model of conductivity, minimum metallic conductivity can easily be understood as the mean free-path cannot be smaller than the lattice spacing [112]. Until present, experimental evidence continues to appear and corroborate the existence of minimum metallic conductivity in various systems. For instance, recently, Farka and coworkers reported that conduction in the elastic scattering regime in conductive polymers of PEDOT: Sulphate to display a minimum metallic conductivity at low temperature of 4 K [113].

B.3 Conductance quantization

The conductance quantum, denoted as $G_o = \frac{2e^2}{h}$, can be achieved in clean quantum point-contact system limit [114]. The fabrication of quantized-conductance atomic switch (QCAS) was achieved, by Terabe group [115], in which the current exhibited stair-way behavior with conductance quantized into multiples of G_o. Such characteristics being achieved at room temperature and under ambient conditions would pave the way for these switches to be used in logical switches in future computers. Furthermore, quantized-conductance majorana of zero-mode – a type of localized quasiparticle – was recently fabricated for the same purpose of applications in quantum computing [116]. Nonetheless, one should make it clear that the phenomenon of quantization of conductance should not mean that the conductance of any system must be an integer multiple of G_o, as that can be reached only in case of realization of conductive channel(s) operating within the ballistic regime (i.e., with a transmission probability of unity). In case of disorder, it is usual that the transmission probability to be less than one, then the conductance would be even less than G_o (i.e., $G < G_o$). The total conductance of any system is, of course, the superposition of those due to its percolating channels.

B.4 Landauer conductance

The problem of electronic transport is a non-equilibrium one. The traditional method, known as linear response theory (LRT), considers the system at equilibrium and treats the driving electric force using a first-order perturbation approximation (i.e., the scheme of Kubo-Greenwood formalism of conductivity (117-118]). In 1970, Landauer [119] proposed a new formalism of conductance, which is probe-dependent and in which the system is composed of a sample as interacting with the two probes.

The transport through the scattering zone of sample is treated by a transmission coefficient T(E). The conductance (G) of the system in assumption of having one channel under a small applied bias (V) is given by:

$$G = \frac{I}{V} = \frac{2e^2}{h} T(E_F) \tag{B.1}$$

where e is the electron charge, E_F is Fermi energy, and h is the Planck constant. In case of existence of multi-channels within a cross-sectional area of a quasi-1D sample, then the Landauer formula can be generalized to the form:

$$G = \frac{2e^2}{h} \sum_{i,j} T_{ij} (E_F) \tag{B.2}$$

where T_{ij} is the probability that a carried (say electron) transmits from the i-th mode at the left to j-th mode at the right side of the sample; and E_F is the Fermi energy. In case of small bias, the general expression of electric current would be:

$$I = \int_0^\infty \frac{dE}{e} [f(E + eV) - f(E)] G(E) \tag{B.3}$$

The Hamiltonian of the system is written as $H = H_0 + U$, where H_0 is the Hamiltonian of the sample as uncoupled to the electrodes, and U represents the coupling between the sample and the electrodes. The transmission operator becomes:

$$T(E) = U + UG(E)U \tag{B.4}$$

where $G(E) = \frac{1}{E-H+i\eta}$ is the Green's function. The transmission probability in equation (B.2) is related to the matrix elements of T(E) operator in equation (B.4) by the following relation:

$$\sum_{i,j} T_{ij} (E) = 4\pi^2 \sum_{l,r} |T_{lr}|^2 \delta(E - E_l)\delta(E - E_r) \tag{B.5}$$

where δ is the Dirac delta function, E_l and E_r are the energy modes at left and right electrodes, respectively. Under bias V_b, they are related as: $E_l = E_r - eV_b$, so the current flows from left to right electrodes.